Development of Liquid Argon Detector for Dark Matter Search

暗黒物質探索のための液体アルゴン検出器の開発

March, 2024

Kazutaka AOYAMA
青山　一天

Development of Liquid Argon Detector for Dark Matter Search

暗黒物質探索のための液体アルゴン検出器の開発

March, 2024

Waseda University Graduate School of Advanced Science and Engineering

Department of Pure and Applied Physics, Research on Experimental Particle Physics

Kazutaka AOYAMA
青山　一天

Abstract

Despite numerous cosmological observations strongly suggesting the presence of dark matter, its nature remains unknown. The current dark matter search can be broadly categorized into three types: direct detection, indirect detection, and accelerator experiments. In direct searches, various signals such as light, ionized electrons, and heat produced by the interaction of dark matter with matter in the Standard Model are detected. To effectively search for dark matter, it is essential to construct detectors utilizing a large target medium, enabling the detection of events with smaller recoil energy, while minimizing the occurrence of background events that mimic the signals. In the indirect search, dark matter is searched through the observation of particles in the Standard Model that result from the decay or annihilation of dark matter. Detectors can be mounted on balloons or satellites, or positioned on the ground, all of which enhance sensitivity by increasing the solid angle and effective area. When detecting particles that do not lose information on the direction of origin, such as gamma rays, the detector must be capable of reconstructing the flight direction. Additionally, when detecting targets with low fluxes (such as cosmic ray antiparticles), the detector must have the capability to identify particles.

Among many detectors, those utilizing liquefied noble gases are leading the search because of their excellent performance. In direct searches, experiments such as LUX and XENONnT, using xenon as a target, and DEAP and DarkSide, using argon as a target, have provided the most stringent limitations over a wide range of dark matter masses from 1 GeV to 1 TeV. In addition, the excellent energy/position reconstruction capability, strong particle identification capability, and ease of scaling up make them potential candidates for applications in indirect searches where argon has not been used as a detector.

Liquid argon functions as a calorimeter. When a particle passing through liquid argon drops energy into liquid argon, the energy is converted into scintillation photons or ionizing electrons through excitation, ionization, and recombination processes. The operation of liquid argon detectors involves a number of technical challenges, such as the high purity of liquid argon, the cryogenic temperature of liquid argon, and the detection of vacuum ultraviolet photons. On the other hand, the scintillation waveform, ionization/scintillation ratio, and dE/dX are different for each incident particle, making strong particle identification possible. This particle identification capability can be enhanced by improving light collection efficiency and spacial resolution, and by reducing noise in the readout electronics. There are many technical issues to be solved for the operation of liquid argon and development challenges to improve the detector performance, and the focus should vary depending on the target to be detected. In this study, we first addressed the following two points that lead to improvement of direct search sensitivity. The first is to improve the light collection efficiency of vacuum ultraviolet light. To collect and detect vacuum ultraviolet light more efficiently, wavelength is converted to visible light. We built vacuum evaporation system for the conversion material TPB and optimized the amount of the coating. Then, a compact liquid argon detector was constructed and the light collection efficiency was measured. As a result, the

world's largest light collection efficiency was confirmed. In order to further improve the light collection efficiency, PMT with a quantum efficiency of 30% has been replaced by MPPC with a quantum efficiency of 50-60%. The second is a spectrum measurement of continuous wavelength emission in the visible region in the gas phase, which is still not fully understood. We constructed a gas argon TPC setup that is simpler to use than liquid argon, and performed the measurements. The electric field dependence and wavelength spectrum were consistent with Neutral bremsstrahlung, which can explain visible light emission. In addition to the above, a balloon-borne test of the liquid argon detector was performed for the application to the indirect search experiment with a flying objects, where liquid argon detectors have not been used so far. The balloon-borne liquid argon TPC was launched on July 27th, 2023, and both environment data and TPC data were obtained. The experiment successfully maintained high-purity liquid argon in the stratosphere, and cosmic charged particles were successfully observed.

Acknowledgments

This work was made possible by the support of many people. As I finish writing my dissertation, I would like to express my gratitude.

First, I am grateful to Prof. Kohei Yorita, who has continued to provide me with unvaluable advice over the past seven years since I joined to his graduation research in my fourth year of undergraduate school. His passion for physics was one of the guidelines for my research and strongly encouraged me. I have learned not only about research but also about how to live as a physicist and how to be truly independent as a person. I am grateful to Masashi Tanaka leading the liquid argon experiment at Waseda university. He showed me how to create an experimental site and how to proceed with the experiment. I was in awe of his deep thinking and learned many essentials. Since joining this lab, both Prof. Kohei and Masashi have consistently encouraged me to take on all challenges without limiting me. Those experiences made me who I am today.

I would like to thank Prof. Hirokazu Odaka. His comments, based on the many experiences he gained from his satellite missions, were especially valuable during the balloon engineering flight.

I would like to thank Prof. Jun Kataoka. His extensive knowledge from radiation science has enhanced my research.

I am grateful to my colleagues who worked with me on the liquid argon experiment. To Dr. Tatsuki Washimi, we worked together to prepare for the experiment and he showed me various hardware techniques. I especially respect Dr. Masato Kimura's analytical skills, which come from his continued careful observation of data. I also enjoyed talking with Masato-san about the experiments. I also thank Kodai Iwasawa, Taichi Nakasone, Mayu Sakurai, Tiga Shimizu, Hinako Taniguchi, Riki Nakajima, Yorinobu Utsumi, Koki Ishikawa, Utano Hijikata, Yutaro Yano, and Shintaro Arai. Without them, the balloon experiments, beam tests, and deveropment of charge readout of the past few years would not have been possible. I would also thank Tetsuma Yaguchi, Takanori Kikuchi, Yuki Takemura, Kotaro Iijima, Tomomasa Takeda, Hiroyuki Morohoshi, Ryukichi Ozu. In Dr. Masato's words, "we all were power-type men." I think so too.

I wish also express my gratitude to the GRAMS collaborators, especially Ryota arai, Tsubasa Tamba, Satoshi Takashima, Marina Yoshimoto, Naomi Tuji, and Tsuguo Aramaki, who made the balloon experiment successful together. I was encouraged from discussion with them.

Lastly, I am grateful to my parents, Shinji and Shizue, and my brothers, Soshiro and Kenta. They give me a lot of support for long time.

Contents

List of figures

List of tables

Chapter 1

Introduction

Dark matter, a mysterious matter that does not emit, absorb, or reflect photons, was first proposed by F. Zwicky et al. in 1933 to account for unexplained gravitational effects within coma galaxy clusters [1]. Subsequent cosmological observations, including galaxy rotation curves [2] and gravitational lensing effects [3], have provided convincing evidence supporting its presence. Furthermore, predictions from Cosmic Microwave Background (CMB) observations, such as those from the Planck satellite in 2018, suggest that dark matter constitutes approximately 23% of the universe's total energy density $\Omega_c h^2 \sim 0.12$ (~23%) [4].

Dark matter is postulated to possess specific properties, including (i) a lifetime significantly longer than the age of the universe, (ii) a suitably low kinetic velocity during the formation of cosmic large-scale structures, and (iii) minimal to no electromagnetic interaction. Neutrinos, within the framework of the Standard Model, satisfy conditions (i) and (iii). However, due to their lightweight nature, they move at speeds approaching the speed of light, preventing them from contributing significantly to the formation of cosmic large-scale structures.

While these observations provide strong evidence for the existence of dark matter, its precise nature remains entirely elusive. It is believed to be a new particles that eludes explanation within the confines of the Standard Model. Understanding its nature stands as one of the most important issues in modern physics, driving numerous research groups worldwide to actively conduct experiments aimed at detecting and revealing the mysteries of dark matter.

This chapter provides an overview of the search for dark matter and the detectors utilized in dark matter detection. Additionally, we summarize the structure of this dissertation at the end of the chapter.

1.1 Review of dark matter search

The candidates for dark matter are considered to be of multiple types, and many groups are conducting experiments using detectors specifically designed to be sensitive to the targeted dark matter. The current approaches can be broadly categorized into three types: direct detection, indirect detection, and accelerator experiments.

Accelerator experiments, exemplified by the Large Hadron Collider [5], focus on detecting dark matter within the particles generated by colliding Standard Model particles in high-energy accelerators. In this approach, the exploration range for mass is constrained by the accelerator's energy, posing a challenge

in extending the search to a higher mass range. Nevertheless, upon discovery, precise measurements of properties such as mass, cross-section, and spin become feasible.

Direct searches involve the detection of light, ionized electrons, heat, and other signals produced by the interaction (scattering) of dark matter with matter in the Standard Model. Detectors, including liquid noble gas detectors and cryogenic detectors, are strategically placed on the Earth's surface or underground to detect dark matter in the vicinity of the Earth. Detection becomes challenging when the mass of dark matter is small due to the low scattering energy. Accelerator experiments and direct searches complement each other in exploring the mass range.

Indirect searches focus on observing cosmic rays in the Standard Model (γ, e^+, $\bar{p}$, $\bar{D}$, etc.) resulting from the decay or annihilation of dark matter. This search method includes experiments conducted with balloons and satellites.

These three search methods can be represented by an equivalent Feynman diagram, as shown in Fig. 1.1. Currently, various experimental groups are in competition to be the first to discover dark matter. Upon discovery, these three methods are anticipated to provide mutually reinforcing evidence, contributing to a clearer understanding of the nature of dark matter. In this section, we outline the current status of dark matter search experiments.

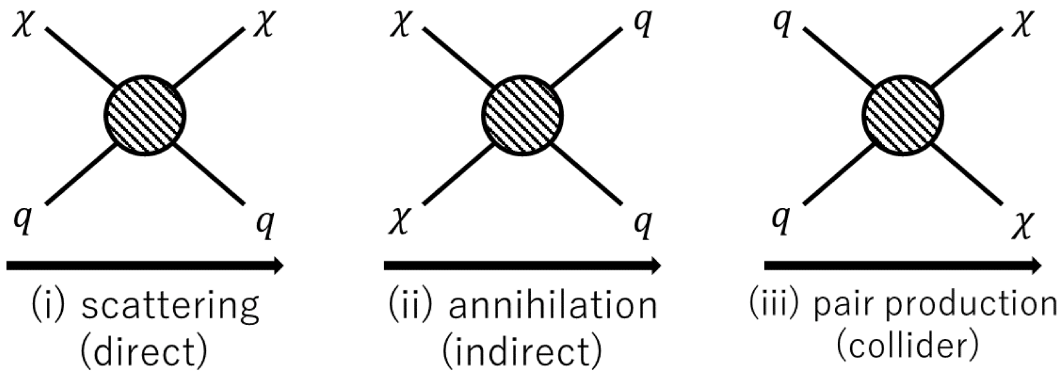

Fig. 1.1. Feynman diagrams representing interaction for (i)direct, (ii)indirect, and (iii)collider dark matter searches.

1.1.1 Direct dark matter detection experiment

Dark matter is assumed to surround galaxies and follows a velocity distribution modeled by a Boltzmann distribution, characterized by a most probable speed v_0. This distribution describes the statistical behavior of dark matter particles. Additionally, the average velocity is assumed to be zero relative to the galaxy. As the Earth orbits within the galaxy as part of the solar system, a detector placed on Earth continually traverses the region where dark matter is present, introducing a relative velocity between the Earth and the dark matter. Under this hypothesis, the search is conducted with the premise that dark matter recoils

with the target material at a velocity equal to the sum of the Earth's motion relative to the galaxy and the velocity derived from the Boltzmann distribution.

In a direct search, nuclei or electrons within the target materials undergo scattering. When dark matter deposits energy into the target material, it triggers a reaction with the moving charged particle–either a recoiled target nucleus or electrons–resulting in the production of light, charge, heat, and other signals within the detector. These signals are then detected to reconstruct the recoil energy or distinguish the particle. Recoil events involving dark matter and target materials are rare due to the low dark matter-nucleon scattering cross-section. Therefore, conducting experiments in an extremely low-background environment, achieved through the removal of background events, is crucial.

Event rate of dark matter-nucleus elastic scattering

The description in this section is informed by Ref.[6]. In experiments searching for the elastic scattering of dark matter and target nuclei, the detection rate of dark matter-nucleus elastic scattering events in the detector is calculated as follows. However, in the subsequent calculations, we proceed under the assumption that there is only one type of dark matter which has a mass m_χ and a number density n_χ in the vicinity of Earth.

The velocity of dark matter is assumed as follows:

$$f(\boldsymbol{v}) = \frac{1}{(\pi v_0^2)^{3/2}} exp\Big(- \frac{|\boldsymbol{v} - \boldsymbol{v_E}|^2}{v_0^2}\Big), \tag{1.1}$$

where $\boldsymbol{v_E} \sim 230$ km/s is the velocity of Earth relative to the Milky way and v_0 is ~ 220 km/s.

The event rate R can be expressed as in Eq. 1.2 in unit of events/day/kg when selecting a nucleus $N(Z, A)$ as the target material with atomic number Z and mass number A.

$$R = \frac{N_A}{A} n_\chi \int_{E_R^{min}}^{E_R^{max}} dE_R \int_{v_{min}}^{v_{max}} dv f(\boldsymbol{v}) \frac{d\sigma_N}{dE_R}. \tag{1.2}$$

The parameter E_R is the recoil energy of dark matter and target nuclei. E_R^{max} is the maximum recoil energy and E_R^{min} is the minimum detectable recoil energy. v_{max} is the maximum velocity of dark matter constrained by escape velocity of Standard Halo Model, and v_{min} is the minimum velocity at which the recoil energy becomes E_R, and N_A is the Avogadro's number. v_{min} is given by

$$\begin{aligned} v_{min} &= \sqrt{\frac{m_N E_R}{2\mu^2}}, \\ \mu &= \frac{m_N m_\chi}{m_N + m_\chi}, \end{aligned} \tag{1.3}$$

where m_N is target nuclei mass. The differential scattering cross section of dark matter and target nuclei

is written as

$$\begin{aligned} \frac{d\sigma_N(q)}{dq^2} &= \hat{\sigma_N}\frac{F(q)^2}{4\mu^2 v^2}, \\ q &= \sqrt{2m_N E_R}, \\ \hat{\sigma_N} &= \frac{4\mu^2}{\pi}[Zf_p + (A-Z)f_n]^2 + \sigma_N^{SD}, \end{aligned} \tag{1.4}$$

where q is a momentum transfer, $\hat{\sigma_N}$ is a cross section at zero momentum transfer, and $F(q)$ is a nuclear form factor. The first term of $\hat{\sigma_N}$ is the spin-independent cross section, while the second term is the spin-dependent cross section. We only consider the spin-independent cross section since the target material in this study, ^{40}Ar, has zero total nuclear spin. f_p and f_n represent the effective coupling constants of protons and neutrons with dark matter, respectively. In direct dark matter search experiments, the Helm Form Factor written in Eqn. 1.5 is commonly used as a correction factor $F(q)$ [7]. In cases where the momentum transfer q is not negligible compared to the de Broglie wavelength of dark matter, the reaction cross-section is reduced due to the visibility of the internal structure of the nucleus.

$$\begin{aligned} F(q) &= 3\frac{\sin(qr_N) - qr_N\cos(qr_N)}{qr_N}e^{-(qs)^2} \\ r_N^2 &= c^2 + \frac{7}{3}\pi^2 a^2 - 5s^2 \\ c &: 1.23A^{1/3} - 0.60\,\mathrm{fm} \\ a &: 0.52\,\mathrm{fm} \\ s &: 0.90\,\mathrm{fm} \end{aligned} \tag{1.5}$$

Here, when effective coupling constant f_p and f_n are equal, and the scattering cross-section for protons is denoted as $\hat{\sigma_p}$, $\hat{\sigma_N}$ is given as follows:

$$\hat{\sigma_N} = (\frac{m_p + m_\chi}{m_N + m_\chi})^2 A^4 \hat{\sigma_p}. \tag{1.6}$$

When using different atomic nuclei as the target, a comparison is made with the nucleon scattering cross-section $\hat{\sigma_p}$. The recoil energy E_R of the elastic scattering is calculated from momentum conservation as follows:

$$\begin{aligned} E_R &= E_i r\frac{1-\cos(\theta)}{2}, \\ r &\equiv \frac{4m_\chi m_N}{(m_\chi + m_N)^2}, \end{aligned} \tag{1.7}$$

where E_i is the kinetic energy of incident dark matter, and θ is the scattering angle. If we assume isotropic scattering in the center-of-mass frame, the event count becomes uniform for recoil energy in the range of

$0 \leq E_R \leq E_i r$. Then differential event rate is given as follows:

$$\frac{dR}{dE_R} = \int_{E_i^{min}}^{E_i^{max}} \frac{1}{E_i r} dR(E_i) = \int_{\boldsymbol{v}} \frac{1}{E_i r} dR(\boldsymbol{v} - \boldsymbol{v_E}). \tag{1.8}$$

E_i^{max} and E_i^{min} represent the maximum and minimum kinetic energies of the incident dark matter, respectively. Substitute Eq.1.2 into Eq.1.8 yields

$$\frac{dR}{dE_R} = \frac{N_0}{A} n_\chi F(q)^2 \hat{\sigma_N} \int d^3\boldsymbol{v} f(\boldsymbol{v} - \boldsymbol{v_E}) v. \tag{1.9}$$

Figure 1.2 illustrates the energy spectrum resulting from dark matter-nucleus scattering with argon as the target material. The assumed dark matter-nucleus scattering cross-section is 10^{-40} cm^2, and calculations span dark matter masses ranging from 10 to 100 GeV/c^2. The recoil energy is on the order of several tens of keV, with a higher event rate at lower energies. Particularly for low-mass dark matter with a mass of 10 GeV/c^2, the event count sharply decreases for recoil energies above 10 keV, thus it is advantageous to lower the energy threshold of the detector. Additionally, the greater the mass of the target material and the observation time, the larger the number of detectable events. Therefore, the enlargement of detectors and their long-term operation is crucial.

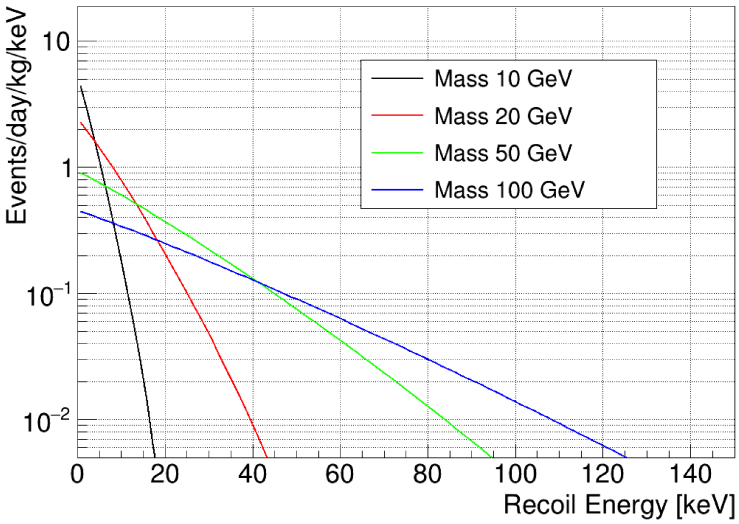

Fig. 1.2. Expected recoil energy spectra for argon target for dark matter masses of 10, 20, 50, 100 GeV/c^2 with dark matter-nucleus scattering cross-section of 10^{-40} cm^2, respectively.

Detectors in direct dark matter search experiments

Direct search experiments are designed to detect signals resulting from the recoil of particles and target material. Various signals, such as light, ionization electrons, and heat, can be generated during these interactions. The choice of the signal to be measured depends on the type of detector utilized, each

with its own advantages and disadvantages. The following provides an overview of detectors commonly utilized in direct searches for dark matter.

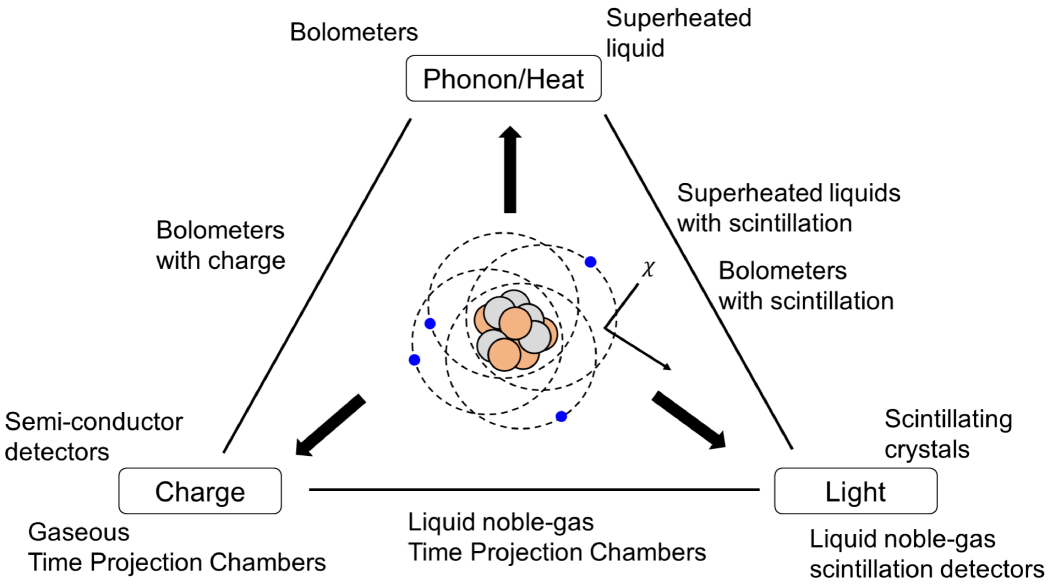

Fig. 1.3. Schematic diagram of signal types utilized in the direct dark matter search.

Scintillating Crystals: Solid scintillators are highly robust and operate at room temperature, making them relatively easy to handle. However, one notable challenge is the presence of radiation impurities, which contribute to background events in dark matter searches. Unfortunately, these impurities cannot be removed after crystallization. Consequently, there is active development focused on crystallization techniques aimed at achieving extremely low background events [8]. The energy threshold for detection typically lies around several keV.

Liquid Noble-gas detectors: Liquid noble gases, such as xenon and argon, emit ionized electrons and scintillation light upon energy deposition. Operating liquefied noble-gas detectors is challenging due to their cryogenic temperatures and the signal attenuation caused by impurities. However, the advantage lies in obtaining a large target mass, facilitated by the higher density compared to gases. Furthermore, scalability is achievable, with ton-scale detectors already in operation. Additionally, the scintillation waveform and the scintillation/ionized electron ratio depend on particle types, contributing to the reduction of background events. Typically, the energy threshold for these detectors is in the range of several 100 eV to several 10 keV.

Semi-conductor detectors: Electron-hole pairs produced by energy deposition are detected as signal in semi-conductor detectors, such as silicon and germanium. The high cost per unit mass of semi-conductor detectors makes larger detector sizes difficult. On a positive note, semiconductor detectors offer excellent energy resolution and energy threshold due to their very small band gap.

Bolometers: The bolometer is designed with extremely low heat capacity, and it registers a temperature increase in the target material caused by energy deposition from incident particles. Target materials, such as semiconductors (e.g., silicon and germanium) and scintillators like $CaWO_4$, are employed. Although the target material must be cooled to about 10 mK, the energy threshold is exceptionally low, typically on the order of a few 10 eV. However, increasing the mass of the target causes an elevated energy threshold, making it difficult to enlarge the detector. In addition to the heat channel, combining ionized electron and optical signals allows for the separation of electron and nuclear recoils, contributing to the reduction of background events.

Recent results of Dark Matter Direct Detection

In a direct dark matter search experiment, sensitivity relies on the expected number of signal events and background events. A discovery is claimed if the number of detected events significantly exceeds what can be explained by background events. Conversely, if the observed events can be reasonably explained to background events, the existence of dark matter is rejected. For instance, in a scenario where a dark matter like event is detected in an environment with zero background, a dark matter is claimed. In cases where a dark matter-like event is observed, its consistency with dark matter is validated through various means, such as utilizing a different target detector or conducting experiments by different research groups, as well as examining time and directional dependence.

Many experiments are currently conducting direct searches for dark matter, utilizing a wide variety of target materials and techniques. The global status of these direct dark matter searches is illustrated in Fig. 1.4 with the dark matter mass on the horizontal axis and spin-independent dark matter-nucleon scattering cross section on the vertical axis. Fig. 1.4 is generated using 'Dark Matter Limit Plotter v5.18' [9]. The solid curve in Fig. 1.4 represents the experimental results that reject the existence of dark matter above that line. The assumed dark matter density near Earth is 0.3 $\mathrm{GeV/cm^3}$. The yellow area in the lower part of the figure is expected to be affected by background events from coherent scattering; solar neutrinos dominate below 10 $\mathrm{GeV/c^2}$, while atmospheric neutrinos dominate above 10 $\mathrm{GeV/c^2}$ [10].

The experiments utilizing liquefied noble gas detectors, such as the DarkSide [11] and DEAP [12] experiment with liquid argon, and the XENON [13, 14] and LZ [15] experiments with liquid xenon, have set the most stringent limit in the mass region above $\sim$ 1 $\mathrm{GeV/c^2}$. These experiments exhibit high sensitivity in the region of relatively heavy mass and low scattering cross-section because of the ease of scaling up the detector. The results obtained by DarkSide-50 in the several $\mathrm{GeV/c^2}$ region were not derived from an experiment conducted in a zero-background event environment. Instead, they are based on data acquired by triggering the ionized electron signal; however, the energy threshold for this signal is 0.6 keVnr, where keVnr represents the energy scale for nuclear recoils. For sub-GeV dark matter, CRESST experiment provides the most stringent limits by utilizing a bolometer with $CaWO_4$ as a target [16]. The bolometer's small energy threshold is advantageous for detecting dark matter with relatively lower masses. In addition to these most stringent limits, experiments employing various targets and techniques have provided constraints. Examples include CDMSlite experiment with a semi-conductor bolometer [17], NEWS-G experiment with a Ne + CH_4 mixture gas [18], COSINE experiment with a

NaI(Ti) scintillator [19], PICO experiments with a bubble chamber [20], and DAMIC experiment with a silicon of charge coupled device [21]. The dashed lines in the figure represent the expected sensitivity of future experiments. The superCDMS experiment (gray dashed line) utilizes a semiconductor bolometer with silicon and germanium [22], while the GADMC 300 ton-year [23] (purple dashed line) and DARWIN 200 ton-year [24] (green dashed line) experiment employ liquid argon and liquid xenon as target nuclei, respectively.

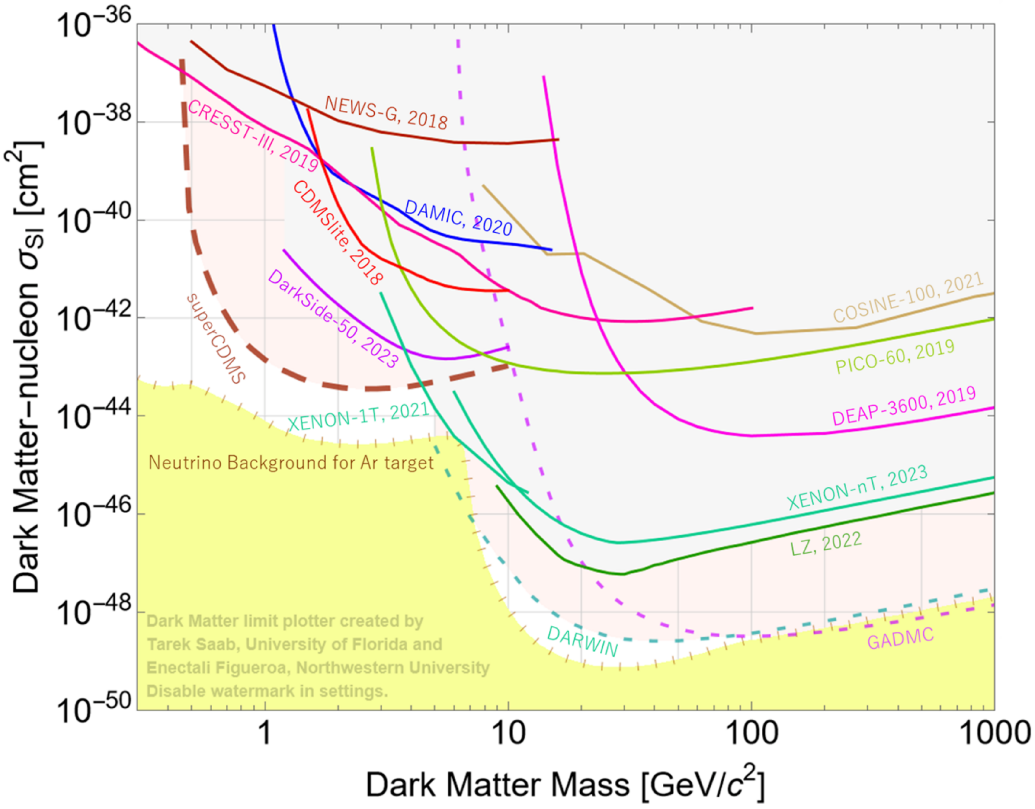

Fig. 1.4. Overview of results from direct dark matter detection experiments in mass and cross section parameter space. The solid line represents the 90%C.L. upper limits, while the dashed line indicates the predicted sensitivity. The colored area at the bottom of the figure represents the region where solar or atmospheric neutrinos are expected to contribute as background events. The figure is generated using 'Dark Matter Limit Plotter v5.18' [9].

1.1.2 Indirect dark matter detection experiment

The indirect search for dark matter involves detecting signals, such as gamma rays, neutrinos, antiparticles, and other Standard Model particles, that reach around Earth as cosmic rays. If a component is detected, which cannot be attributed to known cosmic ray sources but can be explained by the annihilation or decay of dark matter, a discovery is either claimed or suggested. However, it is crucial to consider unknown cosmic ray sources and uncertainties in cosmic ray propagation. Observations are conducted

using detectors on satellites, atmospheric balloons, and ground-based telescopes.

The production rate of Standard Model particles from dark matter depends on (i) the annihilation cross-section $\langle\sigma v\rangle$ or lifetime τ_{DM}, (ii) the number density of dark matter $\rho_{DM}(\vec{r})/m_{DM}$, and (iii) the types of final states f possible through annihilation or decay. The production rates from annihilation $q_f^{Ann}(\vec{r}, E)$ and decay $q_f^{Dec}(\vec{r}, E)$ can be expressed as follows, respectively:

$$q_f^{Ann}(\vec{r}, E) = \alpha\langle\sigma v\rangle \frac{dN_f^{Ann}}{dE_f}(\frac{\rho_{DM}(\vec{r})}{m_{DM}})^2, \tag{1.10}$$

$$q_f^{Dec}(\vec{r}, E) = \frac{1}{\tau_{DM}} \frac{dN_f^{Dec}}{dE_f}(\frac{\rho_{DM}(\vec{r})}{m_{DM}}), \tag{1.11}$$

where $\frac{dN_f^{Ann}}{dE_f}$ and $\frac{dN_f^{Dec}}{dE_f}$ represent the number of particles produced per annihilation and decay, $\rho_{DM}(\vec{r})$ is the energy density of dark matter at position $(\vec{r})$, and m_{DM} is the dark matter mass. The constant α is 1/2 if the dark matter is Majorana particle, and 1/4 if not. In decay, the number density term appears to the first power, while in annihilation, it appears to the second power.

The distribution of dark matter, particularly in the galactic center, is not well-understood. Furthermore, the event rate depends on the extent to which particles created by annihilation and decay can reach the Earth within the halo. Particles produced by annihilation or decay propagate through space to the earth via processes such as diffusion, convection, and re-acceleration. Reducing the uncertainty in the generation and propagation processes is essential for predicting event rates and conducting indirect dark matter searches.

Recent results of Dark Matter Indirect Detection

Several observations suggestive of dark matter have been reported in γ-ray and antiparticle observations. These include AMS-02, Fermi-LAT, BESS experiments, which will be reviewed below.

anti-particles: Charged particles resulting from the annihilation or decay of dark matter can reach the Earth as cosmic rays. To maximize the signal-to-background ratio, searches focus on antimatter, such as positrons, antiprotons, and anti-nuclei. This is because antimatter is less frequently produced through primary and secondary known processes compared to ordinary matter, resulting in fewer background events.

Alpha Magnetic Spectrometer-02 (AMS-02) [25], a detector installed on the International Space Station (ISS) designed to measure cosmic rays with high sensitivity, comprises a silicon tracker, permanent magnet, Time of Flight scintillator, transition radiation detector, Cherenkov counter, and calorimeter. The detector can identify the mass and charge of an incident particle by combining each of these detectors. Figure 1.5 displays AMS-02's observations of antiprotons in the left panel [26] and positrons in the right panel [27]. The red plots in the left panel represent the flux obtained from AMS-02, while the solid lines depict the fitted results. The fitting process takes into account the contribution from the secondary production (in the blue line) and dark matter annihilation (in the yellow band), along with the propagation

process. To determine the background event for antiprotons, the fitting process considers the observation of B/C ratio, the ^{10}Be/^{9}Be ratio, and the proton flux. The flux of dark matter-derived antiprotons is then calculated within 2σ of the fitted result for the background event. In Fig. 1.5, assumed dark matter mass is 47 GeV/c^2 and an annihilation cross-section $\langle\sigma v\rangle$ is 10^{-26} cm^3/s, indicating a component that cannot be explained by cosmic rays from secondary production alone. However, the flux from dark matter is approximately two orders of magnitude lower than that from secondary production, and the uncertainty of background events remains an issue.

For positrons in right panel of Fig. 1.5, components that cannot be explained by known sources have also been observed. Pulsars and dark matter are listed as potential source terms. However, if all components are attributed to dark matter, a dark matter mass above 1 TeV is required. Special modeling is necessary to constrain the particles produced by annihilation to avoid contradictions with other observations, such as antiprotons and gamma rays. High-sensitivity observations of cosmic-ray charged particles, including antiprotons, and modeling of their propagation processes and production origins are still in progress.

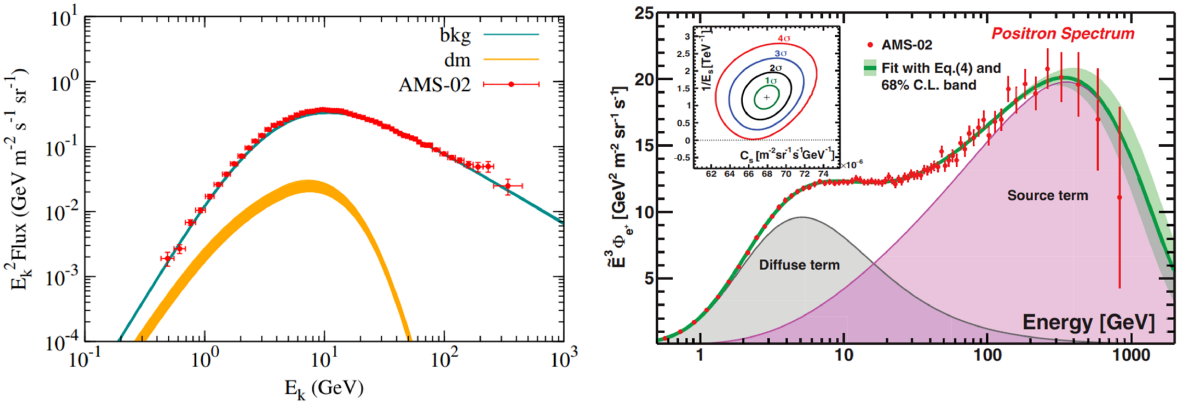

Fig. 1.5. Observation results of antiprotons (left) and positrons (right) by AMS-02 along with model fitting results. These figures are taken from Ref.[26] and Ref.[27].

On the contrary, there have been no observations of heavier anti-nucleus than proton in cosmic rays, despite they are anticipated to serve as effective probes in the search for dark matter. Figure 1.6 shows the expected anti-deuteron fluxes, taking into account the contribution from secondary production (depicted in the red line) and dark matter annihilation suggested from anti-proton observation (depicted in the green line), alongside the upper limit set by the BESS-Polar and the sensitivity of future experiments such as AMS-02, GAPS, and GRAMS. The secondary background flux peaks at the kinetic energy per nucleon (rigidity) of a few hundred MeV/n, given the kinematic suppression of secondary production at low momentum. In contrast, anti-deuterons originating from dark matter annihilation are not subject to such suppression at low momentum, resulting in a flux that is two orders of magnitude higher than the secondary background in the low-energy region. Among the various experiments, only BESS, a long-duration balloon-borne experiment, has provided an upper limit of 1.9×10^{-4} /m^2/s/sr/(GeV/n) within a rigidity range of 0.17–1.15 GeV [28]. BESS employs ToF scintillators and superconducting

magnets with a gas detector. Additionally, upcoming balloon-borne experiments such as GAPS, utilizing Si detectors and ToF [29], and GRAMS, utilizing a liquid argon detector and ToF [30], are in preparation for observations. The expected sensitivities of GAPS, GRAMS, and AMS-02 are shown in the Fig. 1.6, respectively.

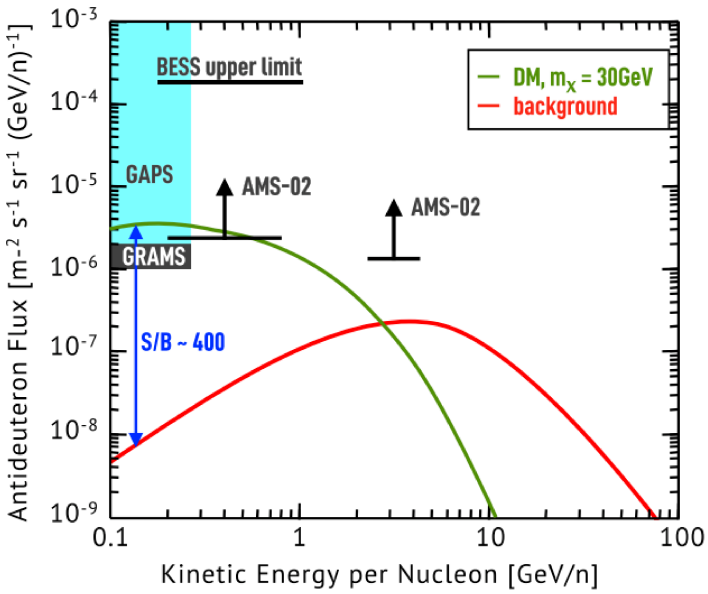

Fig. 1.6. Anti-deuteron sensitivity for GAPS, GRAMS, AMS-02 with expected fluxes from secondary sources (green line) and dark matter annihilation (red line). The balloon-borne experiment, BESS, provides an upper limit of 1.9×10^{-4} /m^2/s/sr/(GeV/n). Figure is taken from Ref.[30].

γ/X-ray: Gamma rays and X-rays are emitted from any final state through a variety of processes including 2γ decay of neutral pions, bremsstrahlung from charged particles, as well as 2-body decay of dark matter to γ rays, and decay to γZ. The 2-body decay from dark matter exhibits as energy peak at its mass, whereas other emission processes result in continuous spectrum. Gamma rays remain unaffected by magnetic fields during propagation, preserving their directional information. Therefore, it is essential to carefully select observation regions, considering both the density of dark matter and the background derived from known processes. Additionally, the direction reconstruction capability is a crucial requirement for the detector.

Figure 1.7 show the results of dark matter searches based on γ-ray observations from the galactic center and dwarf galaxies [31]. The solid black lines represent 11 years of Fermi-LAT observations on 27 dwarf galaxies, along with data on the galactic center excess and the thermal relic cross section.

1.2 Requirements for dark matter search detector

The following requirements are crucial for detectors used in dark matter searches:

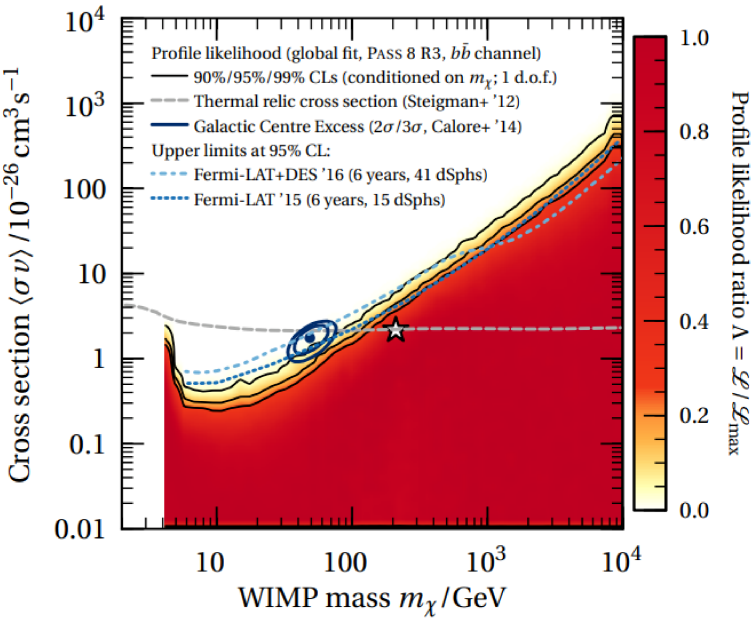

Fig. 1.7. Results of dark matter search utilizing Felmi-Lat data on dark matter mass and annihilation cross section parameter space. This analysis use 11 years of Pass 8 data for 27 dwarfs, and shows profile likelihood for the $b\bar{b}$. The figure is taken from Ref.[31].

1. Large target mass (for direct detection), or large sensitive area/solid angle (for indirect detection),
2. Low energy detection threshold (especially for direct detection),
3. Minimal external/internal background (for both direct and indirect detection),
4. Particle identification capability (for both direct and indirect detection).

The first requirement enhances the number of signal events, and the second is particularly effective in direct searches for low-mass dark matter, as shown in Fig. 1.2.

In rare event searches, the reduction of other radiation acting as background events is essential, i.e. requirement 3. In direct searches, background events consist of external background, which is incident from outside the detector, and internal background, originating from the materials of the detector. External background events comprises environmental neutrons, γ rays emitted from structures around the detector, as well as cosmic rays. A shield, consists of lead or water, around the detector reduces these background events. Addressing neutron background is crucial since neutrons cannot be analytically distinguished from nuclear recoil events caused by dark matter interactions. Shielding is an effective method to reduce neutron background, and an active veto detector also assesses the neutron background. Internal background events comprises γ rays, β rays, and α rays originating from radioisotopes present in the detector materials. Additionally, neutrons are produced from the α rays through the (α, n) reaction. Shielding is less effective against internal background events, making it crucial to use materials with low radiation sources through thorough material screening. Cosmic rays, particularly muons, not only penetrate the detector themselves but also interact with the detector components and the surrounding ground and buildings, leading to

the secondly generation of background events. Cosmic rays, particularly muons, not only penetrate the detector themselves but also interact with the detector components, the surrounding ground, and buildings, leading to the generation of secondary background events. Underground experimental facilities, such as the Gran Sasso and Kamioka mines, utilize the surrounding rock as a shield, resulting in fewer external background events caused by cosmic rays. Many research groups choose to conduct experiments in underground environments to minimize these external background events [32].

In addition, background events that cannot be mitigated through material screening, relocation to underground facilities, or shielding should be distinguished by employing distinct signal features depending on particle types, as specified in requirement 4. In indirect searches involving antiparticles, numerous ordinary particles, such as protons, traverse the detector with a higher flux compared to antiparticles. In gamma-ray observations, neutrons and other particles constitute background events. Hence, particle identification is crucial in indirect searches as well.

1.3 The flow of this dissertation

This chapter provides an overview of the current status of the dark matter search. Chapter 2 reviews the properties of argon as a target material, including its properties, and scintillation/ionization yield, etc. Chapter 3 summarizes the features and challenges of liquid argon detectors. Additionally, it presents a summary of the dissertation's subject.

In Chapters 4 and 5, we detail efforts to enhance the light collection efficiency of liquid argon detectors. In Chapter 4, we discuss the production of the wavelength shifter vacuum deposition system, optimization of vacuum deposition, and light collection efficiency measurements using a compact liquid argon detector with a photomultiplier tube (PMT). Chapter 5 describes the installation of TSV-MPPC, a device highly sensitive to visible light and advantageous for constructing large photodetection areas. We first summarize tests to confirm the TSV structure's operation in the cryogenic environment of liquid argon using a single-channel TSV-MPPC. Subsequently, we describe light collection efficiency measurements using the array type.

Chapter 6 describes a study of the continuous wavelength component in visible light in the gas phase, known as Neutral Bremsstrahlung (NBrS). This emission component has been theoretically studied, and experimental verification has been crucial in recent years. In this study, data were obtained at a gaseous argon TPC and compared with a theoretical model of NBrS.

Chapter 7 provides a description of the loading test of the liquid argon detector to a scientific balloon, conducted with the potential application in indirect search experiments.

Chapter 8 provides a conclusion of the results obtained in this study and discussion for application of liquid argon detector to dark matter search.

CHAPTER 2

Argon as a detector medium

Liquid argon is a highly promising radiation detector medium in particle physics experiments, and is widely used in many experiments with various physics motivations, such as ICARUS [33] (neutrino detector), DUNE [34] (neutrino and proton decay detector), DarkSide (direct dark matter search detector), ATLAS [35] (calorimeter for proton-proton collider), GERDA [36] (veto detector for neutrino less double beta decay searches), and GRAMS (gamma-ray and antimatter detector on balloons and satellites). A key attribute of liquid argon is its capability to produce scintillation photons and ionized electrons in response to energy deposition. The combination of these signals provides excellent energy/position reconstruction and particle identification capabilities. However, liquid argon detectors also have various challenges, including the need for stable operation at cryogenic temperatures, the achievement of high purity, and detection of the short scintillation wavelength of 128 nm. This chapter provides an overview of the physical properties of argon as a detector medium.

2.1 Liquid argon

Table 2.1 summarizes the properties of liquid argon. Argon has boiling and freezing points of 87.3 K and 83.8 K, respectively, at 1 atm. Consequently, precise temperature control within a few Kelvin is essential for the operation of liquid argon detectors. Moreover, as the detector operates at cryogenic temperatures below 80 K, its components must be capable of withstanding low temperatures. On the other hand, these cryogenic temperatures offer several advantages: inhibiting the solidification of impurities, minimizing outgassing from the face of detector components, and reducing the thermal noise of the sensor.

Argon is present in the atmosphere at the third-highest concentration, approximately 1%, exceeding that of other noble gas elements. Unlike other noble gases, argon is cost-effective as it can be obtained as a byproduct of the production of liquid nitrogen and liquid oxygen from air. This cost-effectiveness facilitates the rapid and flexible development of detectors and the construction of large or multiple detectors.

2.2 Radioactive isotope

Atmospheric argon contains the radioactive isotope ^{39}Ar, which undergoes β^+ decay with a Q value of 565 keV and a half-life of 269 years, contributing to background events in rare event searches. According to measurements from Ref.[38], the mass fraction is $(8.0 \pm 0.6) \times 10^{-16}$ g(^{39}Ar)/g($^{\mathrm{nat}}$Ar), and the activity

Table 2.1. Properties of argon [37]

Atomic number	18
Mass number	39.948
Liquid density	1.399 g/cm^3
Boiling point at 1 atm	87.3 K
Melting point	83.8 K
Triple point	0.068 MPa, 83.8 K
Concentration in air	9340 ppm
Stable isotope	^{36}Ar (0.0034)
(abundance in air)	^{38}Ar (0.0006)
	^{40}Ar (0.9960)

in liquid argon is (1.01 ± 0.08) Bq/kg. Since ^{39}Ar is generated by cosmic rays, argon obtained from deep underground has lower ^{39}Ar levels compared to atmospheric argon, with an activity reported as 6.6 mBq/kg in Ref.[39], effectively reducing the internal background radiation from argon radioisotope.

2.3 Interaction of particles in liquid argon

Liquid argon serves as a calorimeter, producing approximately 50,000 ionized electrons or scintillation photons per 1 MeV of energy transfer. When a particle traverses through liquid argon and imparts energy into it, the energy is converted into quanta, such as scintillation photons and ionized electrons, through processes like excitation, ionization, and recombination. Figure 2.1 presents a schematic diagram illustrating the conversion process from energy deposition to observable signals. Moving particles within liquid argon deposit energy into either argon nuclei or orbital shell electrons, known as nuclear and electronic losses, respectively. As depicted in Fig. 2.2, the ratio of nuclear to electronic losses depends on the particle type and its kinetic energy. Electronic losses are predominant for light particles such as electrons, protons, as well as heavy ions with high kinetic energy. Nuclear losses dominate for low kinetic energy heavy ions and recoiled argon ions. Subsequently, recoiled argon nuclei and electrons transfer energy to other argon atoms. Consequently, the ratio of energy deposited into nuclei and electrons differs from the ratio directly given by the incident particles. The energy distributed to electronic losses excites or ionizes argon atoms, leading to the formation of excitons and electron-ion pairs. Excitons, directly excited by energy deposition or formed by recombination, deexcite by emitting scintillating photons. In an electric field, some of the ionized electrons escape recombination and drift according to the applied electric field.

2.3.1 Energy dissipation

The energy deposited into liquid argon E_0 dissipates into three channels; atomic motion, ionization, and excitation. The average number of quanta N_q, induced by energy losses, specifically, the sum of the

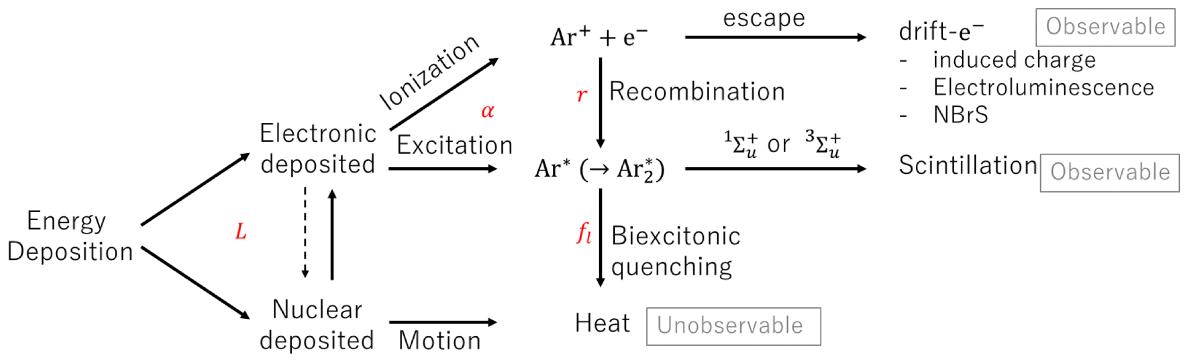

Fig. 2.1. Schematic diagram of the energy conversion process in liquid argon. The energy transferred to liquid argon is divided into ionization, excitation, and atomic motion. Ionized electrons and scintillation photons are both detectable, and atomic motion is unobservable in the current liquid argon detector.

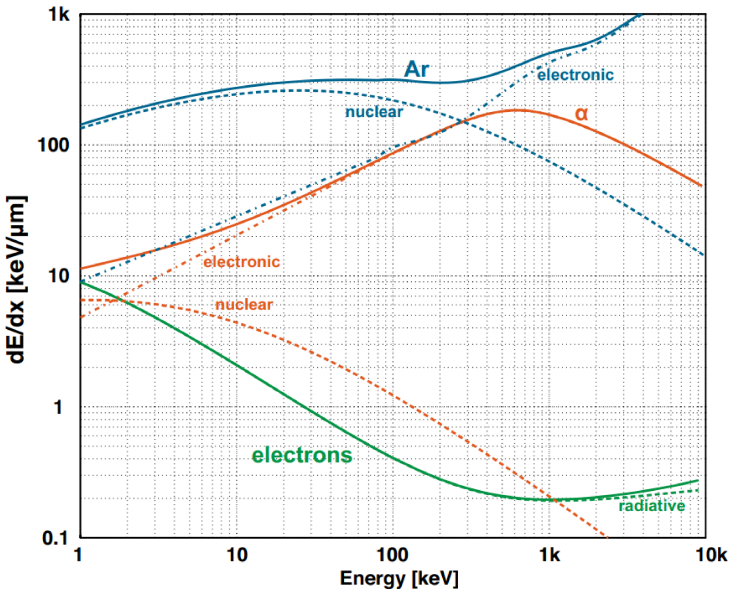

Fig. 2.2. Stopping power in the liquid argon for electron (green line), α ray (red line) and recoiled argon nuclei (blue). Solid lines represent total stopping power, and dashed lines represent contributions of electronic losses and nuclear losses. The figure is taken from Ref.[40].

number of electron-ion pair N_i and exciton N_{ex}, is expressed as follows:

$$N_q = N_{ex} + N_i = \frac{E_0 L}{W_s}, \tag{2.1}$$

where W_s is the average energy required to produce one electron-ion pair or exciton, referred to as the effective work function. A commonly used value for W_s is 19.5 eV. The parameter L represents the ratio of the energy consumed in generating quanta to the total energy loss, accounting for energy losses due to atomic motion. Defining the exciton-to-ion ratio as $\alpha \equiv N_{ex}/N_i$, N_i and N_{ex} are given by:

$$N_i = \frac{1}{\alpha + 1} \times \frac{E_0 L}{W_s}, \tag{2.2}$$

$$N_{ex} = \frac{\alpha}{\alpha + 1} \times \frac{E_0 L}{W_s}. \tag{2.3}$$

These parameters have been measured and modeled in various studies. For electronic recoil, the factor L is set to 1, and the ratio α has been measured as 0.21 [41]. For nuclear recoil, Lindhard theory [42] predicts L as a function of the dimensionless energy ϵ:

$$\begin{aligned} L &= \frac{kg(\epsilon)}{1 + kg(\epsilon)}, \\ k &= 0.133 Z^{2/3} A^{-1/2}, \\ g(\epsilon) &= 3\epsilon^{0.15} + 0.7\epsilon^{0.6} + \epsilon, \\ \epsilon &= 11.5(E_0/\mathrm{keV}) Z^{-7/3}, \end{aligned} \tag{2.4}$$

where $Z = 18$ and $A = 40$ are the atomic and mass numbers of argon, respectively. The expression for $g(\epsilon)$ is an approximation detailed in Ref.[43].

The ratio α for nuclear recoil depends on the applied electric field F and recoiled energy E_R. This has been discussed in several literature; 0.6–2.4 depending on E_R of 16.9–57.3 keV [44], 0.19 [45], 1.0 [46], or $1.3 \times \exp(-0.60 \times F\ [\mathrm{kV/cm}])$ [47]. Additionally, it has been empirically parametrized as a function of the applied electric field F in Ref.[48]:

$$\alpha = \alpha_0^{\mathrm{NR}} \exp(-D_\alpha^{\mathrm{NR}} F), \tag{2.5}$$

where α_0^{NR} and D_α^{NR} are constant values; 1.0 and $8.9^{+0.5}_{-0.4}$ $[\mathrm{V/cm^{-1}}]$, respectively.

2.3.2 Electron-ion recombination

Some of the ionized electrons recombine to form excitons, while the remaining free electrons drift or diffuse away. The recombination probability depends on the electric field and Linear Energy Transfer (LET), which represents the energy deposited to the medium per unit path length along an initial particle track. LET is a crucial parameter for understanding the response of liquid argon. A higher external electric field leads to a lower recombination probability, resulting in an increased number of electrons escaping from the binding of ions. Conversely, when LET is high, indicating a high density of ionized

electrons, the recombination probability is large due to the increased collision rate between ionized electrons and argon ions.

Recombination is considered to be rapid when the separation between ionized electron-ion pairs is such that the electric field-induced drift of charge carriers surpasses the drift caused by thermal diffusion. This crucial distance, denoted as the Onsager radius r_c, is expressed by the equation:

$$\frac{e^2}{4\pi\epsilon r_c} = k_B T, \tag{2.6}$$

where e is the elementary charge, ϵ is the dielectric constant, k_B is the Boltzmann constant, and T is the temperature. Recombination is directly proportional to the electron and ion number densities, denotes as n_+, n_-, respectively. This relationship is expressed by the equation:

$$R = \kappa n_+ n_-, \tag{2.7}$$

where κ is the recombination coefficient. The temporal evolution of the number density is described by Jaffe's diffusion equations, which are expressed as follows:

$$\frac{\partial n_+}{\partial t} = \mu_+ \boldsymbol{F} \cdot \nabla n_+ + d_+ \nabla^2 n_+ - \kappa n_- n_+, \tag{2.8}$$

$$\frac{\partial n_-}{\partial t} = \mu_- \boldsymbol{F} \cdot \nabla n_- + d_- \nabla^2 n_- - \kappa n_- n_+, \tag{2.9}$$

where $\boldsymbol{F}$ is the total electric field arising from charged carriers and the applied field, and $\mu_\pm$ are the diffusion constants. The terms on the right-hand side of each equation delineate the drift due to the electric field, diffusion, and recombination, respectively. Subsequently, we describe the treatment of short and long tracks.

The case for short track: Thomas-Imel box model

When the ionizing track length is comparable to or less than the electron thermal distance, carriers are presumed to disperse uniformly within a region characterized by the typical size of the thermal distance. With an increase in number density, the probability of recombination also rises. This phenomenon is particularly noticeable in instances such as Nuclear Recoil (NR) and low-energy Electron Recoil (ER). The Thomas-Imel box (TIB) model effectively captures and describes this process. Thomas and Imel simplify Jaffe's diffusion equations as follows [49]:

$$\frac{\partial n_+}{\partial t} = -\kappa n_- n_+, \tag{2.10}$$

$$\frac{\partial n_-}{\partial t} = -v \frac{\partial n_-}{\partial z} - \kappa n_- n_+. \tag{2.11}$$

The external electric field is considered only in the -z direction, and the drift velocity is assumed as $\boldsymbol{v} = (0, 0, -v) = \mu_- \boldsymbol{F}$. Given that the diffusion of electrons is sufficiently smaller than the drift induced by the external electric field in liquid argon, the second term in Eq. 2.9 is omitted. Additionally, both the

diffusion and drift velocities of ions are also smaller compared to electrons, leading to the neglect of the first and second terms in Eq. 2.8.

As a boundary condition, TIB model assumes that ions or ionized electrons exist with a uniform density within a square of side length $2a$ at the initial state:

$$n_{\pm}(t=0) = \begin{cases} \frac{N_0}{8a^3} & |x|, |y|, |z| < a, \\ 0 & otherwise, \end{cases} \tag{2.12}$$

where N_0 represents a total number of electron or ion provided as $\int dx^3 n_{\pm}(\boldsymbol{x}, t=0) = N_{\pm}$. Substituting Eq. 2.12 into Eqs. 2.11 and 2.10, and taking the limit $t \to \infty$, the recombination probability is given as follows:

$$r = 1 - \frac{n_-(t=\infty)}{N_0} = 1 - \frac{1}{\xi}\ln(1+\xi), \tag{2.13}$$

$$\xi = \frac{N_0 \kappa}{4a^2 \mu_- F}. \tag{2.14}$$

The case for long track: Doke-Birks ' s model

In the case of long tracks, such as those produced by charged particles or high-energy ER events, the Doke-Birks's model provides a good description. Electron-ion pairs are generated along the trajectory of ionizing particles, forming a columnar distribution. In this model, the diffusion and drift terms in Jaffe's equations are omitted, leading to the following simplified form:

$$\frac{\partial n_+}{\partial t} = \frac{\partial n_-}{\partial t} = -\alpha' n_- n_+. \tag{2.15}$$

The electrons and ions are assumed to distribute uniformly within a unit length dx along the trajectory. Additionally, since the number of ionized electrons and ions is the same,

$$\frac{\partial n_{\pm}}{\partial t} = -\alpha' n_{\pm}^2. \tag{2.16}$$

The integration of Eq. 2.16 until an appropriate time τ when recombination occurs leads to the following expression:

$$R = S \int_0^{\tau} -\frac{dN}{dt} dt = \frac{S N_0^2 \alpha' \tau}{1 + N_0 \alpha' \tau}, \tag{2.17}$$

where R is the number density of recombined electron-ion pairs, S is the cross-sectional area of the ionization column, and $N_0 \equiv N_{\pm}(t=0)$. Assuming that the initial number of ionized electrons or ions N_0 is proportional to dE/dx, recombination probability is given as follows with constants A and B:

$$r = \frac{R}{N_0} = \frac{SK\alpha'\tau(dE/dx)}{1 + K\alpha'\tau(dE/dx)} = \frac{A(dE/dx)}{1 + B(dE/dx)}. \tag{2.18}$$

Additionally, a correction term is added based on the measurement from heavy ion beam tests by Doke et al. as follows:

$$r = \frac{A(dE/dx)}{1 + B(dE/dx)} + C, \quad B = \frac{A}{1 - C}. \tag{2.19}$$

The parameters A and C are determined from experimental results. Figure 2.3 shows the relative scintillation yield of liquid argon as a function of LET.

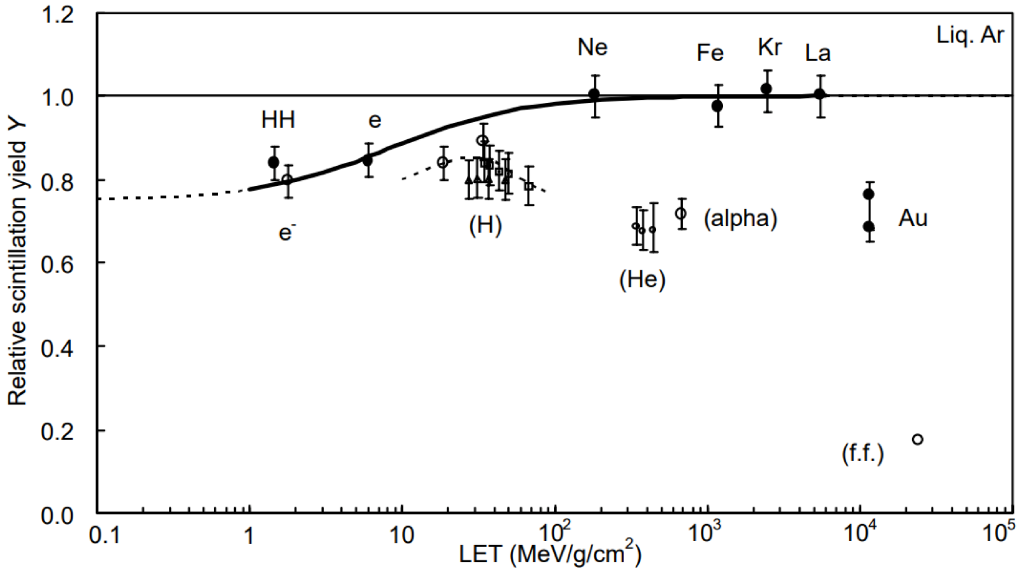

Fig. 2.3. Relative scintillation yield of liquid argon measured using various ion beam as a function of linear energy transfer. Open circles represent non-relativistic particles, and solid circles represent relativistic particles. The result marked with e^- is the 1 MeV electron point. This point corresponds to 41 photon/keV since the maximum scintillation yield is 1/W=51.2 photon/keV. The figure is taken from Ref.[50].

2.3.3 Drift electron

In the presence of an external electric field, some ionized electrons escape recombination and move along the electric field. Since argon is a closed-shell atom and does not adsorb free electrons, these free electrons can drift over long distances. These free electrons move at a constant velocity as a result of repetitive acceleration by the electric field and collisions with surrounding argon atoms. Figure 2.4 depicts the electron drift velocity in liquid argon, as a function of the applied electric field represented on the horizontal axis. The higher the electric field, the greater the drift velocity.

Impurities with electronegativity, such as oxygen and water, adsorb free electrons, resulting in a reduction of the ionized electron signal. The lifetime of free electrons is contingent on the electronegativity of

impurities and their concentration. For instance, in the case of oxygen, the lifetime of free electrons is directly proportional to the level of contamination and is approximately 300 µs/1ppb. Captured electrons are subsequently released and undergo drift.

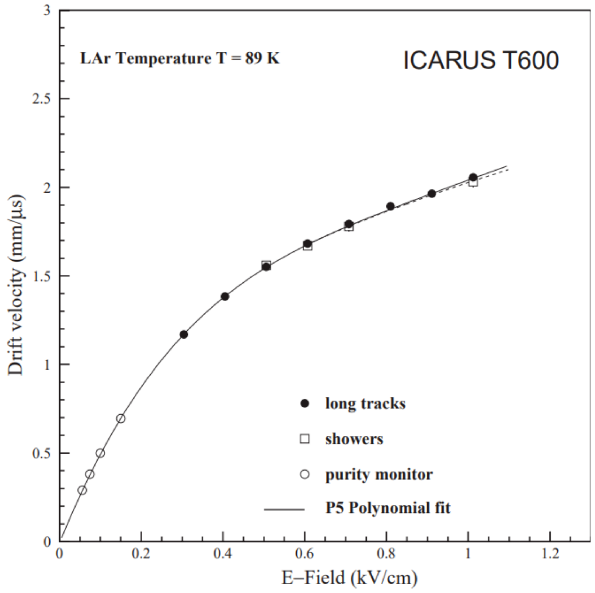

Fig. 2.4. Drift velocity of electrons in liquid argon measured in the ICARUS T600 TPC. The figure is taken from Ref.[51].

2.3.4 Excitation and de-excitation in liquid argon

The primary component of argon scintillation is vacuum ultraviolet light with a wavelength of 128 nm emitted as a result of de-excitation of excimer Ar_2^* (referred to as the "second continuum"). Figure 2.5 displays the emission wavelengths of liquid argon scintillation measured in experiments utilizing ion beams. The blue line represents the spectrum when irradiated with a proton beam, the green line with a gold ion beam, and the red line with a sulfur ion beam. The de-excitation of excimer Ar_2^* around 128 nm is the most intense and dominant for all types of beam particles. The peak around 150 nm is attributed to components derived from xenon mixed in argon.

The formation and de-excitation of Ar_2^* occur through two processes, direct excitation and recombination process, as follows:

$$\begin{aligned} Ar + E &\rightarrow Ar^* \\ Ar^* + 2Ar &\rightarrow Ar_2^* + Ar \\ Ar_2^* &\rightarrow 2Ar + h\nu\ (128\text{nm}) \end{aligned} \tag{2.20}$$

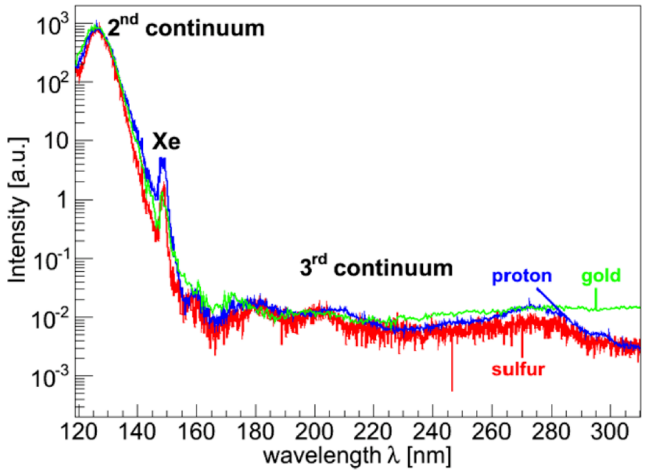

Fig. 2.5. The emission wavelengths of liquid argon scintillation measured in experiments utilizing various ion beams; a proton beam (blue line), a gold ion beam (green line), and a sulfur ion beam (red). The figure is taken from Ref.[52].

and,

$$\begin{aligned} \mathrm{Ar} + \mathrm{E} &\rightarrow \mathrm{Ar}^{+} + \mathrm{e}^{-} \\ \mathrm{Ar}^{+} + \mathrm{Ar} &\rightarrow \mathrm{Ar}_2^{+} \\ \mathrm{Ar}_2^{+} + \mathrm{e}^{-} &\rightarrow \mathrm{Ar}^{**} + \mathrm{Ar} \\ \mathrm{Ar}^{**} &\rightarrow \mathrm{Ar}^{*} + \mathrm{E}_{\mathrm{heat}} \\ \mathrm{Ar}^{*} + 2\mathrm{Ar} &\rightarrow \mathrm{Ar}_2^{*} + \mathrm{Ar} \\ \mathrm{Ar}_2^{*} &\rightarrow 2\mathrm{Ar} + h\nu \ (128\mathrm{nm}) \end{aligned} \tag{2.21}$$

The argon excimer includes a singlet excited state ($^1\Sigma_u^+$) and a triplet excited state ($^3\Sigma_u^+$). Most of the Ar_2^* produced in the process of Eq. 2.20 is in the singlet state, as the spin of the excited electron and the nuclear system to which electron is bound are in opposite directions. On the other hand, in Eq. 2.21, argon ions and electrons can have the same spin orientation since the electrons are ionized once. Therefore, both singlet and triplet states are produced. Additionally, the singlet state changes to the triplet state by interaction with free electrons, as expressed by the reaction:

$$\mathrm{Ar}_2^{*}(^1\Sigma_u^+) + \mathrm{e}^{-} \rightarrow \mathrm{Ar}_2^{*}(^3\Sigma_u^+) + \mathrm{e}^{-} \tag{2.22}$$

The lifetimes of scintillation differ for each state, and in the case of liquid argon, $^1\Sigma_u^+$ has a lifetime of approximately 6 ns, while $^3\Sigma_u^+$ has a lifetime of approximately 1.5 µs [53]. The scintillation time profile is characterized by the ratio of the two states, and this ratio depends on the LET, i.e., the type of incident particles. Figure 2.6 shows the average waveforms of liquid argon scintillation obtained at the liquid argon test stand at Waseda University. The black line represents the waveform of an ER event, and the red line represents an waveform of a NR event. There are two lifetime components: singlet and triplet states,

and the ratio of the triplet component is smaller in NR than in ER; this allows for particle identification, a technique known as Pulse Shape Discrimination (PSD). The practical application of this PSD will be discussed in Section 3.2.1.

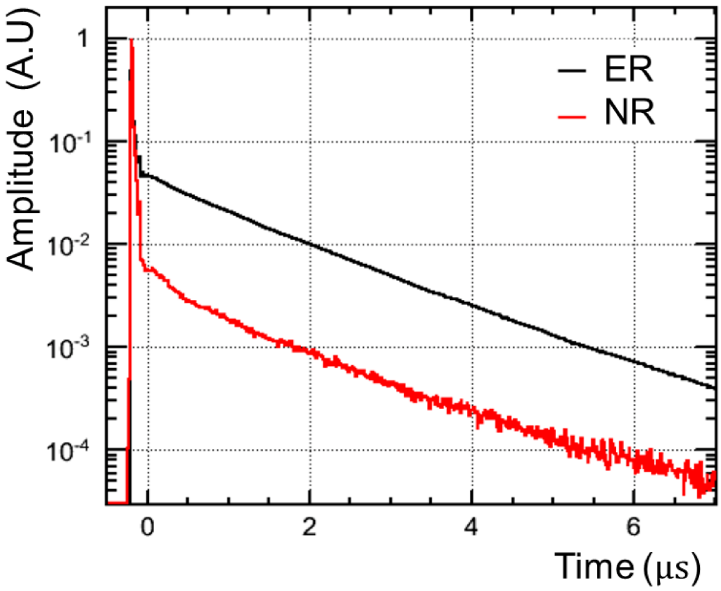

Fig. 2.6. Average waveforms of liquid argon scintillation induced from electron recoil (black line), and from nuclear recoil (red line). Both waveforms are normalized so that the peak values are set to 1.

Figure 2.7 shows the scintillation yield of liquid argon in a no-electric-field environment as a function of the incident energy of gamma ray. Since the recombination probability changes with LET, the scintillation yield exhibits an energy dependence.

In the case of NR, the LET is larger than that of ER, resulting in a dense distribution of excimers. Therefore, the scintillation yield decreases in NR compared to ER through the following process:

$$Ar^* + Ar^* \rightarrow Ar^+ + Ar + e^- \tag{2.23}$$

The ionized electrons generated in this process promptly undergo recombination, rendering them undetectable as ionized electron signals. Figure 2.8 illustrates the scintillation efficiency referenced to a 511 keV ER event measured under electric fields ranging from 0 to 3 kV/cm as a function of the recoil energy.

Impurities such as oxygen or nitrogen, when mixed with liquid argon, induce the de-excitation of excimers without emitting photons through the following processes:

$$\begin{aligned} Ar_2^* + O_2 &\rightarrow 2Ar + O_2 \\ Ar_2^* + N_2 &\rightarrow 2Ar + N_2 \end{aligned} \tag{2.24}$$

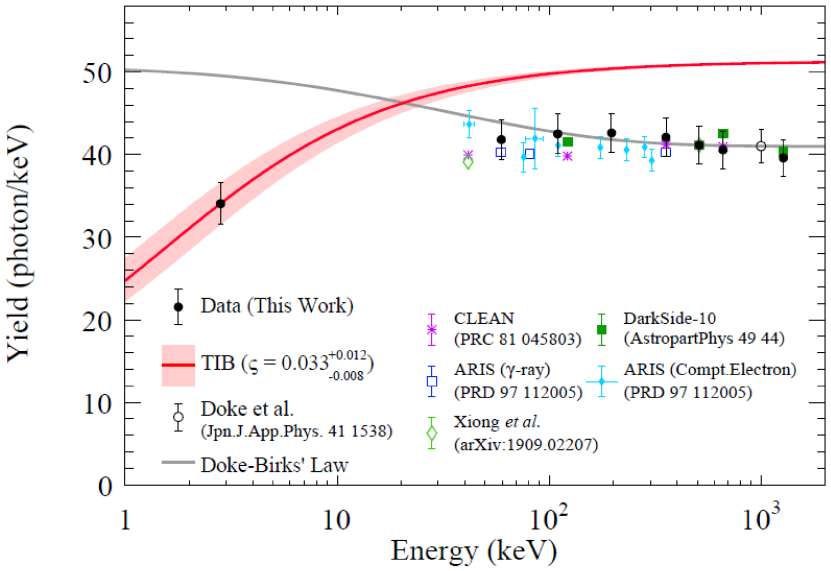

Fig. 2.7. Measured scintillation yield of liquid argon in a no-electric-field environment as a function of gamma ray energy. The figure is taken from Ref.[54].

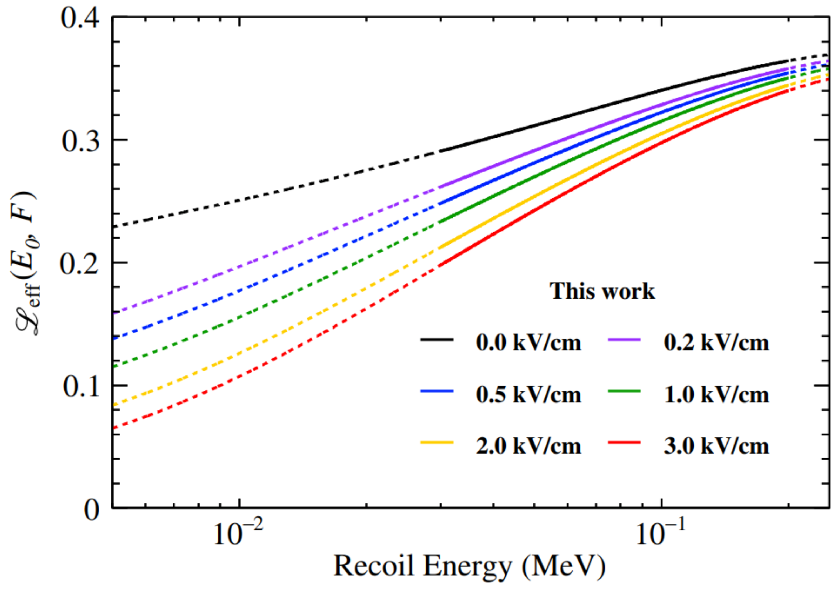

Fig. 2.8. The scintillation efficiency of NR event referenced to 511 keV ER event. The horizontal axis represents the NR energy. The solid lines are the results and dashed lines represent extrapolations. This figure is taken from Ref.[48].

Notably, the triplet state, which has a longer lifetime, is more strongly affected than the singlet state. Figure 2.9 shows the measured lifetime of liquid argon scintillation with different impurity concentrations: O_2 on the left and N_2 on the right. The horizontal axis indicates the impurity concentration, and the vertical axis indicates the lifetime. Changes in scintillation lifetime are observed with oxygen and nitrogen impurity concentrations, respectively.

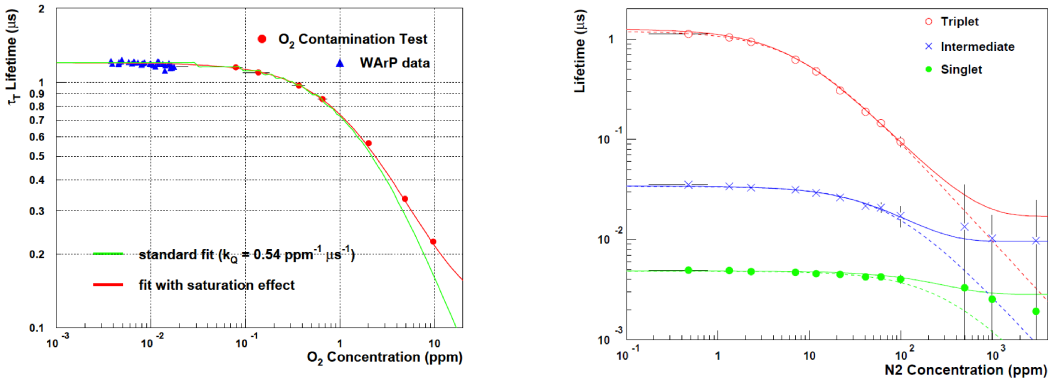

Fig. 2.9. The variation in scintillation lifetime of liquid argon triplet component due to impurity contamination. Left plots represent a contribution of O_2 taken from Ref.[55], and right plot represent a contribution of N_2 taken from Ref.[56].

2.3.5 Fano factor in liquid argon

The fluctuation in the number of quanta produced by the incident ionizing particle is an important parameter that determines the limit of the energy resolution. The standard deviation of the ionized electron produced does not follow simple Poisson statistics, but is given by

$$\sigma = \sqrt{F \cdot \bar{N}} \tag{2.25}$$

where F is the Fano factor and $\bar{N}$ is the average number of produced ionized electrons. The Fano factor of liquid argon has not been measured, but it has been estimated approximately 0.1 theoretically by F. Doke [57]. This is due to the fact that the production of excitons and ionized electrons in liquid argon are not independent of each other. In the Ref.[57], the Fano factor is written as follows:

$$F = \frac{\bar{N}_{ex}}{\bar{N}_i}\left(1 + \frac{\bar{N}_{ex}}{\bar{N}_i}\right)\frac{\bar{E}_{ex}^2}{W^2} + \frac{\overline{(\epsilon_i - \bar{E}_i - \bar{\epsilon})^2}}{W^2} + \frac{\bar{N}_{ex}}{\bar{N}_i}\frac{\overline{(\epsilon_{ex} - \bar{E}_{ex})}}{W^2}, \tag{2.26}$$

where $\bar{N}_a$ is the number of collisions with reaction a (excitation or ionization), ϵ_i is the energy loss due to ionization, $\bar{E}_i + \bar{\epsilon}$ is their average value, $\bar{E}_i$ is the average ionization energy, $\bar{\epsilon}$ is the energy loss as electron kinetic energy, $\bar{\epsilon}_{ex}$ is the energy loss due to excitation, and $\bar{E}_{ex}$ is the average excitation energy. Here, the first term corresponds to the fluctuations in whether ionization or excitation occurs, and the second and third terms correspond to the fluctuations in the energy loss during each collision. Because

$\bar{N}_{ex}/\bar{N}_i$ is small, the Fano factor is also small.

2.4 Luminescence in gaseous argon

2.4.1 Gaseous argon scintillation

Figure 2.10 displays the emission wavelength spectrum of gaseous argon scintillation measured in experiments utilizing proton beams. The blue line represents the spectrum for liquid argon, and the red line represents that for gaseous argon. Gaseous argon scintillation encompasses ultraviolet light with wavelengths between 170 and 300 nm and infrared light beyond 700 nm, in addition to the 128 nm, known as the 'second continuum'. The emission process of the infrared component is well-known and arises from the de-excitation of argon atoms, as follows:

$$\mathrm{Ar}^*(3\mathrm{p}^5 4\mathrm{p}^1) \rightarrow \mathrm{Ar}^*(3\mathrm{p}^5 4\mathrm{s}^1) + h\nu \ (\mathrm{IR} : 700 - 850\ \mathrm{nm}). \tag{2.27}$$

On the other hand, the emission process of ultraviolet light in the range of 170–300 nm is not well-understood. It is speculated that this emission, which is suppressed in the scintillation of liquid argon, may originate from transitions of highly-ionized argon ions, hereinafter referred to as the 'third continuum' [58]. The process can be explained as follows:

$$\mathrm{Ar}_2^{2+} \rightarrow 2\mathrm{Ar}^+ + h\nu \ (\mathrm{UV} : 170 - 300\ \mathrm{nm}). \tag{2.28}$$

The gaseous scintillation spectrum has been measured, and its luminous intensity has also been studied. In this dissertation, we will subsequently refer to gaseous scintillation, including the second continuum, third continuum, and infrared, as 'ordinary electroluminescence (ordinary EL)'.

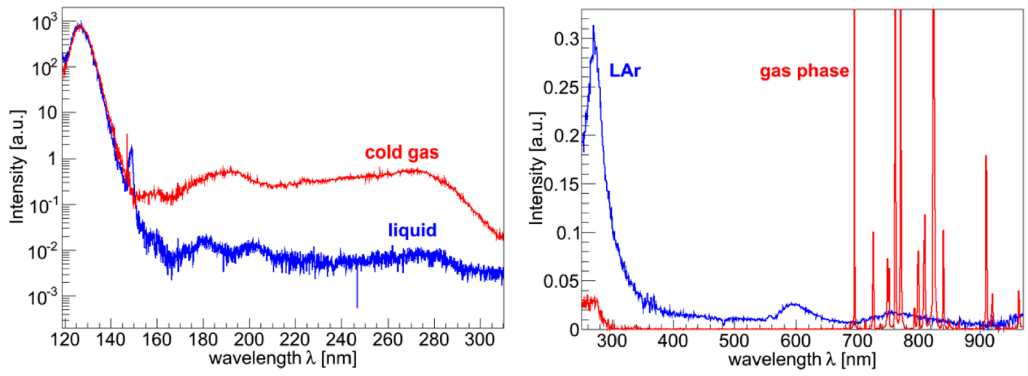

Fig. 2.10. The emission wavelength spectrum of gaseous (red line) and liquid (blue line) argon scintillation measured in experiments utilizing a proton beam. These figure is taken from Ref.[52].

In addition to ordinary EL, luminescence due to impurities has also been observed. For instance, Fig. 2.11 displays the results of wavelength measurements for argon-nitrogen gas mixtures. The measurements

were conducted using an ^{241}Am α source as the light source while varying the amount of nitrogen mixed with argon gas. The visible light emissions (300–450 nm) for the argon-nitrogen gas mixture due to the nitrogen excimer are given by the following process:

$$\mathrm{Ar}^* + \mathrm{N}_2 \rightarrow \mathrm{Ar} + \mathrm{N}_2^*(\mathrm{C}^3\Pi_\mathrm{u}), \tag{2.29}$$

$$\mathrm{N}_2^*(\mathrm{C}^3\Pi_\mathrm{u}) \rightarrow \mathrm{N}_2^*(\mathrm{B}^3\Pi_\mathrm{g}) + h\nu\ (300-450\ \mathrm{nm}). \tag{2.30}$$

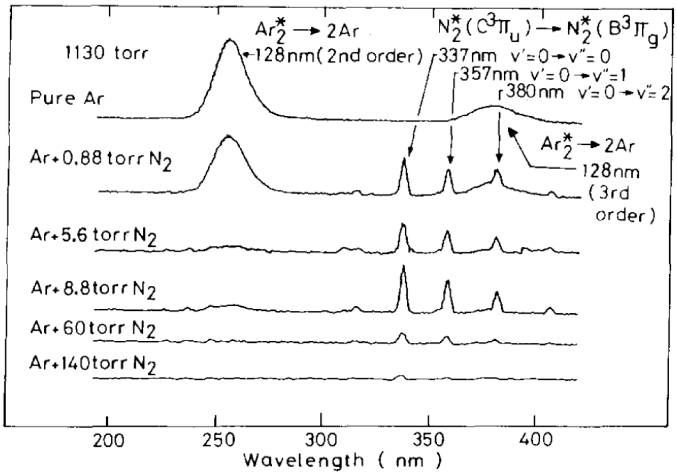

Fig. 2.11. Emission wavelength measurements of argon-nitrogen (Ar-N_2) gas mixtures. The figure is taken from Ref.[59].

2.4.2 Neutral bremsstrahlung

In addition to ordinary EL and the luminescence resulting from the impurity effect, recent studies have proposed a novel form of luminescence known as Neutral Bremsstrahlung (NBrS). This phenomenon is interpreted as bremsstrahlung, arising from the interaction of slow electrons, typically in the O(1–10) eV, recoiling from neutral atoms.

Figure 2.12 illustrates schematic diagrams for several types of bremsstrahlung. Bremsstrahlung resulting from fast electrons penetrating matter is well understood as the interaction between the electric field of the nucleus and electrons (top left in Fig. 2.12). We will refer to the bremsstrahlung produced by this mechanism as ordinary bremsstrahlung, abbreviated as 'OBrS' hereafter. Additionally, polarization bremsstrahlung (PBrS) is known to occur when a fast electron recoils from an electron associated with an atom. This interaction induces a temporary dipole moment in the atom, and the intensity and direction of polarization vary with time, giving rise to bremsstrahlung (top right in Figure 2.12) [60].

On the other hand, theoretical and experimental studies in Ref.[61] suggest that NBrS is believed to be generated by the scattering of relatively slow electrons at 1-10 eV with electrically neutral atoms. The following descriptions of NBrS are based on the findings in Ref.[61]. The bottom of Fig. 2.12 illustrates

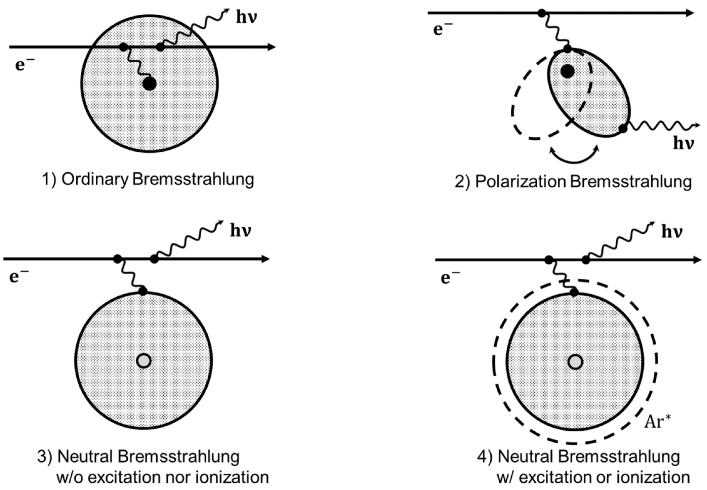

Fig. 2.12. Schematic diagrams illustrating different types of bremsstrahlung. Top left is OBrS, top right is PBrS, bottom left is NBrS without excitation, bottom right is NBrS with excitation.

schematic diagrams of scattering accompanied by excitation (in-elastically, on the right) and without it (elastically, on the left). The differential cross sections of NBrS for inelastic scattering, denoted as $(\frac{d\sigma}{d\nu})_{exc}$, and elastic scattering, denoted as $(\frac{d\sigma}{d\nu})_{el}$, are given as follows, respectively:

$$\begin{aligned}(\frac{d\sigma}{d\nu})_{exc} &= \frac{8}{3}\frac{r_e}{c}\frac{1}{h\nu} \\ &\times\Big[\Big(\frac{E-E_{exc}-h\nu}{E-E_{exc}}\Big)^{1/2}(E-E_{exc}-h\nu)\,\sigma_{exc}(E) \\ &+\Big(\frac{E-h\nu}{E}\Big)^{1/2}E\,\sigma_{exc}(E-h\nu)\Big],\end{aligned} \tag{2.31}$$

$$\begin{aligned}(\frac{d\sigma}{d\nu})_{el} &= \frac{8}{3}\frac{r_e}{c}\frac{1}{h\nu}\Big(\frac{E-h\nu}{E}\Big)^{1/2} \\ &\times\Big[(E-h\nu)\,\sigma_{el}(E)+E\,\sigma_{el}(E-h\nu)\Big]\end{aligned} \tag{2.32}$$

where r_e represents the classical electron radius defined as e^2/m_ec^2 with electron mass m_e and speed of light c, E and E_{exc} represent the initial electron energy and excitation energy, and $h\nu$ is the photon energy. σ_{exc} and σ_{el} are the electron-argon atom cross sections as a function of electron energy, provided in the left panel of Fig. 2.13. The light yield of NBrS, denoted as $\left(\frac{Y_{EL}}{N}\right)_{NBrS}$, is defined as the number of emitted photons per electron per atomic density per drift length, expressed in photons cm^2/electron/atom. The definition is given by the following integral equation:

$$\Big(\frac{Y_{EL}}{N}\Big)_{NBrS} = \int_{\lambda_1}^{\lambda_2}\int_{h\nu}^{\infty}\frac{v_e}{v_d}\frac{d\sigma}{d\nu}\frac{d\nu}{d\lambda}\,f(E)\,dE\,d\lambda \tag{2.33}$$

where v_e represents the electron velocity, v_d is the drift velocity of electron, λ_1 and λ_2 are the sensitive region of the detector, $d\nu/d\lambda = -c/\lambda^2$, and $f(E)$ is the standardized energy distribution function of

electron. Subsequently, the wavelength spectrum is given in (photon cm^2/electron/atom/nm) as follows:

$$\frac{d(Y_{EL}/N)_{NBrS}}{d\lambda} = \int_{h\nu}^{\infty} \frac{v_e}{v_d} \frac{d\sigma}{d\nu} \frac{d\nu}{d\lambda} f(E)\, dE \tag{2.34}$$

The center and right panels of Fig. 2.13 display the anticipated wavelength spectrum and light intensity, respectively, induced by the drift electron under an electric field in gaseous argon. It is expected to exhibit a continuous spectrum within the visible light range and is induced by a lower electric field compared to ordinary EL.

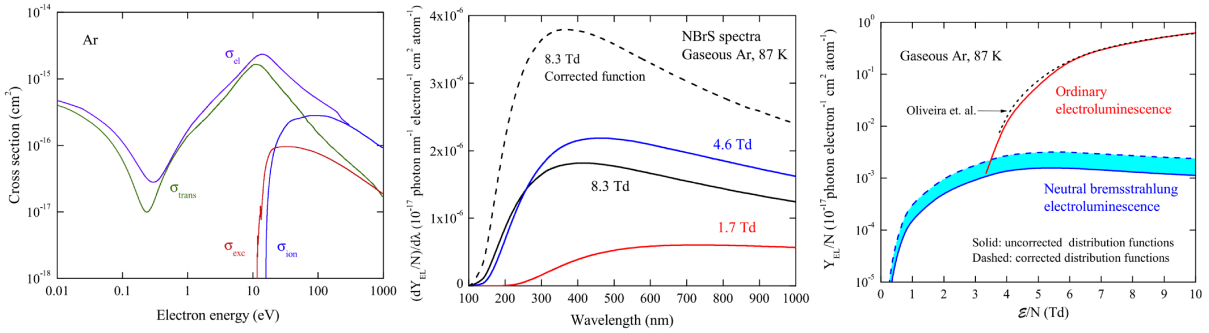

Fig. 2.13. Theoretical predictions for NBrS in gaseous argon. The left panel illustrates the electron-argon atom cross sections as a function of electron energy. The center and right panels show the anticipated wavelength spectrum and light intensity, respectively. The expected spectrum exhibits a continuous range within the visible light range, induced by a lower electric field compared to ordinary EL. These figures are taken from Ref.[61].

Figure 2.14 presents experimental results for electroluminescence yield in the gaseous phase of a double-phase liquid argon Time Projection Chamber, as measured in Ref.[61]. Both plots in Fig. 2.14 represent the same data; the right plot is displayed on a logarithmic scale for the vertical axis. Hollow square markers depict observations using a PMT with wavelength shifting, sensitive to vacuum ultraviolet photons, i.e., ordinary EL. Black circle markers represent observations using a PMT insensitive to VUV. This measurement confirms luminescence in the visible light region, even below the threshold of ordinary EL.

NBrS is expected to be a more easily detectable emission component due to its anticipated wavelength within a continuous spectrum of visible light. However, its wavelength spectrum has not been experimentally measured. The measurement of NBrS constitutes one of the primary subjects of this dissertation, discussed in Chapter 6.

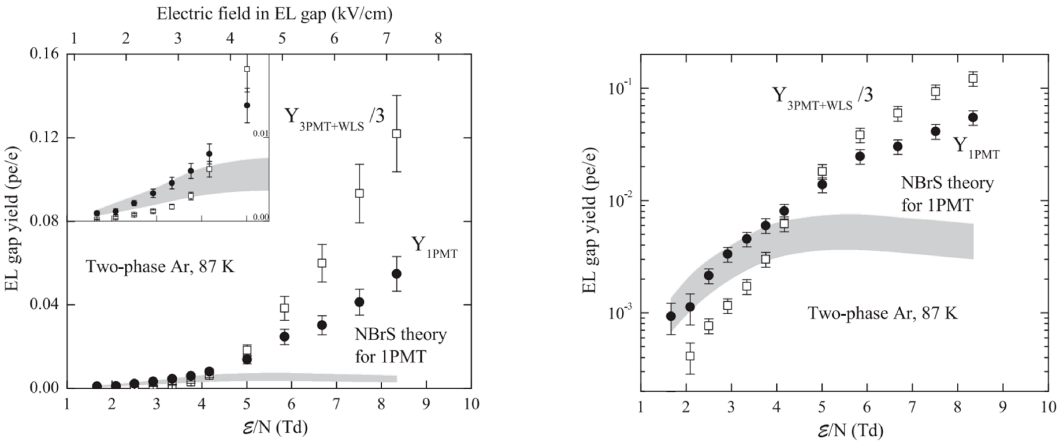

Fig. 2.14. Experimental results of electroluminescence yield as a function of the reduced electric field E/N in the gaseous phase of a double-phase liquid argon TPC. Hollow square markers represents for observations using a PMT with wavelength shifting (sensitive to vacuum ultraviolet photons, i.e., ordinary EL) and black circle markers represents observations using a PMT insensitive to VUV. Both plots represent the same data, with the right plot displayed on a logarithmic scale for the vertical axis. This figure is taken from Ref.[61].

CHAPTER 3

Liquid argon detectors in particle physics experiment

Liquid argon detectors detect either scintillation light or ionized electron signals, or both, facilitating the reconstruction of reaction position, energy, and other parameters. This chapter provides an overview of the operational principles of liquid argon detectors and discusses the challenges in their development. Among the various challenges, the detection of light signals is crucial for the operation of liquid argon detectors, significantly impacting detector performance. Therefore, this study focuses on challenges related to light signals. The specific focus of the dissertation is detailed at the end of this chapter.

3.1 Operation principle

The existing liquid argon detectors can be broadly classified into three types. Figure 3.1 illustrates schematics of the Single-Phase Scintillation detector, Single-Phase Time Projection Chamber, and Double-Phase Time Projection Chamber, respectively, from left to right.

Single-Phase Scintillation detector (SP-Sci): In single-phase scintillation detectors, the sensitive area is filled with liquid argon, and scintillation light generated by interactions with incident particles is detected. The reaction position is reconstructed based on the distribution of scintillation photons detected by each photo-detection device. Since the design prevents the generation of an electric field within the sensitive region, the probability of recombination of ionized electrons is high, resulting in a larger scintillation yield compared to other detector types. This design offers advantages in terms of the energy resolution of the scintillation signal and the PSD capability.

Single-Phase Time Projection Chamber (SP-TPC): The sensitive area is filled with liquid argon, and an electric field is applied in this region to induce the drift of ionized electrons. This configuration allows the detection of both scintillation light and ionized electron signals. The trajectory or recoil position of the incident particle is determined by the hit pattern of the ionized electron signal and the difference in detection time between the scintillation photon and the ionized electron. Subdividing the anode electrodes enables a position resolution of several millimeters. However, achieving high energy resolution for low-energy events is challenging due to the small number of ionized electrons and the difficulty of amplifying electrons in liquid argon.

Double-Phase Time Projection Chamber (DP-TPC): A double-phase TPC consists of a liquid phase and an upper gaseous phase. In addition to a drift electric field that guides ionized electrons toward the gaseous phase, an extraction electric field larger than that drift electric field is formed across the

liquid surface. Ionized electrons drifting to the liquid surface are transferred to the gaseous phase by the extraction electric field, leading to the excitation of gaseous argon and subsequent photon emission in gaseous phase, known as electroluminescence. Both the scintillation light emitted when incident particles recoil with argon (referred to S1 hereafter) and the electroluminescence at the gas phase (referred to S2 hereafter) are detected. The reaction position of the incident particle is determined by the distribution of detected S2 photons for each photo-detection device in the XY direction, and by the difference in detection time between S1 and S2 in the Z direction. While the XY position resolution is inferior to that of a single-phase TPC, the light yield in the gaseous phase is ranges from several tens to hundreds of photons per electron, enabling detection from a recoil energy equivalent to a single electron.

Additionally, a GEM/LEM-based method for amplifying and reading out drift electrons in the gas phase is under development [62]. This is expected to provide better spatial resolution than electroluminescence.

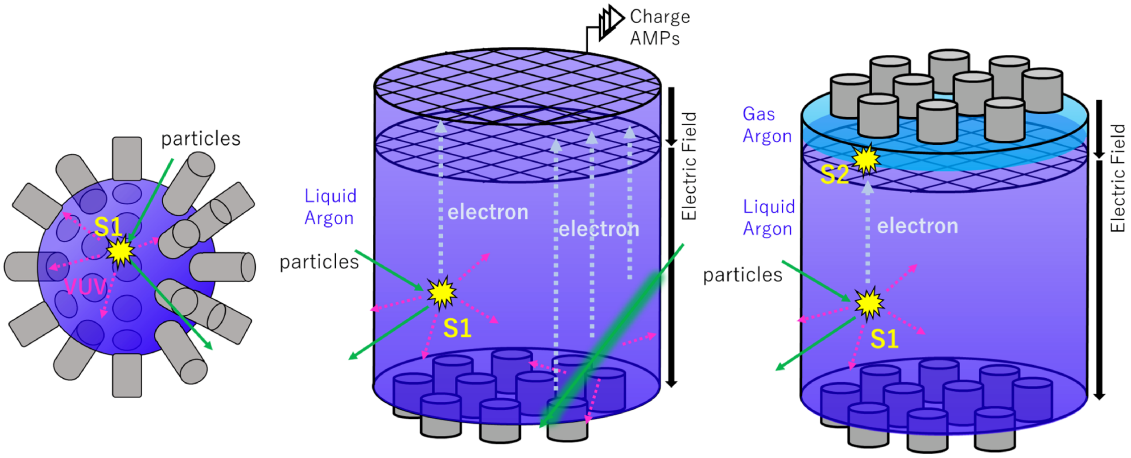

Fig. 3.1. Schematics of various liquid argon detectors, including the Single-Phase Scintillation detector (left), Single-Phase Time Projection Chamber (center), and Double-Phase Time Projection Chamber (right).

3.2 Particle identification

The liquid argon detector possesses particle identification capabilities derived from the distinctive characteristics of signals depending on incident particle types. In the subsequent sections, we describe particle identification through parameters including the singlet/triplet ratio (PSD), ionization/scintillation ratio (S2/S1), and dE/dX.

3.2.1 Pulse shape discrimination (PSD)

In a straightforward approach, the PSD parameter can be calculated as a percentage of the scintillation signal remaining after the singlet is nearly completely de-excited. Hereafter, the PSD parameter Slow/Total

is defined as Slow/Total= L_{slow}/L_{total}, where L_{total} represents the total detected scintillation signal, and L_{slow} represents the signal observed after t=120 ns.

The left panel of the Fig. 3.2 illustrates Slow/Total as a function of detected number of photoelectrons, effectively separating ER and NR. This data was acquired using a liquid argon detector with a photon collection efficiency of 5.7 p.e./keVee, where keVee stands for keV electron equivalent. The mean values of Slow/Total for ER and NR converge at small recoil energies.

As the deviation of Slow/Total becomes smaller with higher number of detected photons, depending on stochastic nature, PSD capability increases with improved light collection efficiency. The right panel of Fig. 3.2 shows PSD distributions obtained with a detector featuring a light collection efficiency of 5.7 p.e./keVee for the black line and 12.8 p.e./keVee for the red line, both corresponding to about 10 keVee. It is evident from the figure that the 12.8p.e./keVee detector exhibits smaller deviation and higher PSD power.

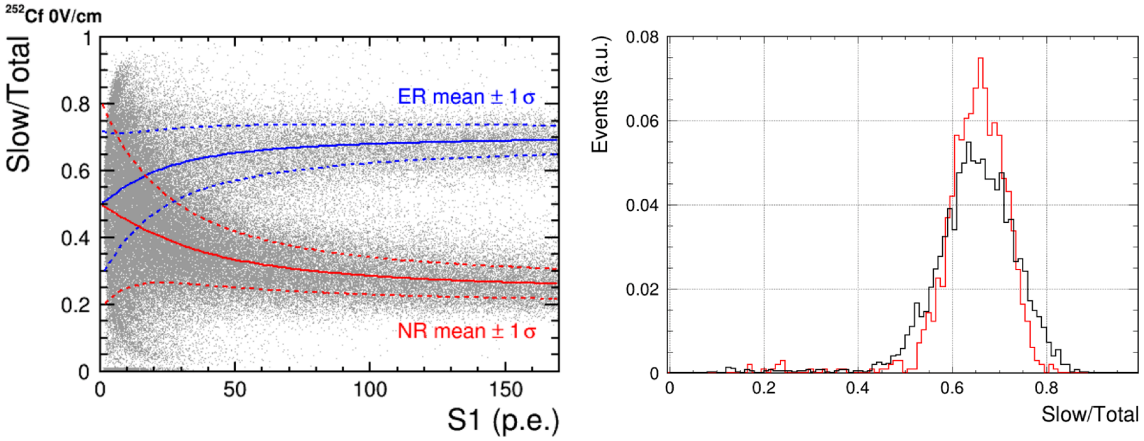

Fig. 3.2. (left) Distribution of Slow/Total as a function of detected number of photoelectrons. ER events and NR events are well-separated. The left panel is taken from Ref.[47]. (right) Slow/Total distributions corresponding to approximately 6 keVee. The black line represents Slow/Total obtained with 5.7 p.e./keVee detector, while the red line represents Slow/Total obtained with 12.8 p.e./keVee detector.

3.2.2 Scintillation/ionization ratio (S2/S1)

The ionized electron and scintillation ratio distinguish ER and NR as the recombination probability depends on the LET. The recombination probability is also influenced by the external electric field, leading to a dependency on the drift electric field. Many experiments utilize $\log_{10}(S2/S1)$ as a parameter for particle identification. Figure 3.3 shows the S2/S1 distribution of NR and ER with the drift electric field of 1 kV/cm, where ER and NR events are well-separated. On the other hand, the application of a drift electric field reduces the scintillation and the PSD capability. The study in Ref.[47] shows that the highest separation capability is achieved when S1 PSD is used with no electric field.

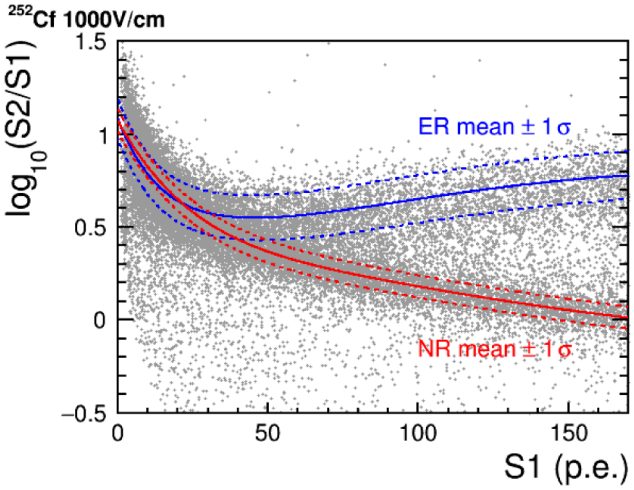

Fig. 3.3. Distribution of $\log_{10}(S2/S1)$ for NR and ER with the drift electric field of 1 kV/cm, obtained using ^{252}Cf. The figure is taken from Ref.[47].

3.2.3 dE/dX along a particle track

Charged particles moving through matter lose energy according to the Bethe-Bloch equation. The rate of energy loss, dE/dX, depends on the velocity and charge of the particle. The single-phase TPC can reconstruct dE/dX along the particle trajectory, and this information is valuable for particle identification. Fig. 3.4 makes it clear that the separation of muons and protons based on their respective energy depositions is enabled. This measurement was obtained with the proto-DUNE detector [63], showcasing the dE/dX along the tracks of a proton and muon stopped in the detector, with the horizontal axis representing the distance from the stopping point

3.3 Signal detection technique

The detection of liquid argon signals involves different techniques for photons and electrons in gaseous and liquid phases. Table 3.1 provides the necessary technologies, with each component discussed below.

Table 3.1. Required technologies for detecting signals in liquid argon detectors

phase	to detect photons	to detect electrons
Liquid	· VUV sensitive photo-devices · Wavelength downshifting to visible light and VL sensitive photo-device	· Multi-channel & Low-noise cold electronics
Gaseous	· Well-controlled S2 amplification · VUV sensitive photo-devices · Wavelength downshifting to visible light and VL sensitive photo-device	· Electron amplification in gas phase such as GEM and LEM · Multi-channel electronics

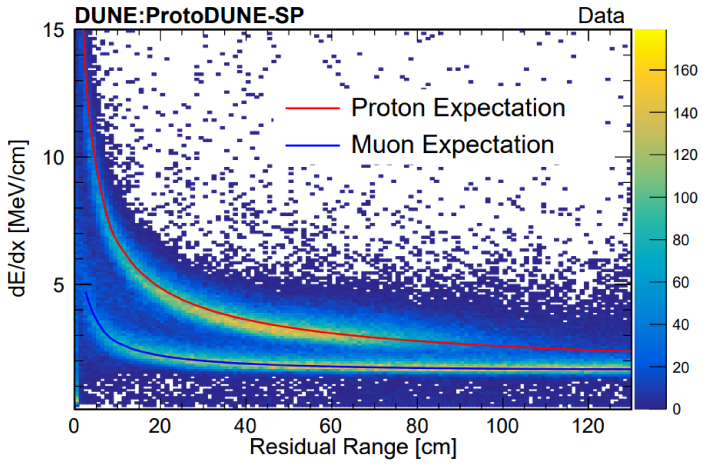

Fig. 3.4. The dE/dX along the track of stopped protons and muons in the detector, plotted as a function of the distance from the stopping point. The data is measured in proto-DUNE detector. The figure is taken from Ref.[63].

3.3.1 Detection of argon scintillation

Argon scintillation signals are detected using photon-detection devices capable of single-photon detection, such as a PMT or a Multi Pixel Photon Counter (Hamamatsu Photonics K.K., MPPC). In the case of a PMT, the sensitivity threshold on the short-wavelength side depends on the transmittance of the PMT window material. Figure 3.5 displays the emission wavelengths of noble gases and the transmittance of materials used as PMT windows. The black dashed line represents the transmittance of MgF_2, and the solid blue line represents the spectrum of liquid argon scintillation. PMTs using MgF_2 as a window material exhibit sensitivity to liquid argon scintillation. The Quantum Efficiency (QE), which is the ratio of the number of photoelectrons ejected from the material to the number of photons incident on the window, for PMTs with MgF_2 windows, operational at liquid argon cryogenic temperatures, is approximately 20%. In addition, certain semiconductor detectors, such as the VUV-MPPC, are sensitive to vacuum ultraviolet light by eliminating the protective window material in front of the semiconductor detection area. It has been confirmed that they can operate in liquid argon environments. For example, the Photon Detection Efficiency (PDE) of the latest 4th-generation VUV-MPPC is about 10–20% for liquid argon scintillation [64, 65].

On the other hand, visible light can be detected by photon-detection devices that operate at liquid argon temperatures, exhibiting a sensitivity to visible light in excess of 30%. In addition, visible light is more effectively collected than VUV because of its ease of reflection compared to VUV, resulting in detectors with high light collection efficiency. Therefore, many liquid argon experiments use a method of wavelength downshifting from liquid argon scintillation to visible light before detection. Wavelength shifting is the subject of this dissertation, described in detail in Chapters 4.

The observed light yield of a liquid argon detector with wavelength shifting, caused by the energy deposition originating from electron recoil, nuclear recoil, and α-ray, as illustrated in Fig. 3.6, can be

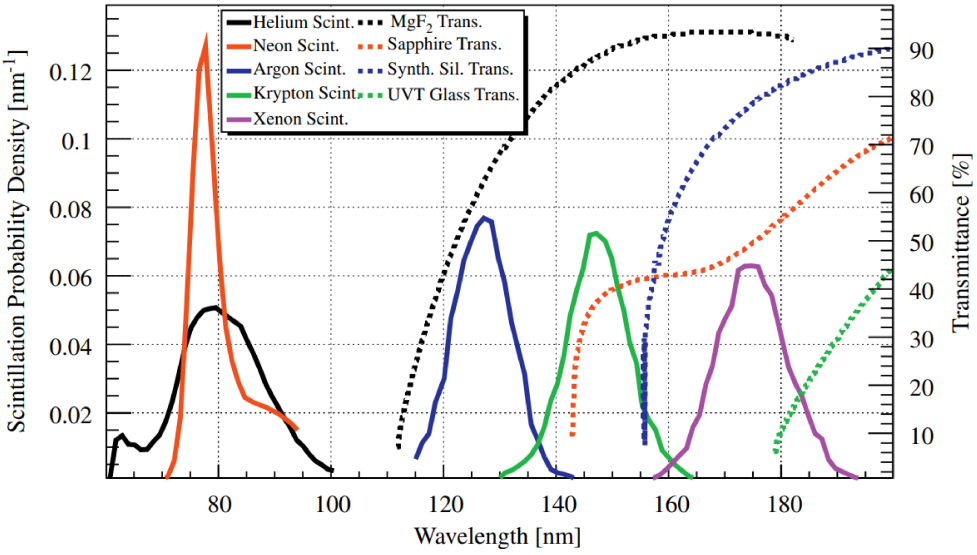

Fig. 3.5. Scintillation spectra for liquefied noble gases and transmittance of common PMT window materials. The figure is taken from Ref.[66].

described as:

$$LY_{obs} = LY_{LAr} \times A_{vuv} \times \varepsilon_{WLS} \times A_{vis} \times QE_{pmt}, \tag{3.1}$$

where LY_{LAr} is the scintillation yield of liquid argon, A_{vuv} is the geometrical acceptance of the VUV scintillation light reaching the wavelength shifter, ε_{WLS} represents the wavelength shifting efficiency defined as the probability of visible light emission when VUV light is incident on the wavelength shifter, A_{vis} is the geometrical acceptance of downshifted visible light reaching the photo-devices, and QE_{pmt} is the QE of PMTs. For example, assuming maximum geometrical acceptance ($A_{vuv} \times A_{vis} = 1$), conversion without excess or deficiency ($\varepsilon_{WLS} = 1$) and a PMT with a QE_{pmt} of 30%, the observed light yield for the recoil electron event ($LY_{LAr} = 41$ photons/keVee) is expected to be $LY_{obs} = 41 \times 1 \times 30\% = 12.3$ p.e./keVee.

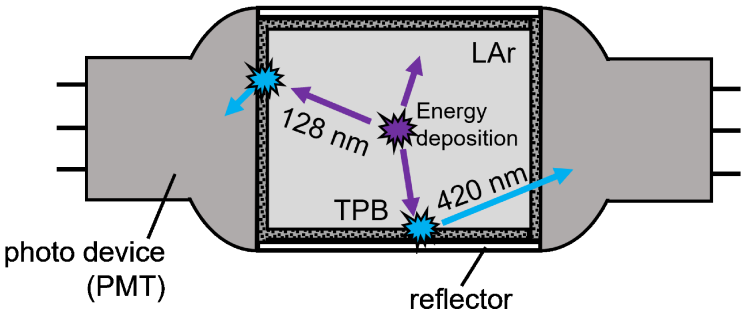

Fig. 3.6. Schematic of the detection of liquid argon scintillation.

3.3.2 Detection of ionized electrons as charge signal

The signal electric current at the electrodes is induced as free electrons drift between the electrodes. Many detectors incorporate a grid or wire-shaped electrode, referred to as the gate-grid hereafter, positioned in front of the anode electrodes, in addition to the cathode and anode electrodes as illustrated in Fig. 3.7. In this configuration, the signal electric current is induced on the anode electrode while drifting between the gate-grid and anode, rather than between the cathode and gate-grid. The total induced charge is equivalent to the number of charges that have moved between the anode and gate-grid.

Generally, the signal is amplified by a charge-integrating amplifier connected to the electrodes. It is essential to utilize a low-noise readout device capable of detecting small charge signals. Anode electrodes can take the form of a 2D wire or strip electrode or a 3D pad, and the XY position can be reconstructed from the hit anode channel. The position resolution is contingent on the electrode size, and, in principle, good resolution can be achieved down to the diffusion level of drift electrons. Some detectors utilize a 3-axis wire configuration because the 2-dimensional readout lead to misreconstruction, resulting in ghost tracks. The Z position is reconstructed from the time difference between the scintillation and ionized electron signals. In the case of the gas-liquid two-phase TPC, a method of generating electron amplification in the gas phase is also under development.

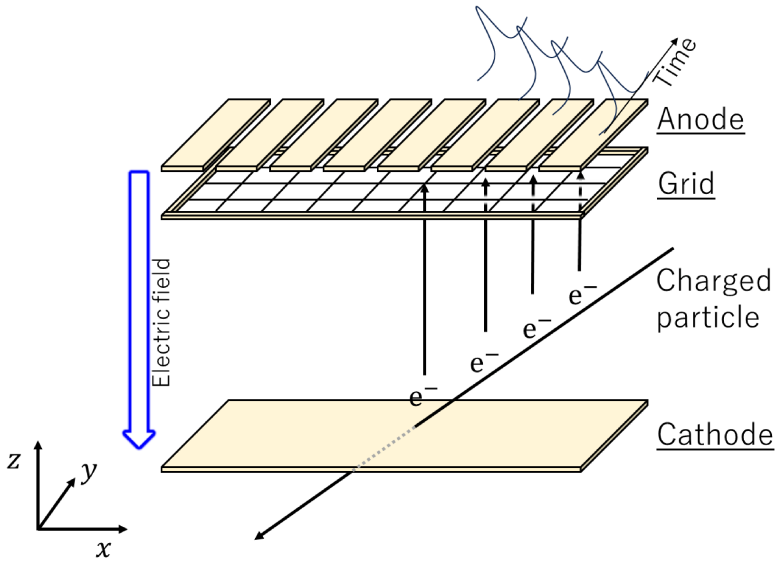

Fig. 3.7. Schematic of the detection of drift electron.

3.3.3 Detection of ionized electron as electroluminescence

When there is an electric field above a certain level at the liquid surface of argon, electrons are extracted from the liquid phase to the gas phase. As shown in Fig. 3.8, the larger the applied electric field, the

greater the probability of transfer from the liquid phase to the gas phase. Because the density of the gas phase is smaller than that of the liquid phase, electrons extracted into the gas phase are accelerated more easily than those in the liquid phase.

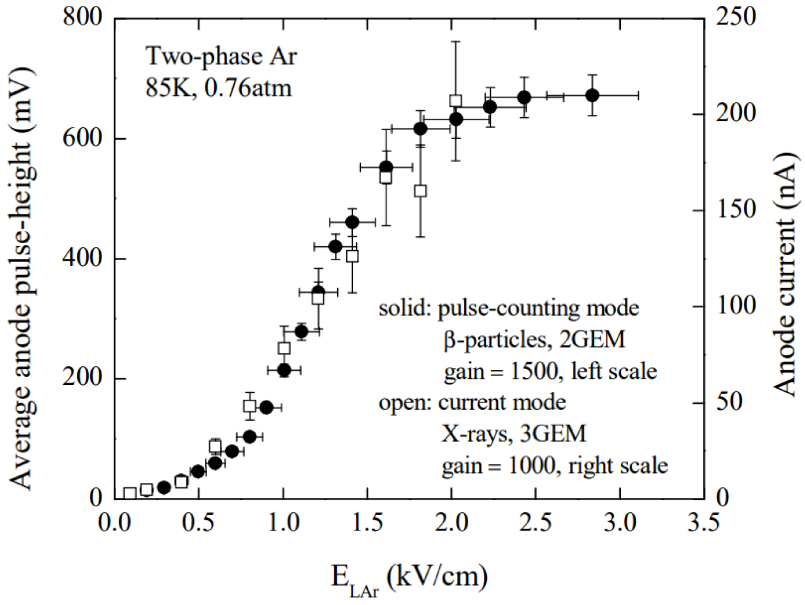

Fig. 3.8. Extraction efficiency of electrons from the liquid to gaseous phase, measured as a function of the extraction electric field. The figure is taken from Ref.[51].

The free electrons moving through gaseous argon undergo repeated collisions with argon atoms, exciting and ionizing the surrounding argon along their trajectories when a certain level of electric field is applied to gaseous argon. This process generates gaseous argon scintillation, known as electroluminescence. As explained earlier, this emission includes components of vacuum ultraviolet, ultraviolet, and infrared light. The electroluminescence yield N_{el} depends on factors such as the density of gaseous argon ρ, electric field F, and the drift length in gas x. The relationship is expressed as follows:

$$\frac{1}{\rho}\frac{dN_{\mathrm{el}}}{dx}[10^{-17}\mathrm{photon/electron}\cdot\mathrm{cm}^2/\mathrm{atom}] = P_\alpha\frac{F}{\rho} - P_\beta, \tag{3.2}$$

where F/ρ is in Td (10^{-17} V cm^2 atom^{-1}), and P_α and P_β are constant parameters. Measurements from Ref.[67] provide $P_\alpha = 0.081$ and $P_\beta = 0.190$. The electroluminescence yield, with a luminescence field of a few kV/cm and an inner pressure of $O(1$ atm), is on the order of $O(10$–$100)$ photon/electron/cm.

3.4 Challenges to enhance performance of liquid argon detector

Figure 3.9 illustrates challenges for development of liquid argon detector. For all types of detectors described in Section 3.1, low-temperature techniques and the attainment of high purity argon are necessary.

In addition, the detector configuration varies depending on the physics motivation, leading to differences in the development elements.

In direct dark matter search experiments, the region of interest for the recoil energy of dark matter with argon is 100 keV or below. A lower energy threshold is advantageous for observations. Especially, when searching for dark matter with masses on the order of a few GeV or lower, it is necessary to detect recoil energies below 1 keV. Therefore, Darkside-50, targeting liquid argon, utilizes a Double-Phase Time Projection Chamber (DP-TPC), while DEAP-3600 uses a Single-Phase Scintillation Detector (SP-Sci). Both detectors are designed to detect low-energy events. For the detection of low-energy rare events, both DP-TPC and SP-Sci require a medium-sized detector with a liquid argon of about several tens of tons, high light collection efficiency, and the use of extremely low-background detector materials. In the case of DP-TPC, it is crucial to achieve sufficient gain for S2 electroluminescence and understand its emission.

In neutrino experiments, the total energy deposited in the detector varies widely, ranging from a few MeV to 100 GeV, depending on the origin of the neutrinos being studied. However, particles depositing energy to argon is charged particles like electrons or muons from neutrinos interacting in the detector. For instance, in the case of Minimum Ionizing Particles (MIPs), around 1×10^5 quanta are generated per centimeter, resulting in a significantly larger signal yield compared to dark matter searches. However, since the reconstruction of charged particle tracks is necessary, a high spacial resolution is required. Additionally, to detect neutrinos with low interaction probabilities at high statistics, the construction of a large-scale detector on the order of tens of kilotons becomes necessary. With the scale-up, challenges arise, including the increase in the required number of readout channels and the applied voltage for electric field. Notably, the MicroBooNE experiment has already conducted observations using a SP-TPC, and the DUNE experiment is advancing the development of both DP-TPC and SP-TPC.

On the contrary, liquid argon detectors have not been utilized to observe cosmic MeV gamma rays, which are attractive in astrophysics, or for the observation of charged cosmic antiparticles, which are good probes for dark matter. For these observations, it is necessary to operate the detector at an altitude of over 30 km to avoid atmospheric shielding, and it is required to be mounted on a flying object such as a scientific balloon or a satellite. However, there have been no missions with liquid argon detectors on balloons or satellites. Balloon and satellite experiments have unique challenges, such as shocks during launch and parachuting, as well as changes in atmospheric pressure and temperature during ascent. In the case of detecting cosmic charged antiparticle, similar to neutrino experiments, charged particles move through liquid argon, resulting in a large deposited energy that can be reconstructed by existing SP-TPC technology. On the other hand, for cosmic gamma rays in the MeV range, where Compton scattering is the main reaction, recoils of several tens to several hundred keV occur at each interaction point. To reconstruct these event as a Compton camera using a single-phase detector for incident direction and energy, it is essential to achieve an energy resolution close to the theoretical limit and a position resolution of a few millimeters. Since there is no liquid argon detector that satisfies these requirements, the development of a high-energy and high spatial resolution readout for ionized electrons is necessary, as well as on-board flight objects.

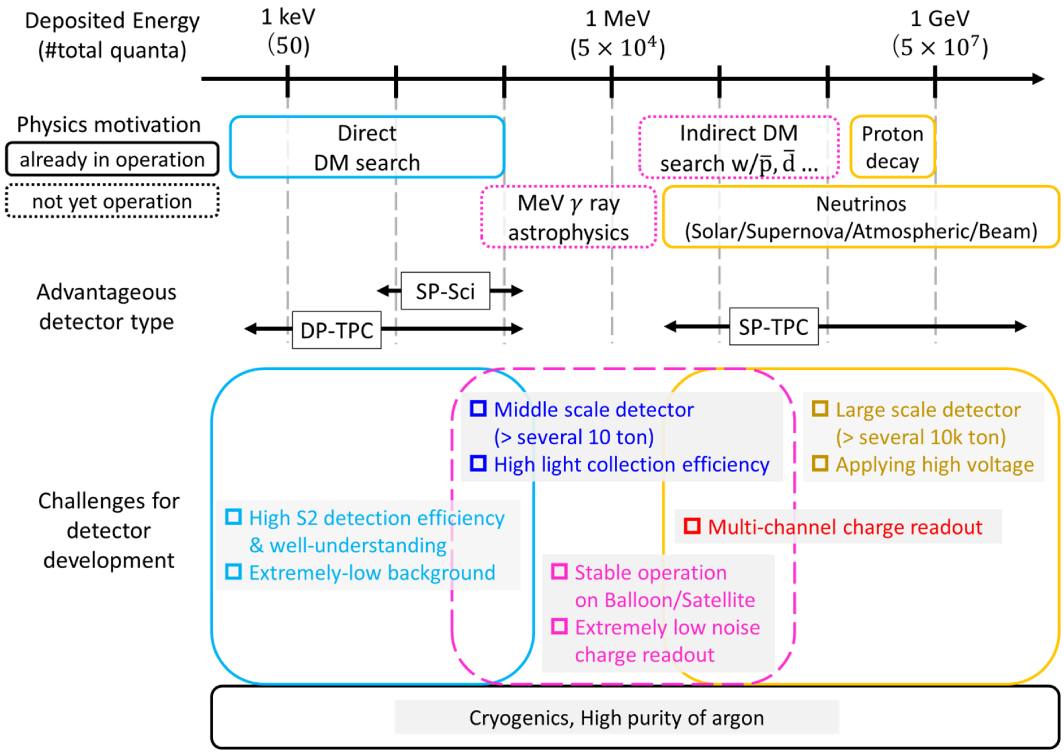

Fig. 3.9. Schematic illustrating challenges for development of liquid argon detector.

3.5 Subject of this dissertation

As described above, the liquid argon detector exhibits ease of scaling up, excellent energy/position reconstruction capability, and strong particle identification. These qualities satisfy the requirements for a detector listed in section 1.2. On the other hand, there are numerous challenges in maximizing these capabilities.

In liquid argon detector, the detection of light signals is an essential technique. There are two types of light signals emitted in the liquid and gas phases as mentioned above, and all of liquid argon detector utilize light signals. In direct dark matter search experiments, the understanding and efficient detection of luminescence exhibit a significant impact on performance in terms of energy resolution and particle discrimination capability. Vacuum ultraviolet light is the primary emission element for both liquid- and gas-phase luminescence, making its detection technique crucial in any liquid argon detector. While the luminescence associated with the excitation and de-excitation of argon is well-understood, as previously explained, the luminescence in the visible light region in the gas phase remains less clear. This lack of understanding may introduce uncertainty or result in the overlooking of useful luminescence signals. Efficient detection of vacuum ultraviolet light and an understanding of gas-phase luminescence are pivotal developments in enhancing the sensitivity of liquid argon detectors in direct search experiments.

The light detection technique is not only crucial for direct searches but is also valuable for neutrino experiments and indirect searches. However, when applied to indirect search experiments requiring mounting

on a flying vehicle, challenges arise that are not required in ground-based experiments. Therefore, for the knowledge on light detection obtained in this study to be applied to future indirect search experiments, it is imperative to overcome the challenges specific to such flying objects.

Thus, this dissertation focuses on addressing the following three challenges related to the liquid argon detectors.

Maximization of light collection efficiency

As discussed thus far, enhancing photon collection efficiency proves beneficial for achieving lower energy thresholds and improved particle identification. Previous studies utilized detectors with light detection efficiencies below 10 p.e./keVee, as shown in the table. The liquid argon detector used by Waseda's experimental group also had a light collection efficiency of less than 10 p.e./keVee before the study of this dissertation.

Table 3.2. Light collection efficiency of liquid argon detectors

Experiments	E-Field (V/cm)	Light collection efficiency (p.e./keVee)	Reference
DarkSide-10	Zero	9.1	[68]
DarkSide-50	Zero	7.9	[69]
	200	7.0	
DEAP-3600	Zero	7.8	[70]
SCENE	Zero	6.3	[71]

A light collection efficiency of about 12 p.e./keVee can be achieved with the approximately 30% quantum efficiency of the PMT for visible light, a common choice in many experiments. In addition, light collection efficiency can be further improved by changing the light detection device to one with higher sensitivity. In this study, our focus was on improving light collection efficiency through the following two methods:

1. Optimization of TPB wavelength shifting

To enhance the light collection efficiency until it is constrained by the detection efficiency of the light detection device, the factors $A_{vuv} \times \varepsilon_{WLS} \times A_{vis}$ in the formula 3.1 are optimized. To achieve this, we developed a vacuum evaporation system that allows for precise control of the coating. We then optimized the coating of the wavelength shifter.

2. Installation of TSV–MPPC to liquid argon detector

The TSV-MPPC, with high sensitivity to visible light after wavelength conversion, was implemented into the liquid argon detector. Compared to the 30% sensitivity of the PMT, the TSV-MPPC has a sensitivity exceeding 50%. In principle, this implies an expected light collection efficiency of exceeding 41 photon/keVee $\times$ 50% = 20.5 p.e./keVee.

Spectrum measurement of NBrS emission

The NBrS described in Section 2.4.2 is still poorly understood, as its emission and wavelength characteristics have not been experimentally confirmed. Scrutinizing this emission process is crucial for a better understanding of the existing S2 signal detection. Furthermore, given the expected wavelength in the visible light range, optical detection may be feasible without requiring wavelength conversion if enough light is available. The electric field required to generate NBrS is also lower than that required for normal electroluminescence, which is advantageous both for operation and for scaling up. If it can be confirmed that NBrS is generated with sufficient light yield even in liquid phase, it may be possible to convert the ionizing electron signal into an optical signal in single-phase TPCs. This could enable eliminating the need for a charge readout device with exceptionally high signal-to-noise ratio when directly reading ionizing electrons in single-phase TPCs. This capability is valuable for detecting low-energy events, particularly in environments where two-phase operation is not feasible, such as on balloons. In this study, we measured the emission wavelength spectrum in gaseous argon while systematically varying the electric field and the concentration of nitrogen impurities to advance our understanding of NBrS.

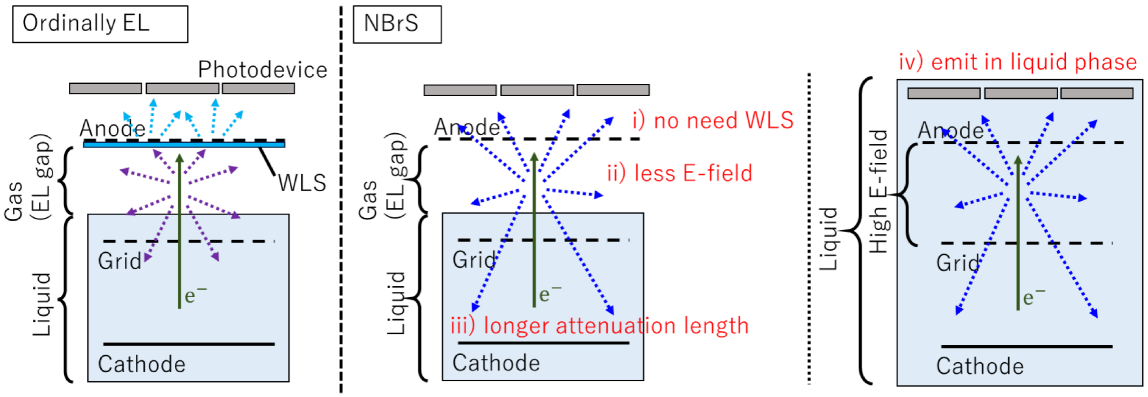

Fig. 3.10. Advantageous in NBrS compared to ordinary luminescence.

Application to scientific balloon-borne experiments

While liquid argon detectors have been extensively utilized in ground and underground experiments, they have not yet been operated on flying objects such as balloons and satellites. Liquid argon, however, can be configured to cover large solid angles and large sensitive areas, presenting the potential for significant advancements in cosmic ray observations including indirect dark matter search. This study conducted a balloon-borne experiment as the initial test for airborne operation of liquid argon. Details are described in Section 7.

3.6 Liquid argon test stand at Waseda University

The liquid argon test stand, utilized in liquid argon test described in Chapters 4 and 5, is situated in a semi-underground location on the Nishiwaseda campus in Okubo, Shinjuku-ku, Japan. The test stand comprises liquid argon, a detector within a 200L vacuum-insulated vessel, filling and circulation lines, a liquefier, an electric rack, and a desk for monitoring. An overall photograph of the setup is presented in Figure 3.11.

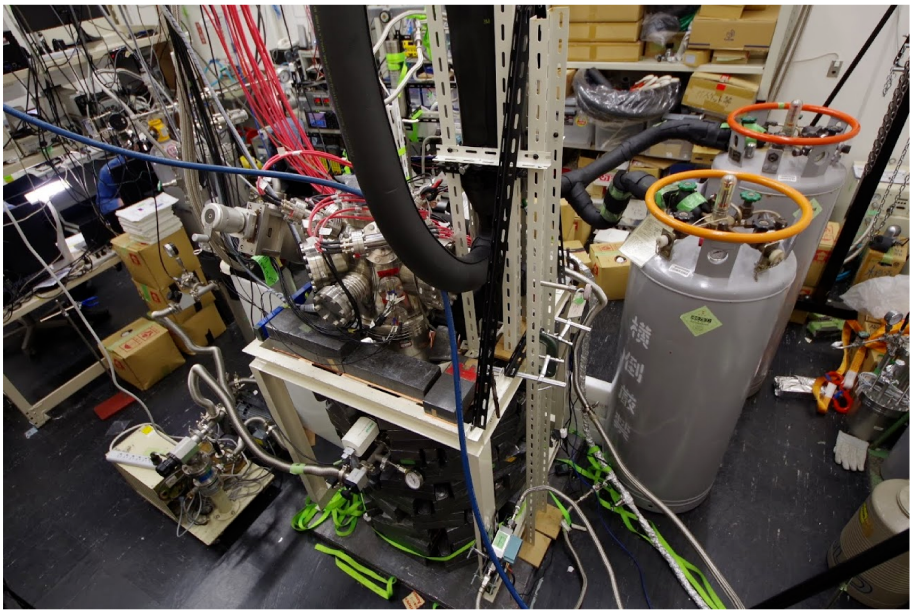

Fig. 3.11. Liquid argon test stand of Waseda university.

Figure 3.12 illustrates the schematic of liquid argon handling system situated on Waseda university. Liquid argon for the detector is contained in a vacuum-insulated stainless steel vessel with a diameter of 50 cm, a height of 100 cm, and a capacity of 200 L. The liquefier, equipped with a 200 W GM-cryocooler (Sumitomo CH-100), is also constructed from a stainless steel vacuum-insulated container. The GM-cryocooler cools the gaseous argon, circulating it through the system before returning it to the 200L container to cool its interior. It's important to note that the 200L vessel and the argon in the liquefier are separated.

At Waseda's test stand, impurities are systematically reduced in three steps. Initially, to minimize outgassing, the 200L vessel and circulation system are evacuated for 10 days to 2 weeks before the experiment, achieving a vacuum level of 1×10^{-3} Pa. As the liquid argon used for system filling is commercially obtained and contains impurities, a homemade filter, comprising molecular sieve and reduced copper, is employed during the filling process to eliminate water and oxygen. Moreover, the argon gas circulation line is equipped with a SAES Microtor to remove water and oxygen, along with a Pureron GP-5 to eliminate nitrogen. The argon gas flows through the circulation line at a rate of approximately 30

L/min. These vacuuming and filtering procedures effectively reduce electronegativity impurities (oxygen and water) to sub-ppb levels and nitrogen impurities to sub-ppm levels.

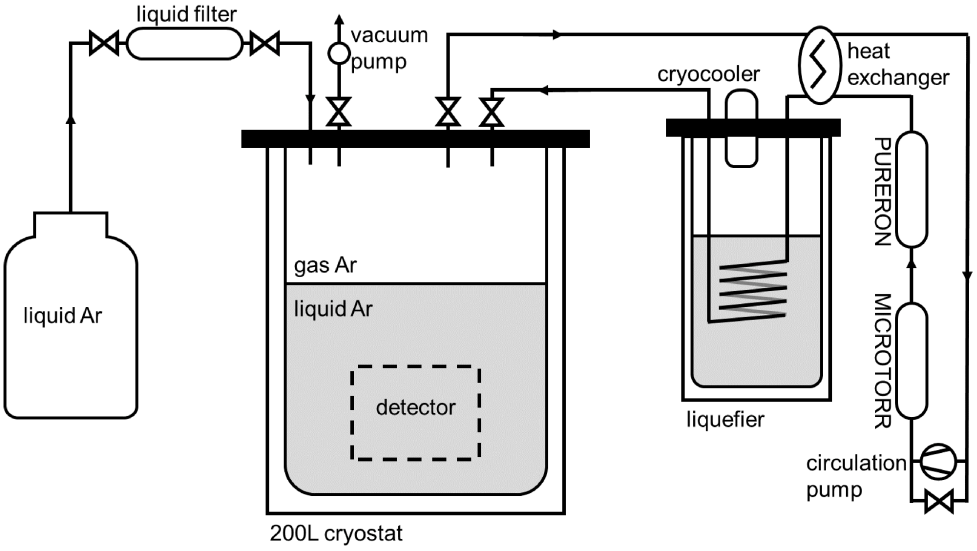

Fig. 3.12. Schematic of liquid argon handling system situated on Waseda university.

CHAPTER 4

Optimization of TPB wavelength shifting

In Chapter 3, we discussed the significance of wavelength downshifting as a technique in liquid argon scintillation light detection. This chapter begins with a brief overview of organic wavelength-shifting materials commonly utilized in liquid argon detectors. Following that, we detail the wavelength shifter deposition system and the thin film evaluations performed in this study. Finally, we describe the measurements of the light detection efficiency of the liquid argon detector.

4.1 Wavelength shifter

4.1.1 Requirements

For the wavelength shifter used in liquid argon detector, the following four characteristics are required:

- high absorption rate for liquid argon scintillation peaked at 128 nm,
- high luminescence yield per absorbed photon,
- low overlap between absorption and luminescence spectra, resulting in a high transmittance of emitted photons,
- long term stability in liquid argon.

Additionally, to achieve PSD capability, it is necessary to use a wavelength shifter that emits photons promptly compared to liquid argon scintillation. Furthermore, in rare event searches, the contamination of radioisotopes must be low.

4.1.2 Conversion mechanism

The description in this section is informed by Ref.[72]. Figure 4.1 illustrates the wavelength shifting process, including absorption, vibrational relaxation (VR), internal conversion (IC), intersystem crossing (ISC), fluorescence, and phosphorescence. The thick horizontal lines denote electronic levels, while the thin horizontal lines represent vibrational levels associated with each electronic state. Straight arrows indicate absorption and emission, respectively, and wavy arrows symbolize processes without radiation, such as vibrational relaxation. Table 4.1 summarizes the typical timescale for each process.

At temperatures below room temperature, the majority of molecules exist in the ground state (S_0) with zero vibrational energy. Light absorption induces transitions from S_0 to an excited singlet state (S_1 or

S_2) or their corresponding vibrational levels. Fluorescence occurs when the transition is from S_1 to S_0 or the vibrational level corresponding to S_0, emitting photons. Internal conversion leads to the direct transition from S_1 to the vibrational level of S_0 without photon emission. Intersystem crossing from a singlet state to a triplet state (T_1) involves initial vibrational relaxation, followed by a transition from T_1 to either the ground state (S_0) or its vibrational level, resulting in phosphorescence. The extended lifetime of phosphorescence, compared to fluorescence, is due to the forbidden transition from the triplet state to the singlet state. Additionally, the triplet state can undergo intersystem crossing back to S_0 without photon emission.

The longer wavelength of fluorescence compared to the absorption wavelength is attributed to energy consumption during vibrational relaxation. Additionally, the wavelength of phosphorescence surpasses that of fluorescence due to this energy-consuming process. The broad spectrum observed in both absorption and emission results from excitation and relaxation processes involving vibrational levels.

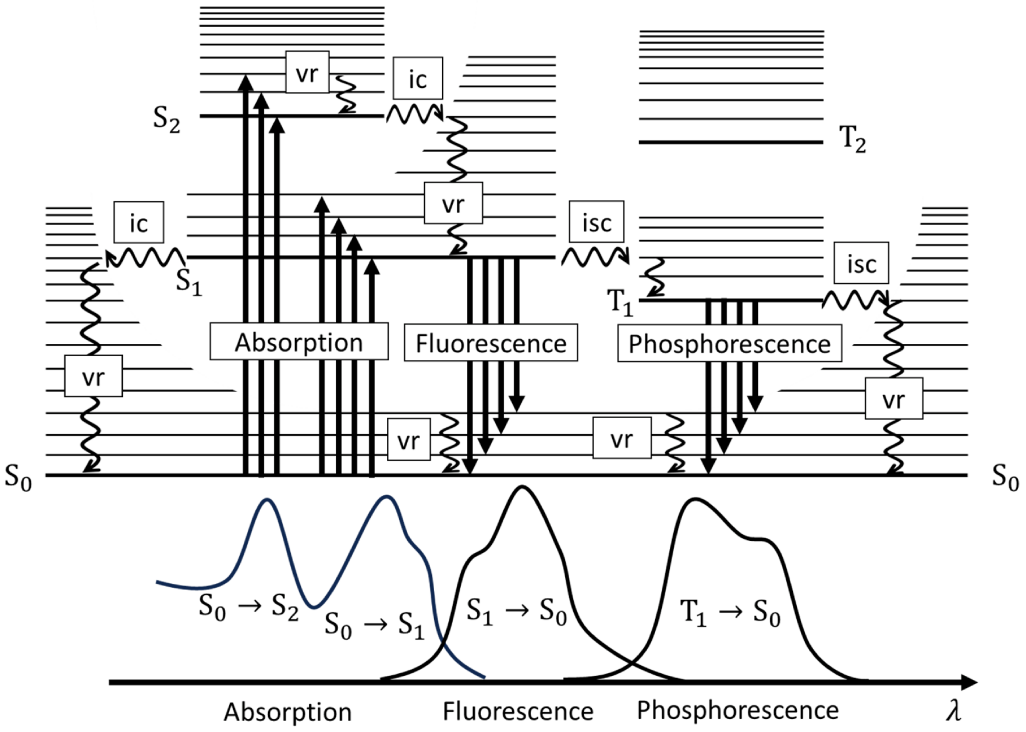

Fig. 4.1. Jablonski diagram illustrating the wavelength shifting process, including absorption, fluorescence, phosphorescence, and relevant transitions. The thick lines represent electronic levels, while the thin lines denote vibrational levels. The figure is illustrated based on information from Ref.[72].

4.1.3 Wavelength shifters in liquid argon

Several wavelength shifters meet the requirements outlined in section 4.1.1. Table 4.2 summarizes features of some wavelength shifters considered for applications in liquid argon detectors, with their emission

Process	Timescale
Vibrational relaxation	$10^{-12} - 10^{-10}$ s
Internal conversion	$10^{-11} - 10^{-19}$ s
Intersystem crossing	$10^{-10} - 10^{-8}$ s
Lifetime of S_1 (Fluorescence)	$10^{-10} - 10^{-7}$ s
Lifetime of T_1 (Phosphorescence)	$10^{-6} - 10$ s

Table 4.1. The timescale of processes within the conversion mechanism [72]

wavelengths shown in Fig. 4.2 [73]. It's essential to note that measuring the absolute luminescence yield of wavelength shifters involves significant uncertainty due to challenges in estimating light propagation and reabsorption, as well as aging and forming method dependence.

1,1,4,4-tetraphenyl-1,3-butadiene (referred to as TPB hereafter) has been widely used in liquid argon detectors due to its short emission time constant, ease of thin film formation, robustness, and emission wavelength matching typical PMT sensitivity. Thin films of TPB can be produced using both the polymer matrix and vacuum evaporation methods. Our experimental group, after investigating both coating production methods, found that the vacuum evaporation method provides higher light collection efficiency. Consequently, we employ the vacuum evaporation method.

Wavelength Shifter	λ_{peak} [nm]	yield @128 nm	τ [ns]	T_m [^oC]
TPB	430	0.6-2 [74, 75]	2	204
p-Terphenyl	350	0.82 (@254 nm) [76]	1	213
bis-MSB	440	0.42 [77]	1.5	180
pyrene	470	0.64 (@260 nm) [78]	155	150
PEN	420	0.4-0.8 [79] (relative to TPB)	20	270

Table 4.2. Characteristic of wavelength shifter considered for liquid argon detector [73]

4.2 1,1,4,4-tetraphenyl-1,3-butadiene (TPB)

TPB is a white powdery substance (Figure 4.3) with properties summarized in Table 4.3. The melting point of TPB is approximately 210 °C at atmospheric pressure, and its boiling point is around 556 °C. Excessive heating induces a transformation into a non-wavelength-shifting yellow substance, necessitating caution [80]. When exposed to ultraviolet light in an oxygen environment, TPB undergoes a transformation into a substance known as benzophenone, which does not emit photons. It is stored at a temperature between 2 and 8 °C for preservation.

Figure 4.4 illustrates the emission and absorption spectra of TPB. TPB absorbs photons with wavelengths below 400 nm and emits with a peak at around 420 nm. The emission spectrum maintains a consistent shape within the wavelength range of 265 to 400 nm for absorbed photons.

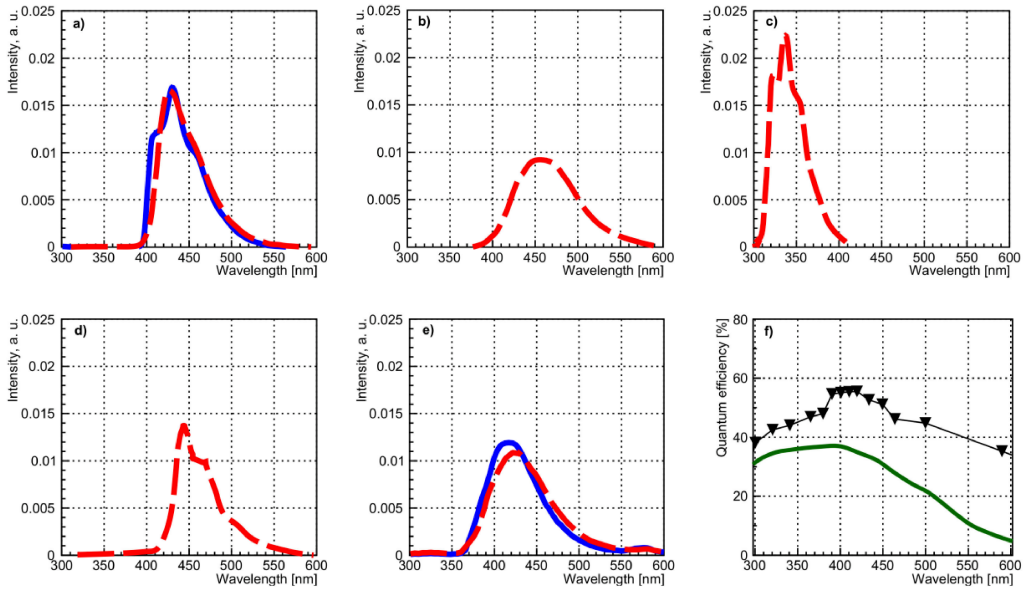

Fig. 4.2. The emission wavelength spectrum of several wavelength shifter measured in room temperature (red) and cryogenic temperature (blue). Each panel represents (a) TPB, (b) pyrene, (c) p-terphenyl, (d) bis-MSB, and (e) PEN. Panel (f) displays the quantum efficiency for Hamamatsu R11065 PMTs (green) and FBK NUV-HD-SF SiPMs at an overvoltage of 10 V (black), respectively. This figure is taken from Ref.[73].

Table 4.3. TPB basic properties.

molecular formula	$C_{28}H_{22}$
molecular weight	358.48
density	1.079 g/cm^3
boiling point(1 atm)	556.1°C
melting point(1 atm)	207 ~ 209°C
ignition point	289°C
storage temperature	2 ~ 8°C
refractive index	1.635

Fig. 4.3. Image of TPB.

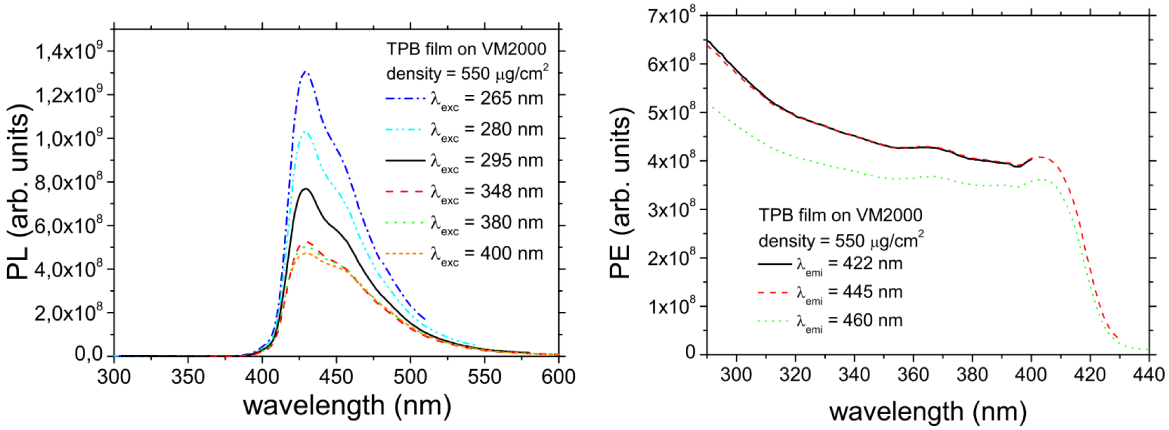

Fig. 4.4. Emission (left) and absorption (right) spectra of TPB. The figure is taken from Ref.[81].

As shown in left panel of Fig. 4.5, a second peak is observed around 400 nm in the cryogenic environment at liquid argon temperature (87 K), attributed to the vibrational level of the molecule. However, the primary peak at around 420 nm remains consistent. Consequently, TPB maintains its emission wavelength within the visible light range, even at cryogenic temperatures. Additionally, as shown in the right panel of Fig. 4.5, the photon yield of TPB is higher at lower temperatures. This is due to the more effective relaxation process at higher temperatures, including intramolecular vibration and rotation without photon emission.

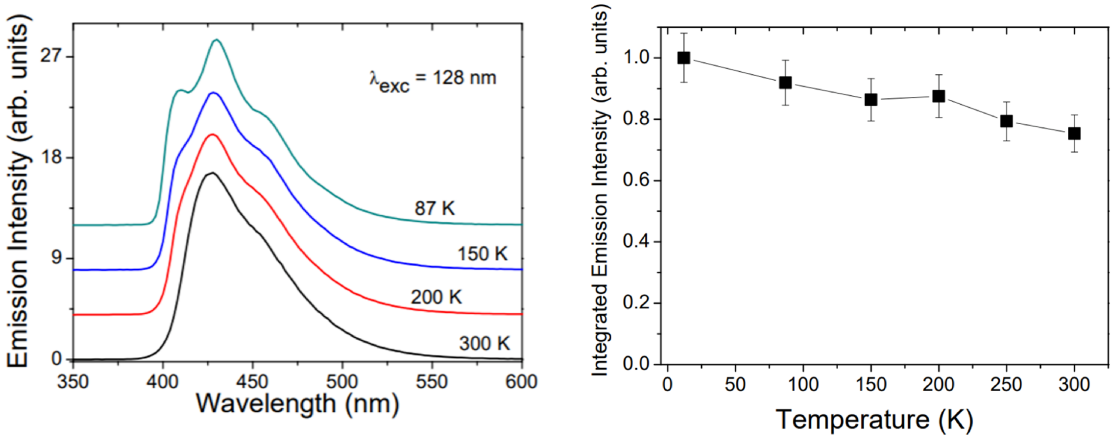

Fig. 4.5. The temperature dependence of the emission spectrum (left) and integrated relative photon yield (right) of TPB. Figure 4.5 is taken from Ref.[81].

The absolute wavelength shifting efficiency of TPB has been measured in various experiments, nevertheless this value remains controversial. Figure 4.6 illustrates the absolute photon yield of TPB for one-photon incident. In the left figure, results are based on a sample prepared by vacuum deposition. The red and black lines in this figure represent outcomes from the same dataset. The red line reflects an

updated calibration, specifically addressing photon propagation. Moving to the right figure, it includes two sets of samples: one prepared by vacuum deposition (red dots) and another by spin coating (black dots). Additionally, hollow dots in the right figure represent samples that were exposed to the atmosphere for 100 days. Both measurements were conducted at room temperature, utilizing a plasma lamp as a light source in the left figure and a synchrotron radiation facility as a light source in the right figure. The absolute photon yield of TPB ranges from approximately 0.6 to 2, depending on the measurement. These variations result from challenges in assessing the effects of aging and photon propagation processes, including reflection and reabsorption within TPB itself.

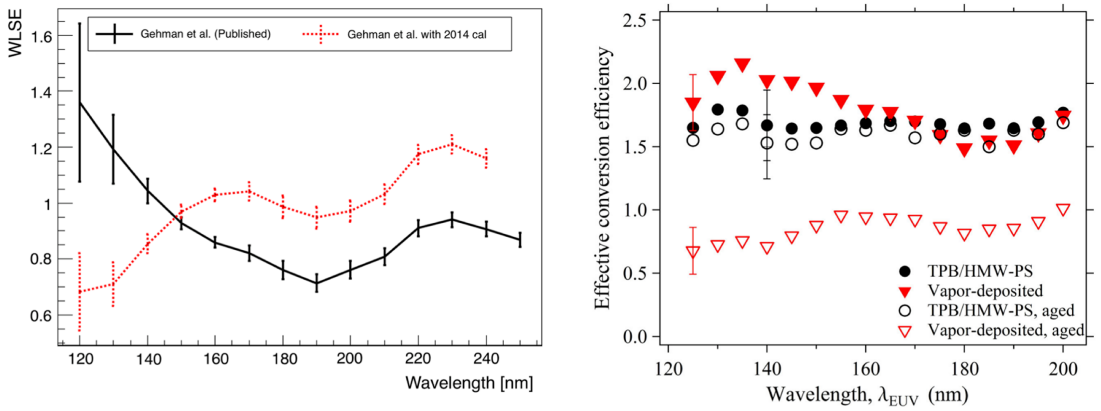

Fig. 4.6. The measured absolute photon yield of TPB. The left and right figures are taken from Ref.[74] and Ref.[75], respectively.

4.3 Vacuum evaporation system

TPB is deposited onto the detector using the vacuum evaporation method, a thin film formation technique. In this process, the evaporation material undergoes sublimated in a vacuumed container and is then adhered to the surface of a substrate positioned at a certain distance from the crucible. Sublimation methods vary based on the evaporation material, including techniques like resistance heating, laser, and electron beam. The use of a vacuum is essential to prevent sublimated substances from scattering with gas molecules before reaching the deposition surface. The exhaust system is typically configured to achieve a vacuum of $10^{-4} \sim 10^{-3}$ Pa. Additionally, increased distance between the crucible and the deposition surface enhances the uniformity of deposition. Since vacuum evaporation involves heating the evaporation material, threfore, only materials with stable properties under heat can be effectively evaporated. TPB begins to sublimate at around 180°C in a vacuum, but at higher temperatures, it transforms into a substance that does not emit photons. Hence, precise temperature control is necessary to ensure proper deposition.

To achieve stable TPB coating, we constructed a vacuum evaporation apparatus, as shown in Fig. 4.7. This apparatus comprises a stainless steel vacuum chamber, an evacuate system, a crucible, a jig for holding the evaporated substrate, a DC voltage source, and various monitoring systems. The vacuum

chamber has a diameter of 420 mm and a height of 400 mm, equipped with two view ports allowing observation of the deposition process. A scroll pump and a turbo pump, directly attached to the stainless steel vessel, are utilized for evacuation. After approximately 15 hours of evacuation, achieving a vacuum of up to 5×10^{-4} Pa. The inner vessel pressure is measured using a Bourdon tube and a Pirani cold cathode vacuum gauge, with the readings automatically recorded in a PC.

Fig. 4.7. Image of the TPB evaporation system. The pressure in the vacuum vessel is lower than 1×10^{-3} Pa.

The amount of TPB deposited affects the wavelength shifting efficiency and visible light transmittance of TPB thin coatings, necessitating careful evaluation and ensuring reproducibility. To measure the deposition amount, we utilize a quartz crystal microbalance (QCM), capable of measuring masses ranging from several nanograms to several hundred micrograms. The QCM sensor consists of a thinly processed quartz crystal plate sandwiched between two metal electrodes, as shown in Figure 4.8. Upon applying an alternating electric field to the electrodes, the crystal oscillates at a specific resonance frequency. As a substance adheres to the electrode surface, the frequency decreases proportionally to its mass, allowing determination of the adhered mass by measuring the frequency change. It is important to note that if the substance being measured does not adhere to the electrode, such as when feathers are present on the electrode surface, the mass cannot be accurately measured with a standard QCM. Table 4.4 summarizes information on the QCM sensors used.

To initiate the evaporation procedure, the vessel was evacuated until its inner pressure reached approximately 1×10^{-3} Pa. Subsequently, the heater voltage was set to 35 V for the first 15 minutes, followed by 30 V, to prevent TPB degeneration. The TPB was heated until complete evaporation from the crucible. Fig. 4.9 shows the temporal parameter changes in parameters recorded during the TPB heating. These parameter behaviors were reproducible at the same heater voltage control, confirming the reproducibility of the TPB coating on this evaporation system. The evaporation result was further validated by measuring the deposition mass of TPB using the QCM sensor.

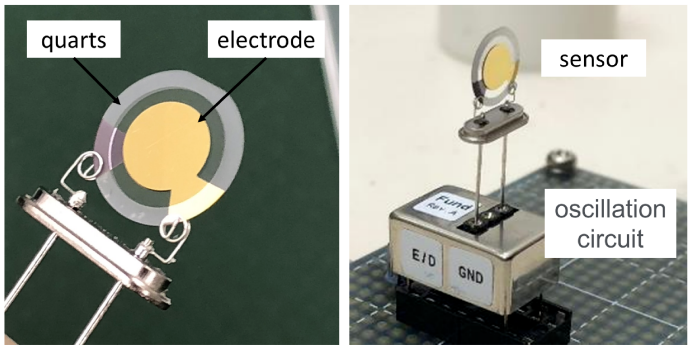

Fig. 4.8. Image of QCM sensors to measure the deposition mass of the TPB at the height of the deposition surface.

Table 4.4. Information of the QCM sensor used in this study

manufacturer	TAMADEVICE Co.,Ltd
model number	QSET-5P-H
fundamental frequency	5 MHz
electrodes size	ϕ5 mm
sensitivity	3.47 ng/Hz
dynamic range	300 ng ~ 100 µg

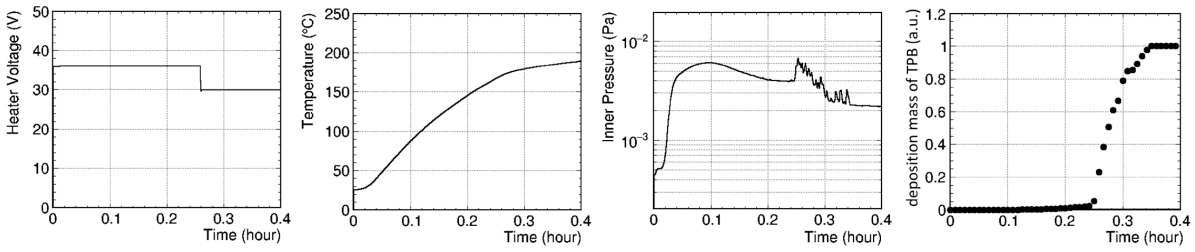

Fig. 4.9. The environmental parameters when heating the TPB were as follows: heater voltage (left), crucible temperature (left center), inner pressure (right center), and TPB deposition mass (right).The horizontal axis indicates the elapsed time since the heater voltage was switched on.

Left panel of Fig. 4.10 correlates the TPB amount in the crucible with the evaporated mass measured by the QCM sensor positioned 7 cm away from the center of the evaporation surface. Sublimated TPB moves straight in a vacuum, depositing on a surface without colliding with gas molecules. Hence, the evaporated mass can be estimated by assuming an even distribution over the hemisphere from its respective position in the crucible. The red dashed line in left panel of Fig. 4.10 represents the TPB deposition mass estimated from the geometry. The actual deposition mass is consistent with the expected evaporation mass. Furthermore, as depicted in right panel of Fig. 4.10, the deposition mass exhibits uniformity, showing variations of less than 10% within a 7-cm radius from the central axis of the system.

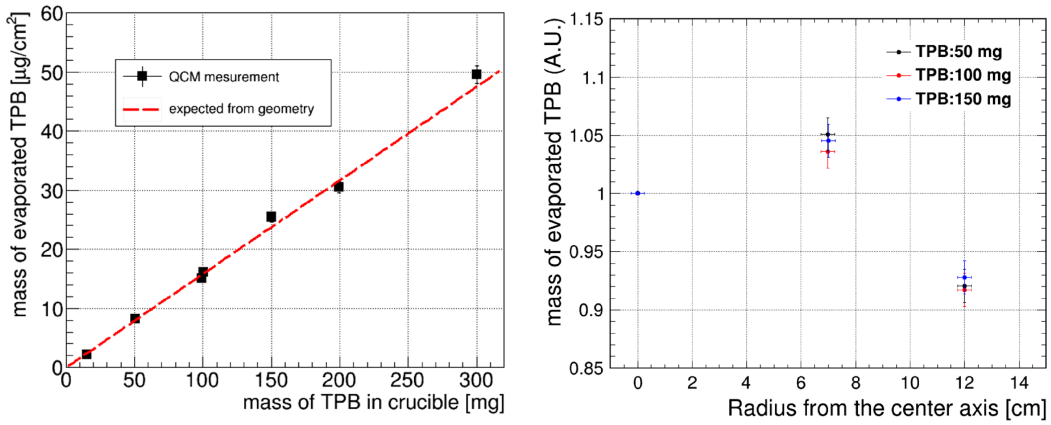

Fig. 4.10. (Left) The correlation between the amount of TPB in the crucible and the deposition mass.The deposition mass was measured using the QCM sensor. The black squares represent the deposition masses measured by the sensor, while the red dashed line represents the values expected from the geometry of the evaporation system. These measurements and expectation were specifically conducted at a distance of 7 cm away from the center of the evaporation surface. (Right) Uniformity of TPB coating in this evaporation system, with mass of TPB in the crucible of 50 mg (black plots), 100 mg (red plots), and 150 mg (blue plots), respectively. Plots were normalized to data obtained at r=0, per evaporation with different amounts of TPB.

4.3.1 Surface condition of TPB

Figure 4.11, taken utilizing a polarizing microscope, illustrates the surface conditions of evaporated TPB on acrylic disks with varying deposition masses. The coating, with an estimated density of 2 μg/cm^2, displayed evenly distributed kernels exhibiting relatively high luminance (strong polarization). As the deposition mass increased, a crystalline structure developed. The deposition thickness of the TPB was measured using a stylus profilometer (Dektac 6M, ULVAC). According to the stylus profilometer measurements, the thickness was 0.3 μm in the left panel of Fig. 4.11, 1.1 μm in the center panel, and 1.3 μm in the right panel.

Assuming a close-packed structure with a TPB molecular density of 1.079 g/cm^3, the computed total TPB coating amount was 32 μg/cm^2 (= 0.3 [μm]×1.079 [g/cm^3]). In contrast, the actual TPB mass

measured by the QCM sensor was 2 µg/cm^2. This resulted in an estimated filling rate of approximately 6%. The filling rate exhibited an upward trend with increasing TPB deposition mass, reaching 12% at 15 µg/cm^2 and 18% at 25 µg/cm^2.

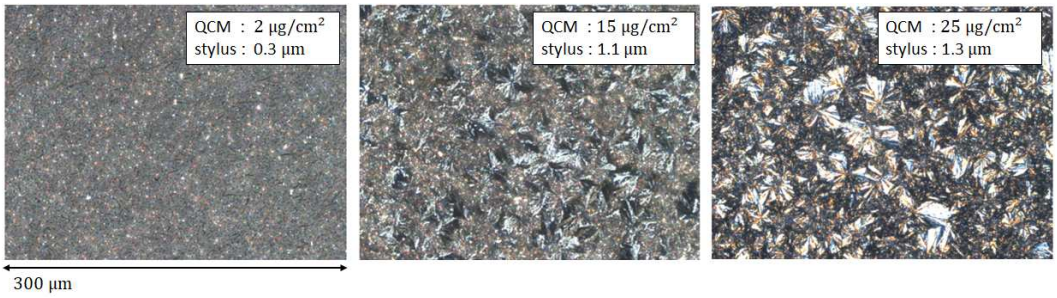

Fig. 4.11. Images of the surface condition of the TPB coating observed under a polarizing microscope. The crystalline structure grew with the increase in the TPB deposition mass.

4.4 Optical validation of TPB coating

Figure 4.12 shows the schematics of setup for measuring relative wavelength-shifting efficiency (left panel) and transmittance (center panel) of the TPB coating. Six acrylic disks (diameter = 7 cm, thickness = 3 mm) served as validation samples with varying TPB densities (0 – 35 µg/cm^2). Each acrylic disk had a PMT installed on its non-coated side, and a cylinder was mounted on the opposite (TPB coated) side to accommodate the light sources. For the relative wavelength-shifting efficiency measurement, the gaseous argon scintillation were induced by α-rays from a ^{241}Am source mounted on the cylinder wall. The gaseous argon purity was maintained by continuous gas flow into the cylinder. The PMT detected the converted argon scintillation light passing through the acrylic disk and the TPB coating itself. For the transmittance measurements, a pulsed LED with a pulse width of ten ns served as the light source. The emitted blue light from the LED resembled the blue light produced through TPB conversion.

The right panel of Fig. 4.12 illustrates the relative wavelength-shifting efficiencies (depicted by blue circles) and transmittances (depicted by red squares) of the six samples. The relative wavelength-shifting efficiency was determined as the average number of photoelectrons from the gaseous argon data, normalized by the case of the highest deposition mass of TPB ($\varepsilon_{TPB}/\varepsilon_{TPB}$ (32 µg/cm^2)). The transmittance was determined by comparing the peak of PMT signal waveform of the LED light data to that of the sample without TPB coating. While the absolute value of ε_{TPB} remains unknown, the relative wavelength shifting efficiency increased with the deposition mass, reaching saturation above 25 µg/cm^2. Contrary, the transmittance decreased with the TPB deposition mass but remained at approximately 80%, even in the saturation region of the relative wavelength-shifting efficiency.

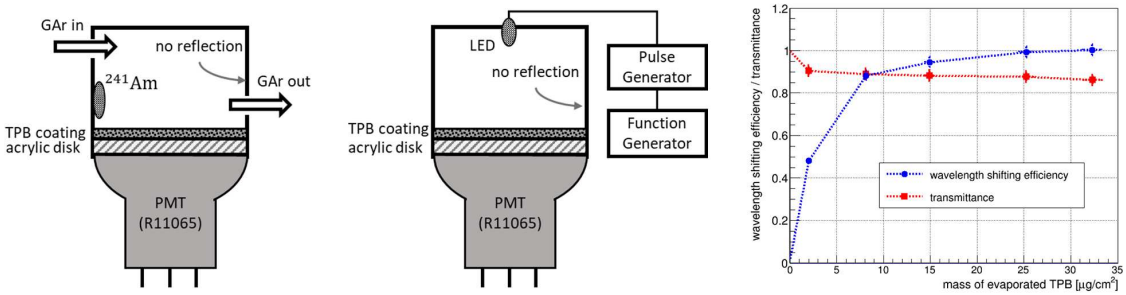

Fig. 4.12. Systems for measuring relative wavelength-shifting efficiency using the GAr scintillation induced by α-rays emitted from ^{241}Am (left) and transmittance under a blue LED (center). Measurements were performed on six acrylic disk samples deposited with TPB at different densities (0–35 μg/cm^2). Optical validation results of the TPB coating (right). The horizontal axis indicates the mass of the TPB deposited on the acrylic disks.

4.5 Light collection efficiency measurement with PMTs

4.5.1 Apparatus

We measured the observed light yield of a single-phase liquid argon detector designed to minimize photon loss, maximizing light collection efficiency. Figure 4.13 provides a schematic and image of the liquid argon scintillation detector. The main structure comprises a polytetrafluoroethylene (PTFE) sleeve, known for its high reflectivity in the visible light region. Additionally, a reflector foil (3M, enhanced specular reflector (ESR)) is positioned on the inner surface of the detector to further enhance the reflectivity compared to the PTFE wall alone. Two PMTs (Hamamatsu Photonics K.K., R11065) with a quantum efficiency of approximately 30% for TPB-converted blue light were employed. The TPB directly covered the PMT windows and the ESR. The TPB coating density on the PMT windows was adjusted to the minimum amount (30 μg/cm^2), maximizing the wavelength shifting efficiency and preventing a reduction in the transmittance of the converted light. In contrast, the TPB coating density on the ESR was higher (42 μg/cm^2) than that of the PMT windows, as the TPB coating density on the ESR is not influenced by the transmittance reduction. The PMTs are operated with a negative bias voltage, typically set at -1570 V. The field-shaping electrodes within the PTFE sleeve are likewise biased with the same voltage to maintain an electric field inside the fiducial volume of less than 1 V/cm, validated using finite element analysis conducted with Femtet [82].

4.5.2 Gain calibration of PMTs

The gain calibration of the PMT was performed using the setup depicted in Figure 4.14. The LED flashes in a room temperature environment outside the liquid argon vessel and is directed into the detector through an optical fiber. The LED is operates by voltage pulses of approximately 20 ns width, generated by a function generator plus a pulse generator. The intensity of the LED light is adjusted to yield an expected number of photons detected by the PMT of about 0.1 photons. The trigger is initiated by the signal from the function generator, and data is acquired by the FADC. The average waveform is presented

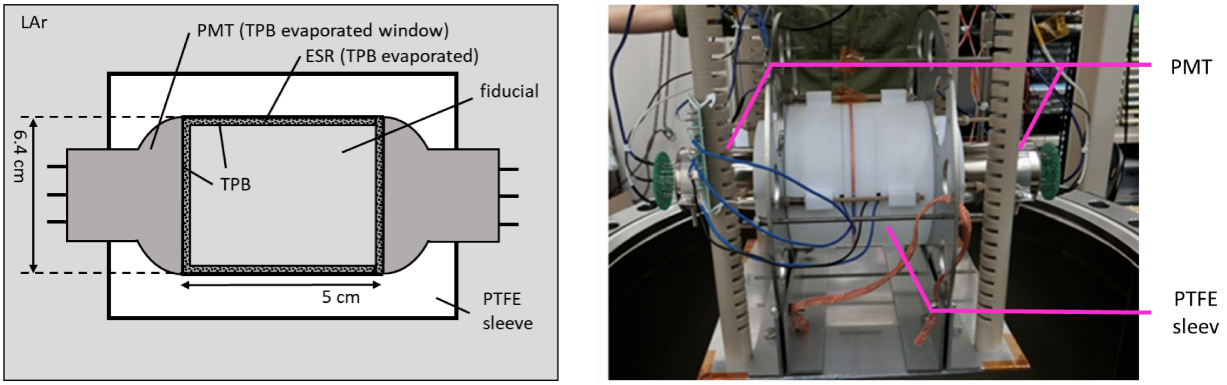

Fig. 4.13. Schematic and image of liquid argon detector.

in Figure 4.14. The pedestal was averaged over the time interval t=[-2 μs, -0.6 μs], and the PMT output charge is integrated over the time interval t=[+80 ns, +140 ns].

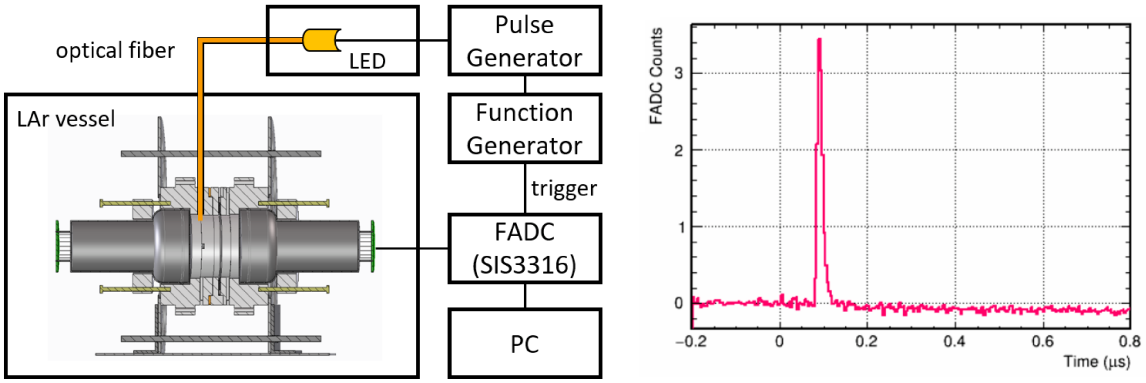

Fig. 4.14. Setup for PMT Gain calibration and observed waveform.

The gain value is calculated by fitting this distribution to model function [68]:

$$
\begin{aligned}
f(q) &= \sum_n P(n;\lambda) \times f_n(q), \\
f_n(q) &= \rho(q) \otimes \psi_1^{n*}(q), \\
\rho(q) &= G(q; x_0, \sigma_{\mathrm{ped}}), \\
\psi_1(q) &= \frac{p_E}{\tau} \exp(-q/\tau) + (1 - p_E) G(q; x_m, \sigma_m),
\end{aligned}
\tag{4.1}
$$

where $P(n;\lambda)$ represents a Poisson distribution with mean λ, $G(q;x,\sigma)$ denotes a Gaussian distribution with mean x and standard division σ, $\psi_1(q)$ represents the PMT single photoelectron response, $\psi_1^{n*}(q)$ represents the n-fold convolution of $\psi_1(q)$ with itself, and $\otimes$ denotes a convolution. This model assumes two components representing the PMT response: a photoelectron signal fully amplified by the dynode

chain represented by a simple Gaussian term, and underamplified photoelectrons and/or feedback from the dynode photoemission signal represented by an exponential term characterized by a parameter τ. The parameter p_E denotes the fraction of the single photoelectron response attributed to the underamplified terms. If there is no underamplified or dynode-feedback response in a PMT, p_E is 0, leading to a perfect description of the photoelectron response by Gaussians alone.

In Figure 4.15, the charge distribution of LED data is represented by the black plot, and the fitted result is indicated by the red line. Here, 1 count×sample is equivalent to an output charge of 9.8×10^{-15} C. The mean charge corresponding to a single photoelectron, denoted as g, is defined by the equation:

$$g = p_E\tau + (1 - p_E)x_m, \tag{4.2}$$

and it is calculated to be approximately $2.0 \times 10^6 = e^-$/p.e. at a PMT bias voltage of -1570 V.

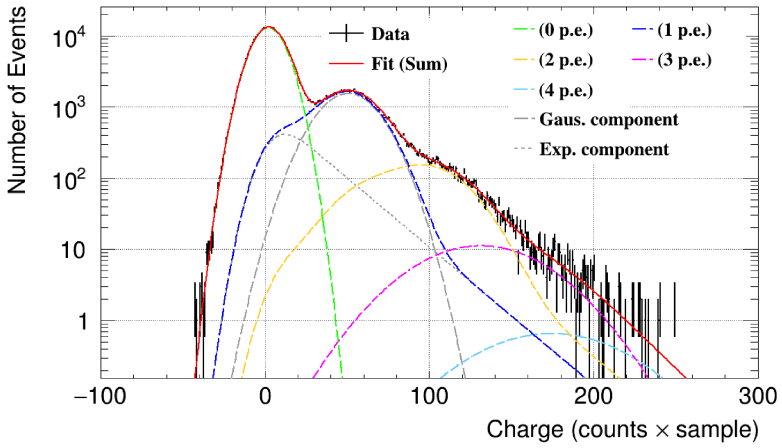

Fig. 4.15. Distribution and fitting result of PMT output charge for LED events at 1570 V.

4.5.3 Determination of light collection efficiency with ^{22}Na and ^{137}Cs

The light collection efficiency, defined as the number of photoelectrons per energy deposition of 1 keV, is determined by the full absorption peak corresponding to the 511 keV and 1274.6 keV γ rays from ^{22}Na and the 661.7 keV γ ray from ^{137}Cs. Fig. 4.16 shows the spectra of the argon scintillation photons observed using a ^{22}Na source (left panel) and ^{137}Cs source (right panel). In measurement with ^{22}Na, NaI(Ti) scintillator is positioned at opposite side of the liquid argon detector to tag the backward-traveling γ rays, resulting in blue plots in left panel of Fig. 4.16.

Each full absorption peak is fitted using a model function that consists of a Gaussian plus background, where the background comprises linear and error functions. The observed signal contains additional charge from PMT afterpulses of 2–4%, and there is underestimation from the photon-counting algorithm. These contributions are taken into account in the analysis. The measured light collection efficiency is summarized in Tab. 4.5. The observed light collection efficiency reached the expected maximum of

12.3 p.e./keVee with QE_{PMT} = 30% as mentioned before in Eq. (3.1). Therefore, we conclude that this detector achieved close to unity acceptance ($A_{vuv} \times \varepsilon_{WLS} \times A_{vis} = 1$) under the assumption of QE_{PMT} = 30%.

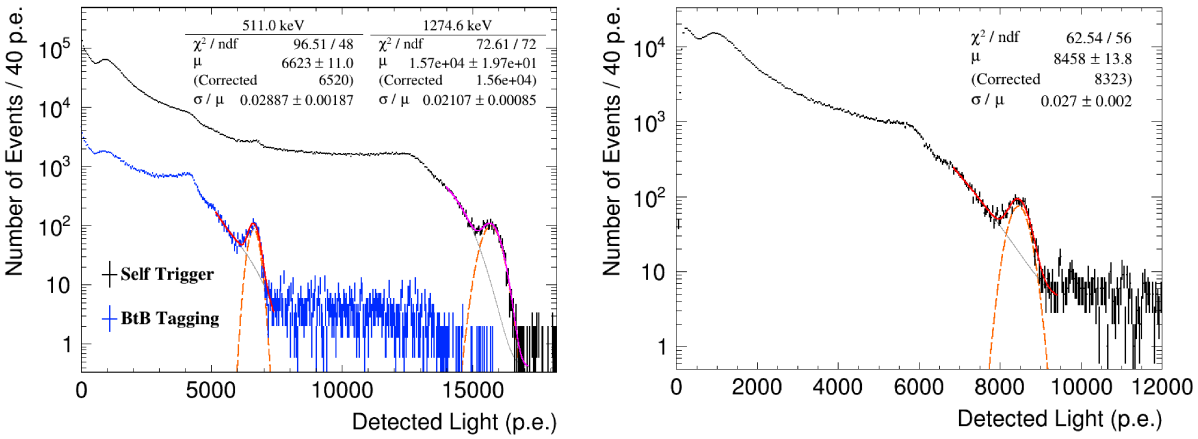

Fig. 4.16. Observed spectra of ^{22}Na and ^{137}Cs detected using the liquid argon detector, with the adjusted TPB coating based on the validation results. Each full absorptio peak was fitted to a Gaussian plus background function to estimate light collection efficiency.

Table 4.5. Fitted γ-ray energy E_γ and light collection efficiency μ/E_γ resulting from the full-absorption peak fit.The uncertainties include both statistical and systematic uncertainties.

E_γ [keV]	Source	μ/E_γ [p.e./keV]
511.0	^{22}Na	12.8 ± 0.3
661.7	^{137}Cs	12.6 ± 0.3
1274.6	^{22}Na	12.3 ± 0.3

4.5.4 PSD capability

We confirmed the light collection efficiency of 12.8 p.e./keVee, surpassing results from previous experiments. Subsequently, we evaluated the PSD capability of this detector. The PSD parameter Slow/Total is defined as follows:

$$Slow/Total = \frac{L_{slow}}{L_{total}} \tag{4.3}$$

where L_{total} represents the total integrated charge of the liquid argon signal over the range [−20 ns, +7 µs], and L_{slow} is the integrated charge after 120 ns. The mean μ and deviation σ of the PSD distribution are determined from ^{22}Na data for ER events and ^{252}Cf data for NR events. The PSD distribution, segmented

by a certain energy width, is empirically modeled by a beta distribution:

$$
\begin{aligned}
f(x;\alpha,\beta) &= A \times \frac{x^{\alpha-1}\,(1-x)^{\beta-1}}{B(\alpha,\beta)}, \\
B(\alpha,\beta) &= \int_0^1 x^{\alpha-1}\,(1-x)^{\beta-1}\,dx, \\
\alpha = \frac{\mu^2\,(1-\mu)}{\sigma^2} - \mu \quad &, \quad \beta = (\frac{1}{\mu} - 1)\,\alpha.
\end{aligned}
\tag{4.4}
$$

Initially, the mean μ_{ER} and deviation σ_{ER} for ER events are determined. The histograms in Fig. 4.17 display PSD distributions segmented by 5-photon bins of the ^{22}Na data, with the blue line representing the fitting results. Next, to calculate the mean μ_{NR} and deviation σ_{NR} of the NR events, a similar fit is performed for ^{252}Cf. As ^{252}Cf data includes both NR and ER events, it is modeled as the sum of two beta distributions. Here, the mean μ_{ER} and deviation σ_{ER} of the ER distribution are fixed to the results determined from the ^{22}Na data. Therefore, A_{ER}, A_{NR}, μ_{NR}, and σ_{NR} are the fitted parameters for the ^{252}Cf data. The histograms in Fig. 4.18 display PSD distributions segmented by 5-photon widths of the ^{252}Cf data. The black lines represent the results of the fits, and the blue and red lines indicate the ER and NR contributions, respectively. This fitting process is performed up to 500 photons for both ^{22}Na and ^{252}Cf data. Finally, in Fig. 4.19, the PSD distributions as a function of the number of detected photoelectrons for ^{22}Na and ^{252}Cf are presented. The PSD central value obtained from the fit, along with the $\pm 2\sigma$ band, is superimposed.

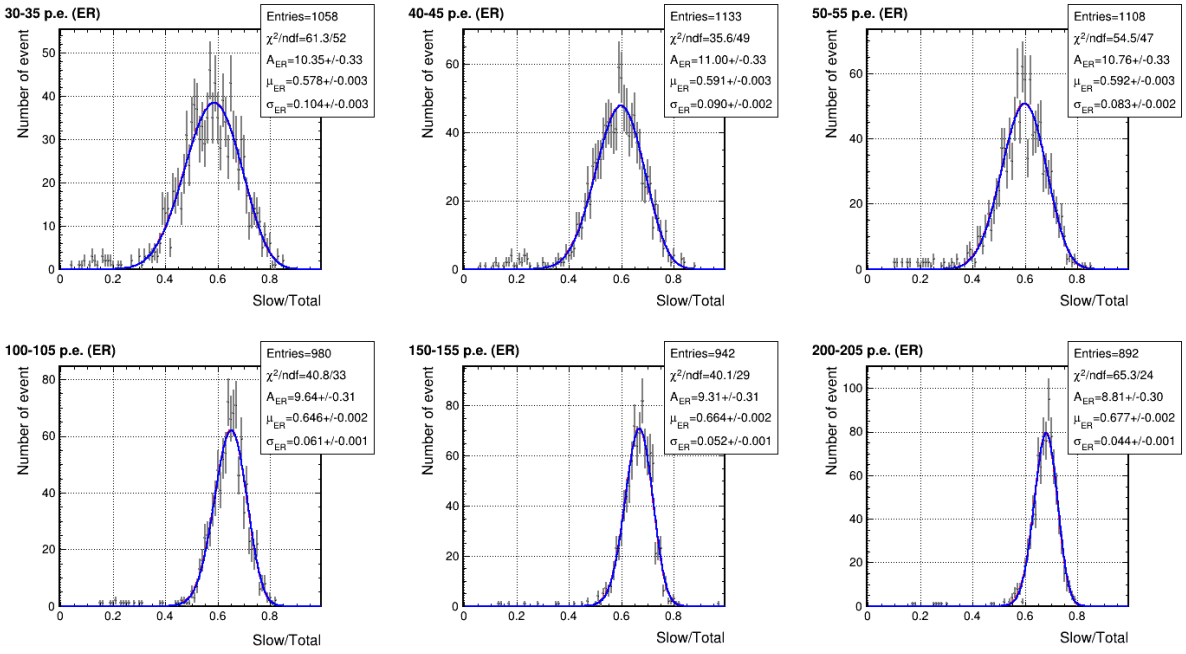

Fig. 4.17. PSD distributions for ER events segmented by 5-photon bins of the ^{22}Na data (gray histograms) and the fitting result (blue line). (Top left: 30-35 p.e., Top center: 40-45 p.e., Top right: 50-55 p.e., Bottom left: 100-105 p.e., Bottom center: 150-155 p.e., Bottom right: 200-205 p.e.).

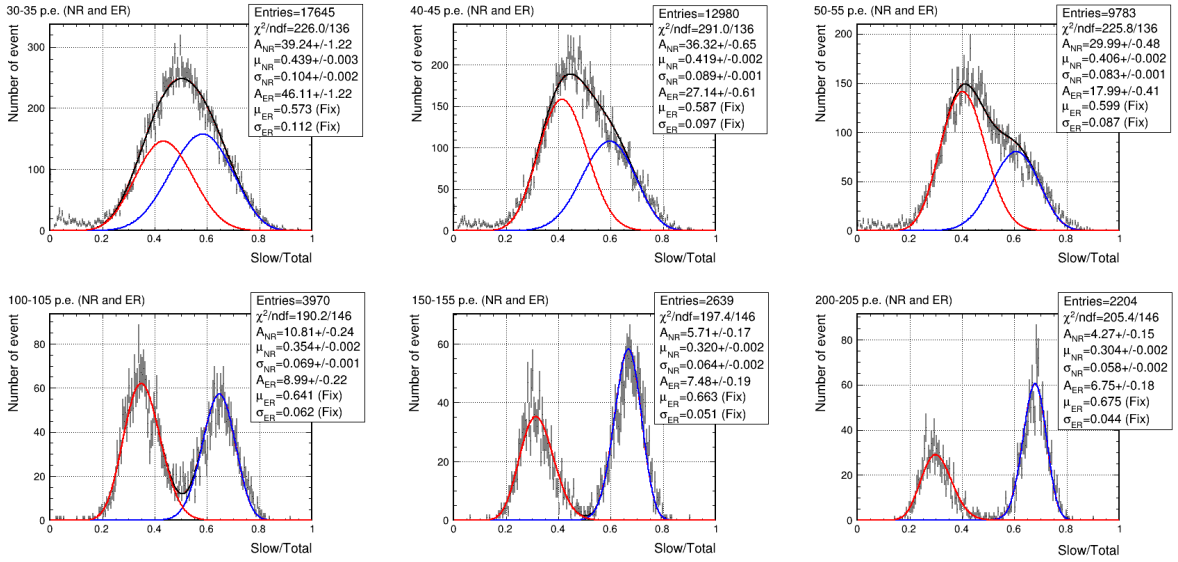

Fig. 4.18. PSD distributions for NR events segmented by 5-photon bins of the ^{252}Cf data (gray histograms) and the fitting result (black line). The ER and NR contributions are indicated by the blue and red lines, respectively. (Top left: 30-35 p.e., Top center: 40-45 p.e., Top right: 50-55 p.e., Bottom left: 100-105 p.e., Bottom center: 150-155 p.e., Bottom right: 200-205 p.e.).

We conducted a similar analysis for ER events using data obtained from a detector with a light collection efficiency of 5.7 p.e./keVee (details in Ref.[47]). The left panel of Fig. 4.20 depicts the mean value as a function of recoil energy, while the right panel illustrates the deviation as a function of the number of detected photoelectrons. In both panels, the black line represents data acquired with a detector of 12.8 p.e./keVee, and the red line represents data acquired with 5.7 p.e./keVee. It's important to note that the central value of PSD varies with recoil energy, and the deviation is influenced by the number of detected photons.

Due to insufficient statistics in the data, a Monte Carlo simulation (MC) is employed to evaluate the PSD capability based on the obtained model. In the MC simulation, random PSD values are generated using the distribution obtained earlier. The central value of the PSD is obtained from the assumed recoil energy, while the deviation is derived based on the assumed number of detected photons (recoil energy $\times$ light collection efficiency). Both the actual data (black line) and the MC results (red line) are depicted in Fig. 4.21.

Although particle identification by PSD should be optimized to maximize sensitivity, we will simplify the discussion by focusing on the rejection power of ER events when applying a cut based on the PSD mean of NR. The rejection power of ER R^{ER}_{PSD} is defined as follows:

$$R^{ER}_{PSD} = \frac{N^{ER}_{gen}}{N_{<\mu_{NR}}}, \tag{4.5}$$

where N^{ER}_{gen} is the number of generated events simulating ER, and $N_{<\mu_{NR}}$ is the number of events with a Slow/Total lower than the NR PSD mean. Figure 4.22 illustrates the rejection power as a function

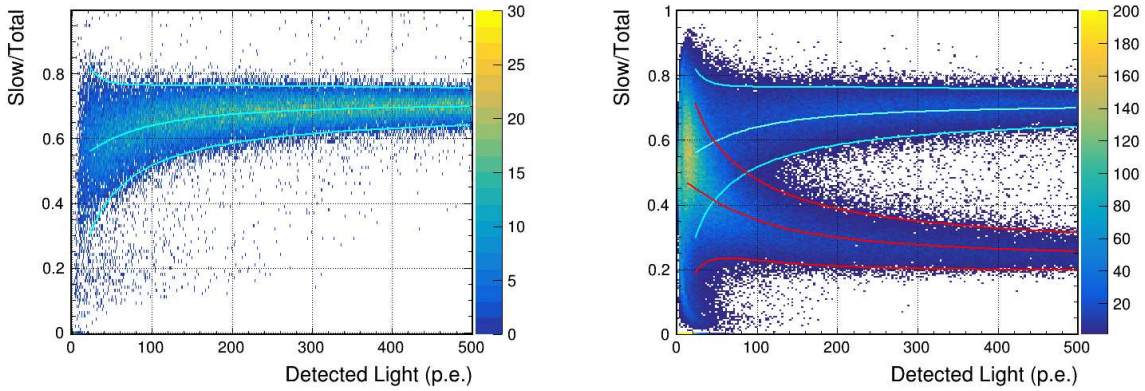

Fig. 4.19. PSD distributions as a function of the number of detected photoelectrons for ^{22}Na and ^{252}Cf. The fitting results for ER (light blue line) and NR (red line) are superimposed.

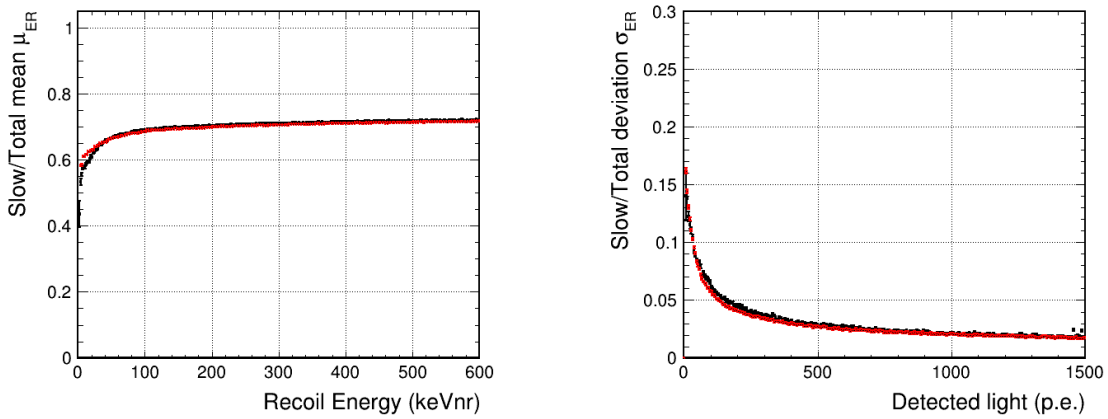

Fig. 4.20. Left panel: Mean value of PSD as a function of recoil energy for ER events. Right panel: Deviation as a function of the number of detected photoelectrons. The black line represents data acquired with a detector of 12.8 p.e./keVee, while the red line represents data acquired with 5.7 p.e./keVee.

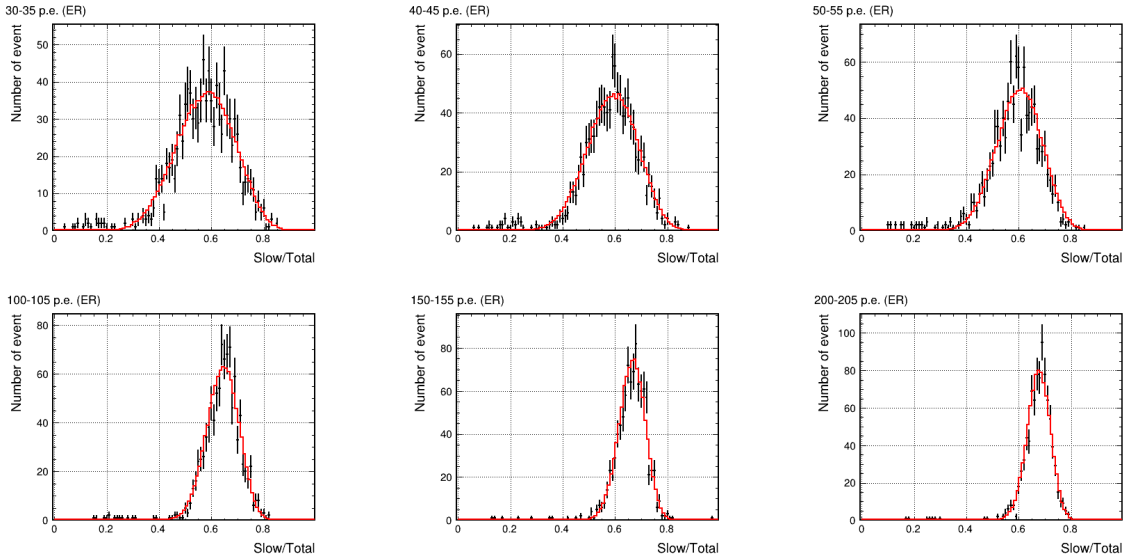

Fig. 4.21. Comparison between actual data (black line) and Monte Carlo simulation results (red line) for the PSD capability evaluation. (Top left: 30-35 p.e., Top center: 40-45 p.e., Top right: 50-55 p.e., Bottom left: 100-105 p.e., Bottom center: 150-155 p.e., Bottom right: 200-205 p.e.).

of recoil energy when the light collection efficiency is assumed to be 5.7 (black plots) and 12.8 (red plots) p.e./keVee. As expected, we observed an improvement in PSD capability with the enhanced light collection efficiency.

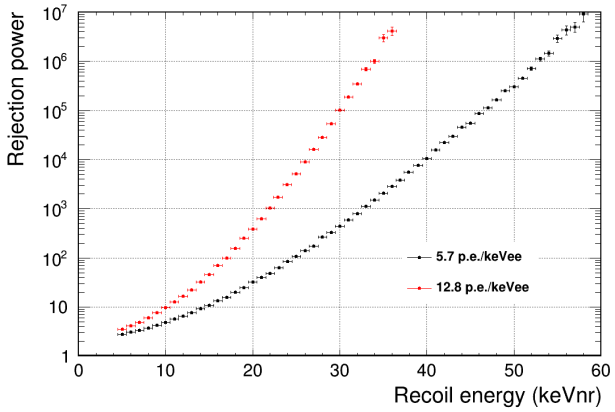

Fig. 4.22. Rejection power as a function of recoil energy. The black plots corresponds to a light collection efficiency of 5.7 p.e./keVee, while the red plots corresponds to a 12.8 p.e./keVee.

CHAPTER 5

Installation of TSV–MPPC to liquid argon detector

Implementing a higher-sensitive photosensor is essential to improve the light collection efficiency of the liquid argon scintillation detector. TSV–MPPC, a type of Silicon Photomultiplier (SiPM), is known for its superior sensitivity to visible light compared to the PMT used in Chapter 4. To assess its performance in a liquid argon environment, we initially conducted a test using a single-channel TSV–MPPC, as its functionality at liquid argon temperatures was unverified. Subsequently, we proceeded to construct a small-sized liquid argon detector incorporating TSV–MPPC. This chapter details the TSV–MPPC installation process.

5.1 Multi Pixel Photon Counter

The Multi Pixel Photon Counter (MPPC) is a photon-counting semiconductor detector manufactured by Hamamatsu Photonics K.K. It consists of an Avalanche Photo Diode (APD) connected in series with a quenching resistor, forming the fundamental unit (one pixel), arranged in two dimensions in parallel. When a photon strikes a pixel and generates an electron-hole pair, avalanche amplification occurs in the APD. The avalanche amplification in the APD stops after a brief period, enabling the detection of the next photon. As each pixel's output is intentionally standardized, the charge output from the MPPC is directly proportional to the number of pixels that detected the photon. For example, if two pixels detect a photon, the output is twice that of one pixel. Figure 5.1 illustrates a typical waveform of the MPPC acquired by the FADC, corresponding to the output of 1 (around -189 µs) and 2 pixels (around -190 µs), respectively.

MPPC functions as a photodetection device with several advantages, including high photon detection efficiency, large gain, one-photon identification capability, low voltage operation (around 50 V), and insensitivity to magnetic fields. The applied voltage influences both the photon detection efficiency and gain, with higher applied voltages leading to increased performance. The output charge of the MPPC is known to vary with the breakdown voltage, which is influenced by temperature. Consequently, the MPPC signal is temperature-dependent. However, throughout our experiment, the MPPC operated at the temperature of liquid argon (87 K), resulting in negligible fluctuations in output values and other parameters due to temperature changes.

On the other hand, the MPPC exhibits characteristics that require attention, including crosstalk, afterpulses, and latching. Crosstalk is a phenomenon in which a photon, produced during avalanche amplification, generates an electron-hole pair in another pixel, causing avalanche amplification in that pixel as well. This leads to an increase in the output charge by an integer factor. Afterpulses appear

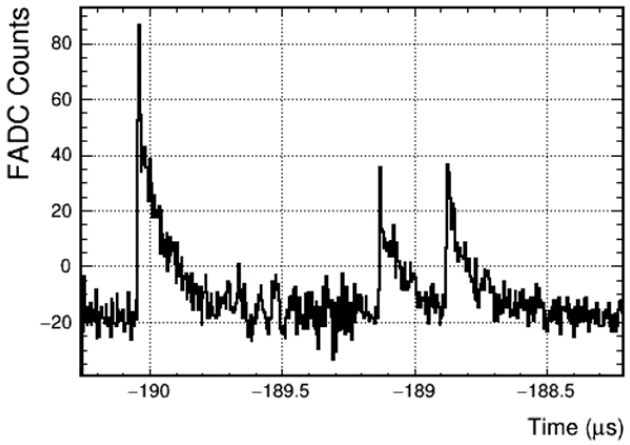

Fig. 5.1. Typical signal waveform of MPPC correspond to a few photons.

as delayed output in the same pixel after the incident photon due to the release of a trapped electrons. Latching occurs when the MPPC operates at a high applied voltage, and insufficient quenching allows current to persist. In a room temperature environment, the MPPC is warmed by the signal current, causing an increase in the breakdown voltage. However, in a low-temperature environment, the breakdown voltage remains stable, resulting in a relatively higher output charge. These phenomena are more likely to occur at higher applied MPPC voltages, creating a trade-off between photon detection efficiency and gain, thereby impacting the MPPC resolution

As shown in Fig. 5.1, the rise of the MPPC signal is sharp due to the current caused by the Geiger discharge of the APD. Thereafter, the fall is relatively slow because charging proceeds with a time constant that depends on the value of the capacitance and resistance of the MPPC. The equivalent circuit of MPPC is expressed using the capacitance C_{1pix} of the semiconductor sensor per pixel, the quenching resistance R_{1pix}, and the number of pixels n_{pix}. If there is a resistance of $R_{receive}$ exists in the readout circuit, the time constant τ_{MPPC} is expressed as follows:

$$\tau_{MPPC} = n_{pix} C_{1pix} \times (\frac{R_{1pix}}{n_{pix}} + R_{receive}). \tag{5.1}$$

The photon detection efficiency, gain, and time constant are contingent on the size of an pixel. A larger pixel corresponds to a higher detection efficiency of photons due to the larger aperture ratio. The aperture ratio represents the proportion of the area where photons can be detected within the photosensitive area of the MPPC. Moreover, as the pixel size increases, so does the capacitance per pixel C_{1pix}. Consequently, a larger pixel size results in a higher gain and a longer time constant. Additionally, the dynamic range of the MPPC is influenced by the number of pixels within the device, with a larger number leading to a broader range. A smaller pixel pitch corresponds to a higher number of pixel, thereby expanding the dynamic range in terms of the number of detected photons, even with the same physical size. In this way, a trade-off relationship exists with respect to pixel pitch.

5.1.1 Requirement

The following are some of the requirements for liquid argon scintillation detection devices:

(1) Stable operation in low-temperature environment: In this study, the photodetector needs to operate stably in an low-temperature environment of 87 K because the device is immersed in liquid argon for experimental use.

(2) Adequate light detection area: In dark matter search experiments, sensitivity improves with an increase in the mass of the target material. However, as detectors grow in size, there is a corresponding increase in the total required light detection area. Given that the light detection area of the MPPC is on the order of square centimeters, an inevitable consequence is the need for an increase in the number of channels. Consequently, a circuit was developed to efficiently manage the MPPC voltage application and signal readout by reducing the number of channels.

(3) Time constant not degrading liquid argon PSD capability: The signal waveform of the MPPC has an impact on the liquid argon PSD, influenced by different factors for high and low intensities of detected photons. In situations where the number of photons detected in each channel is small, leading to the discrete output of one photon, the rise time significantly affects the PSD resolution. A sharper rise contributes to an enhanced PSD resolution. Conversely, in scenarios with a substantial quantity of light and continuous MPPC output, the decay time constant also affects the PSD capability. It has been established that a time constant below 100 ns does not compromise the PSD capability.

(4) High Gain for Identifying Single Photons: When calculating the gain and crosstalk of the MPPC, peaks for 1, 2, ..., photons are separated in the distribution. Furthermore, in scenarios involving events with low light quantity where the MPPC output is discretized, it is preferable for the output of a single photon to be significantly larger than the noise. Consequently, a sufficiently high gain is necessary for these reasons.

(5) High Detection Efficiency for Liquid Argon Wavelength-Converted Light: For the main theme of this study — enhancing detection sensitivity in liquid argon detectors through increased light collection efficiency —it is crucial to utilize a light detection device with the highest possible sensitivity.

5.1.2 TSV-MPPC

In this study, a Through Silicon Via (TSV) type MPPC was employed. TSV incorporates electrodes passing through the silicon, without electrodes on the outer periphery of the package. Consequently, the gap between the photosensitive area and the side of the package is 200 µm on all four sides, smaller than that of a typical MPPC. This reduced gap is advantageous for photon collection efficiency as dead space is minimized when multiple channels of MPPCs are arranged. Hamamatsu Photonics K.K. offers the commercially available 1-channel type (S13360) and the Array type (SIS3316), where multiple MPPCs are assembled as a single unit. The left panel of Fig. 5.2 displays the photosensitive surface of the 1-channel type, with a silicon through via electrodes running through the four light-colored squares area.

The right panel of Fig. 5.2 displays the Array type arranged in a 4×4 row of single types. Each of the 16 MPPCs is subjected to different voltages, and their respective signals are read individually.

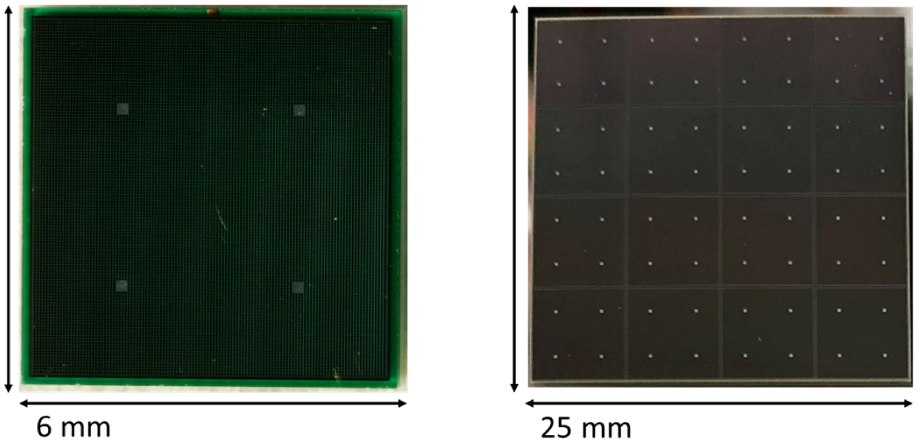

Fig. 5.2. Left panel: Photosensitive surface of the 1-channel TSV–MPPC (S13360) with silicon through via electrodes. Right panel: Array type (SIS3316) consisting of a 4×4 arrangement of individual MPPCs.

Figure 5.3 presents specifications for photon detection efficiency (hereafter referred to as PDE), gain, and crosstalk probability of the TSV-MPPC (S13361-6050 series) with a pixel size of 50 µm, as a function of overvoltage, as published by Hamamatsu Photonics K.K. The PDE is notably high, surpassing 50% for 420 nm light. Furthermore, the PDE exceeds 60% for the TSV-MPPC with a pixel pitch of 75 µm (hereafter referred to as 75U), owing to the larger aperture ratio compared to the TSV-MPPC with a pixel pitch of 50 µm (hereafter referred to as 50U).

Thus, some TSV-MPPCs are more sensitive to visible light than PMTs. In addition, it is relatively easy to realize a large photosensitive area since the Array type is available. Therefore, in this study, the TSV-MPPC was chosen as a candidate MPPC to be implemented in the liquid argon detector, and the light collection efficiency is expected to be more than twice that of the conventional MPPC by introducing the TSV-MPPC in the liquid argon detector instead of the PMT. However, it's important to note that the operating temperature guaranteed by Hamamatsu Photonics for the TSV type is above -20 °C and is not intended for use at liquid argon temperature (87 K).

5.2 Low-temperature tolerance test of single-chip TSV–MPPC

5.2.1 Apparatus

The operability of the TSV–MPPC, known for its a high PDE, was evaluated using the setup depicted in Fig. 5.4. This test followed the procedure that reported in Ref.[64]. The light sources employed were the liquid argon scintillations induced by α-rays emitted from ^{241}Am (E_α = 5.5 MeV) and a blue LED with a pulse width of 10 ns. The pulse generator served the dual-purpose of providing the driving voltage for

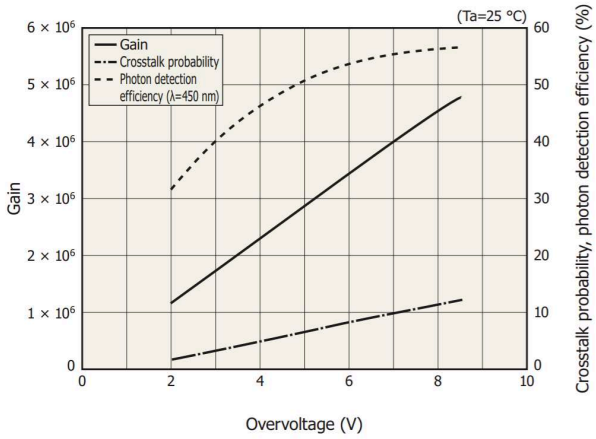

Fig. 5.3. Specifications for PDE, gain, and crosstalk probability of the TSV-MPPC (S13361-6050 series) with a pixel size of 50 µm, as a function of overvoltage. This figure is taken from Ref.[83].

the LED and acting as the trigger for data acquisition during LED calibration. The average number of photons from the LED observed by the MPPC was adjusted to be less than one photon per pulse. The MPPC used in this test was a single-chip TSV–MPPC (Hamamatsu Photonics K.K., S13360-6050VE) with a gain of 1.7×10^6 at the bias voltage recommended by Hamamatsu Photonics K.K. It was 6×6 mm in size and had a 50 µm pixel pitch. The TSV–MPPC window, positioned 1.5 cm above the ^{241}Am source, was coated with a 30.6 µg/cm^2 of TPB. During the low-temperature tolerance test, the entire apparatus was immersed in liquid argon. The MPPC driver kit (Hamamatsu Photonics K.K., C12332-01) provided the MPPC bias voltage and amplified the signal, with a signal amplification gain of 10.9 ± 0.1. The MPPC signal was digitized using a flash analog-to-digital converter (Struck, SIS3316) with a 250 MHz sampling rate and recorded as a waveform.

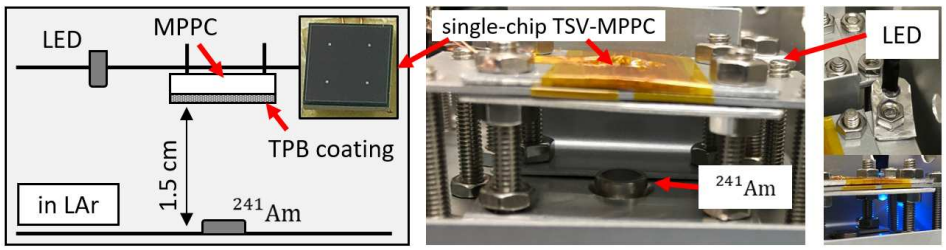

Fig. 5.4. Apparatus of the low-temperature tolerance test. The liquid argon scintillation light was detected via the TSV–MPPC window coated with TPB (30.6 µg/cm^2).

5.2.2 analysis

The observed signal charge of the MPPC (Q_{obs}) is expressed as follows:

$$Q_{obs} = N_{obs} \times Q_{1pix} \times N_{pix}, \tag{5.2}$$

where N_{obs} represents the number of photons observed in MPPC, Q_{1pix} is the signal charge of one pixel of MPPC, and N_{pix} is the number of pixels with an electron-hole pair per single-photon detection. N_{pix} is greater than one due to optical crosstalk and after-pulses in the MPPC. The values of Q_{1pix} and N_{pix} were determined using the LED data. The left plot in Fig. 5.5 illustrates the charge distribution of the LED data acquired at an MPPC bias voltage of 44 V. The signal charge was obtained by integrating a waveform over the range [−20 ns, +400 ns], based on the timing of the LED pulses. In the charge distribution, the first and second peaks correspond to zero (pedestal) and one pixel hit events, respectively. The number of pedestal events (N_0) is assumed to follow a Poisson distribution:

$$N_0 = N_{all} \times \mathrm{P}(\mathrm{n} = 0; \mu) = N_{all} \times e^{-\mu}, \tag{5.3}$$

where $\mathrm{P}(n; \mu)$ represents a Poisson distribution with mean μ, and N_{all} is the total number of events. The parameter μ, corresponding to N_{obs}, is calculated from the number of pedestal events. In contrast, events with one or more pixel hits deviate from a Poisson distribution because of the optical crosstalk and after-pulses. Additionally, Q_{1pix} is defined as the difference in the FADC counts between the zero and one pixel hit peaks. Therefore, the charge distribution was modeled using the following function:

$$f = N_{all} \times \{\mathrm{P}(0; \mu) \times \mathrm{G}_0 + \sum_{n=1}^{4} A_n \times \mathrm{G}_\mathrm{n}\}, \tag{5.4}$$

$$\mathrm{G}_\mathrm{n} = \mathrm{Gaus}(q; Q_{ped} + n \times Q_{1pix}, \sqrt{\sigma_{ped}^2 + n \times \sigma_{1pix}^2}) \qquad (0 \leq n \leq 4), \tag{5.5}$$

where $\mathrm{Gaus}(q; Q, \sigma)$ is a Gaussian distribution with mean Q and standard deviation σ, Q_{ped} and σ_{ped} are the Gaussian mean value and standard deviation of the pedestal, respectively, σ_{1pix} is the standard deviation of the single pixel pulse, and A_n is the scale value of n-th ($1 \leq \mathrm{n} \leq 4$) Gaussian. The fitted parameters include μ, A_n, Q_{ped}, σ_{ped}, Q_{1pix}, σ_{1pix}. Additionally, a mean count of the left plot in Fig. 5.5 ($\langle Q_{obs} \rangle$) satisfies Eq. 5.2, represented by the following function:

$$\langle Q_{obs} \rangle = \mu \times Q_{1pix} \times N_{pix}. \tag{5.6}$$

Therefore, N_{pix} was determined using μ, Q_{1pix}, and $\langle Q_{obs} \rangle$. As a result of the aforementioned analysis, Q_{1pix} was found to be 248.3±0.5 FADC counts and N_{pix} is 1.027±0.015 at the MPPC bias voltage of 44 V. It is well known that both Q_{1pix} and N_{pix} exhibit dependencies on overvoltage; thus, the same analysis was repeated at nine bias voltage (V_{bias}) points from 43 V to 48 V. The center and right plots in Fig. 5.5 show the results of Q_{1pix} and N_{pix}, respectively. The determination of the breakdown voltage V_{bd} involved fitting the Q_{1pix} data points as a function of V_{bias} using the following function:

$$Q_{1pix} = k \times (V_{bias} - V_{bd}) \equiv k \times V_{ov}, \tag{5.7}$$

where the overvoltage V_{ov} is defined as $V_{bias} - V_{bd}$. Subsequently, the N_{pix} data points, plotted as a function of V_{ov}, were fitted to the following function,

$$N_{pix} = 1 + p_0 \times (V_{ov})^{p_1}. \tag{5.8}$$

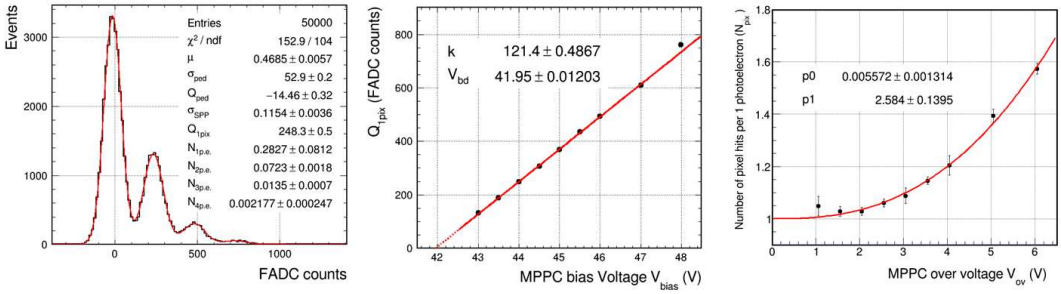

Fig. 5.5. Charge distribution of the LED light (left), and the results of Q_{1pix} (center) and N_{pix} (right) estimated from the charge-distribution fitting. The red lines are the fitting function. These parameters indicate that the TSV–MPPC preserves its well-known features, even at the liquid argon temperature (87 K).

The left and center panels of Fig. 5.6 show the charge distribution of the ^{241}Am data and the average waveform of the events around the peak of the ^{241}Am α-rays at the MPPC overvoltage of approximately 3 V. The total charge was derived by integrating the waveform over the temporal range of t = [−1 µs, +20 µs]. The lifetime of the average waveform is consistent with the triplet component of the liquid argon scintillations (τ_{slow} = 1.6 µs). The PDE was determined as follows:

$$PDE = \frac{N_{obs,\alpha}}{N_{\gamma,\alpha}} = \frac{1}{N_{\gamma,\alpha}} \frac{Q_{obs,\alpha}}{Q_{1pix} \times N_{pix}}, \tag{5.9}$$

where $N_{\gamma,\alpha}$, $N_{obs,\alpha}$, and $Q_{obs,\alpha}$ represent the expected number of photons reaching the MPPC photon detection area, the number of photons detected by the MPPC, and the observed signal charge, respectively, for the 5.5 MeV α-ray in the ^{241}Am data. $Q_{obs,\alpha}$ is obtained by fitting the ^{241}Am peak with a single Gaussian function (as shown in the left panel of Fig. 5.6). Q_{1pix} and N_{pix} are assumed to be the same as the LED data. $N_{\gamma,\alpha}$ is calculated using Eq. (3.1):

$$N_{\gamma,\alpha} = \frac{E_\alpha}{W_\alpha} \times A_{VUV} \times \varepsilon_{WLS} \times A_{vis} \tag{5.10}$$

$$= \frac{5.5\,\mathrm{MeV}}{27.5\,\mathrm{eV}} \times 1.2\% \times 1 \times 50\% = 1200\,\mathrm{photons}. \tag{5.11}$$

$N_{\gamma,\alpha}$ = 1200 photons is calculated under specific assumptions: the distance between the MPPC surface and the ^{241}Am source (1.5 ± 0.05 cm, geometrical acceptance A_{VUV} = 1.2%), the liquid argon scintillation emission yield for α-rays (W_α = 27.5 eV/photon [84]), and the wavelength shifting efficiency of the TPB (ε_{WLS} = 1). Furthermore, it was assumed that photon emission from TPB is uniformly isotropic; hence, half the photons converted by TPB inject into MPPC (A_{vis} = 50%).

The right panel of Fig. 5.6 shows the PDE of the TPB-converted liquid argon scintillation light as a function of the MPPC overvoltage. The uncertainty in the PDE is attributed to fitting errors in Q_{1pix}, N_{pix}, and $Q_{obs,\alpha}$, as well as misalignment in the distance between ^{241}Am source and the MPPC surface. The PDE of the TSV–MPPC was approximately 40% and 50% at V_{ov} = 3 and 5 V, respectively. These results confirmed that the TSV–MPPC operates effectively in the liquid argon environment, exhibiting higher efficiency in detecting TPB-converted visible light compared to PMTs.

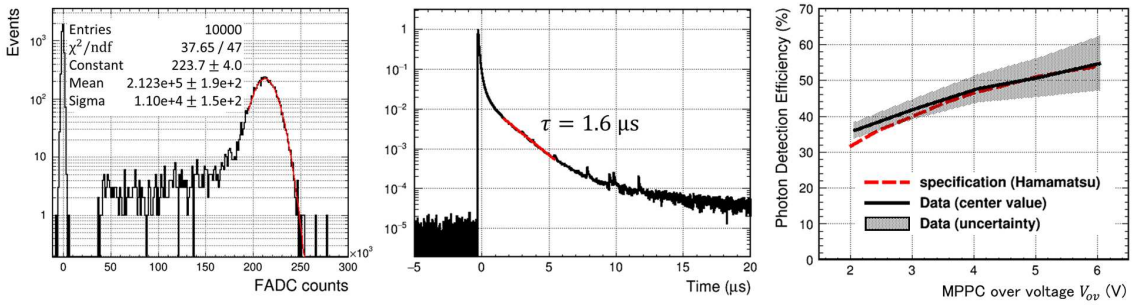

Fig. 5.6. Charge distribution detected by TSV–MPPC, showing a peak of α-rays emitted from ^{241}Am (left), average waveform of the liquid argon scintillation light detected by TSV–MPPC (center), and measured PDE of TSV–MPPC as a function of MPPC overvoltage (right). The black solid line and red dashed line in the right panel plot the measured PDE and the PDE in the TSV–MPPC specifications, respectively, and the black band shows the uncertainties in the measurements.

5.3 Demonstration of liquid argon detector using TSV–MPPC Arrays

The basic characteristics were measured using a single-chip TSV–MPPC, as described above. Subsequently, the operability of the liquid argon detector was demonstrated using a 4×4 array-type TSV–MPPC, necessitated by the need for larger light-detection coverage in practical applications.

5.3.1 Readout printed circuit board of TSV–MPPC array

In this study, the TSV–MPPC array utilized was a 4×4 assemblage of TSV–MPPC chips (Hamamatsu Photonics K.K., S13361-6050AE-04 and S13361-6075AE-04 with the pixel size of 50 μm and 75 μm, respectively). The array covered an area of 2.5×2.5 cm^2, and the sensor's underside featured two electrical connectors (SAMTEC, ST4-40-1.00-L-D-P-TR). As shown in Fig. 5.7, the readout board designed for TSV–MPPC array was a double-sided printed circuit board (PCB) measuring 50.5 mm × 80.5 mm × 1.6 mm in dimensions. Four (2-column×2-row) TSV–MPPC arrays were mounted on the PCB. To prevent an increase the number of readout channels, four independent MPPC chips (1-column×4-row) were merged by a connection circuit (depicted in the left panel of Fig. 5.8) integrated on the readout PCB. The concept of the circuit was originally developed in the $\mu \to e\gamma$ (MEG) experiment [85]. Coupling capacitors (100 nF) were interposed between adjacent MPPCs, while resistances (1.0 kΩ) were connected perpendicularly to the line of interconnected MPPCs and capacitors. The values of capacitors and resistances were chosen

through SPICE simulation to ensure that they do not alter the MPPC waveform. As the MPPC signal was propagated through the series connection, its lifetime decreased as the number of connections increased. Conversely, the MPPC bias voltage was supplied through a parallel connection, remaining independent of the number of MPPC connections. The right panel in Fig. 5.8 compares the average signal waveforms of single-chip and connected TSV–MPPCs using laser light at room temperature (approximately 300 K). The connected TSV–MPPC exhibited a shorter signal lifetime compared to the single-chip TSV–MPPC. Additionally, the readout PCB merged two high-voltage (HV) lines into one line, with each HV line operating two signal channels (equivalent to eight MPPC chips). In this configuration, 64 TSV–MPPC chips were managed by 8 HV lines, and 16 signal lines were extracted from the PCB through a flexible flat cable (FFC).

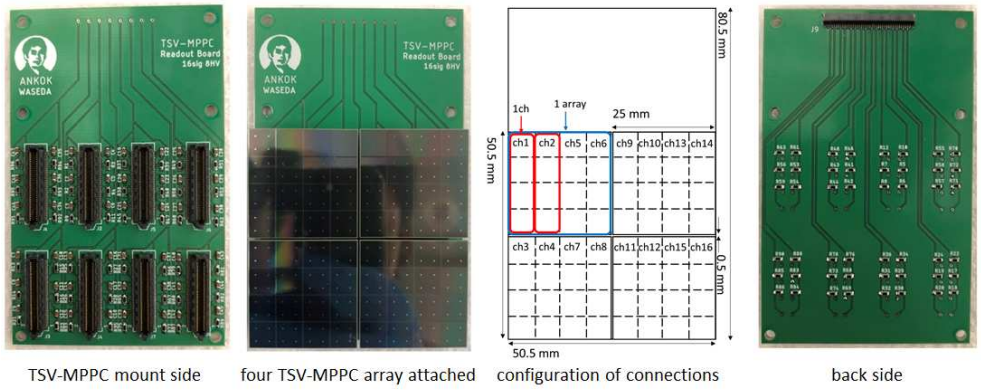

Fig. 5.7. Readout PCB of TSV–MPPC array with the connection circuit. Four arrays can be mounted on one PCB.

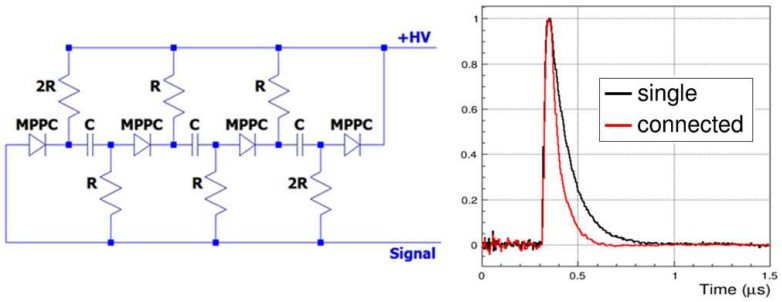

Fig. 5.8. Schematic of the MPPC connection (left) and average MPPC waveforms of a single-chip (black) and connected chips (red) obtained at room temperature (right).

5.3.2 Apparatus

Fig. 5.9 illustrates the single-phase liquid argon scintillation detector constructed with TSV–MPPC arrays. The fiducial volume, forming a cube with 5 cm edges, consisted of ESR and Teflon tape. Eight TSV–

MPPC arrays, comprising two readout PCBs and 32 signal channels, were positioned on opposite sides. To examine the impact of varying the pixel size, we utilized four MPPC arrays with a pixel pitch of 50 μm on one PCB and four MPPC arrays with a pixel pitch of 75 μm on the other PCB, denoted as 50U and 75U, respectively. TPB covered both the ESR (42 μg/cm^2) and the windows of the MPPC arrays (30 μg/cm^2). The MPPC bias voltage, set to 48 V for this measurement, was supplied by an MPPC driver kit (Hamamatsu Photonics K.K., C12332-01). To minimize the number of feedthroughs and cables, the HV line was divided into eight sublines within the liquid argon vessel. The MPPC signal exited the liquid argon vessel through a commercial D-sub feedthrough. and was then passed through a high-pass filter at room temperature before being digitized using a flash ADC (Struck SIS3316). A radioactive source (^{241}Am, 40 Bq) was positioned above the MPPC detector. The decay chain of ^{241}Am involves sequential processes:

$$^{241}\mathrm{Am} \rightarrow {}^{237}\mathrm{Np}^{*} + \alpha\ (5.49\ \mathrm{MeV}), \tag{5.12}$$

$$^{237}\mathrm{Np}^{*} \rightarrow {}^{237}\mathrm{Np} + \gamma\ (59.5\ \mathrm{keV}). \tag{5.13}$$

The γ-ray events inside the MPPC detector were identified by coincidence with the α-rays detected by five PMTs (Hamamatsu Photonics K.K. R6041-506 $\times$ 4, R11065 $\times$ 1) positioned above the MPPC detector. Additionally, a passive shield (consisting of 10 cm lead and 2 cm copper) was constructed around the liquid argon vessel to attenuate ambient γ-rays. Therefore, γ-ray events at 59.5 keV from ^{241}Am were detected with a high S/N at the MPPC detector.

A nanosecond pulsed laser light (THORLABS, NPL45B) was delivered to the MPPC detector via an optical fiber. The positioning and direction of the fiber within the detector were optimized to achieve a uniform distribution of observed photons across all 32 channels, with a variation within 20%.

Signal waveform

Fig. 5.10 displays the waveforms of all 32 channels acquired using the pulsed laser. The waveforms of the 75U and 50U are shown in red (left) and blue (right), respectively. The laser intensity was adjusted to yield several hundred photoelectrons per channel, similar to the ^{241}Am signal. All 32 channels were successfully read out without a any dead channels.

The waveforms in the Fig. 5.11 represent the summed waveforms of the laser data (left in red for 75U, right in blue for 50U). These waveforms were obtained by summing 16 channels of the waveforms for the 75U PCB or the 50U PCB, and by averaging 1000 events. As shown in Fig. 5.11, the waveform exhibits a rising time of several hundred nanoseconds and includes an undershoot. This distortion is primarily attributed to electrical crosstalk through the HV connections and D-sub feedthroughs. The left and right panels in Fig. 5.12 depict the summed waveform for the 75U and 50U PCBs, respectively, with the HV turned off for one PCB while the other PCB is turned on. As no real signals were expected without HV, these waveforms indicated approximately 20% electrical crosstalk between the 75U and 50U PCBs. In addition to the crosstalk between the two PCBs, crosstalk also occurred between channels within the same PCB. Determination of MPPC gain was also difficult due to poor S/N in the observed single photoelectron

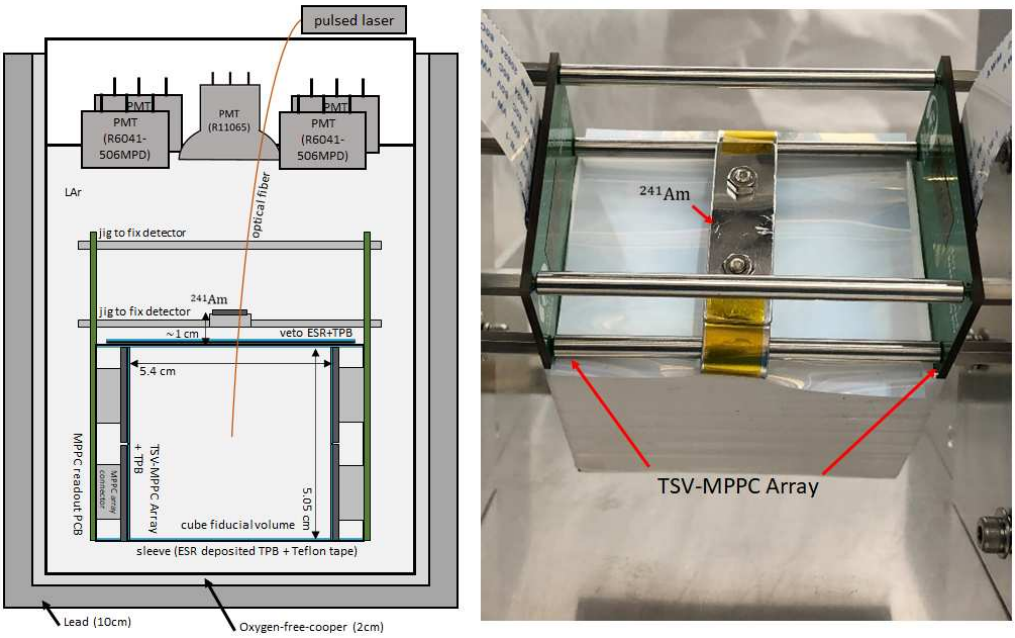

Fig. 5.9. Liquid argon scintillation detector with TSV–MPPC arrays. The fiducial volume (ESR and Teflon tape) was enclosed within sides of 5 cm. Eight TSV–MPPC arrays (two readout PCBs) were installed on the two facing sides. TPB was coated on the ESR (42 µg/cm^2) and the windows of the MPPC arrays (30 µg/cm^2).

signal. Consequently, it was challenging to determine the absolute observed light yield for this detector.

5.3.3 Response function relative to single photon detection

The response function of the detector for a single-photon signal is determined from laser data, where the expected number of detected photons is intentionally reduced using an optical filter. Figure 5.13 shows the distribution of integrals over the range t=[0 µs, 1 µs] for the reduced laser data with different filter attenuation rates of (top left: 1/4000, top right: 1/1600, bottom left: 1/800, bottom right: 1/500). In contrast to the single-channel test described in section 5.2, no amplifier was used, resulting in the pedestal and single-photon peak not being separated. To calculate the average number of detected photons (μ) and the integral value corresponding to one photon per channel ($Mean$), we simultaneously fit these distributions using the following equation:

$$
\begin{aligned}
f &= N_{all} \times \left[\mathrm{P}(0;\mu) \times \mathrm{G}_0 + \sum_{i=1}^{n} P(i;\mu) \times \left\{ (1-f_\tau)\, G_i \otimes \mathrm{Exp}(\tau) + f_\tau\, G_i \otimes \mathrm{Exp}(c_\tau \tau) \right\} \right], \quad (5.14)\\
\mathrm{G_n} &= \mathrm{Gaus}(q; n \times Q_{1pix}, \sigma_{ped}),\\
\tau &= Mean - Gain,
\end{aligned}
$$

where $\mathrm{P(n};\mu)$ is Poisson distribution with mean μ, $\mathrm{Exp(x};\tau)$ is exponential function, $\mathrm{Gaus}(q;Q,\sigma)$ is a Gaussian distribution with mean Q and standard deviation σ, and $\otimes$ denotes convolution. The

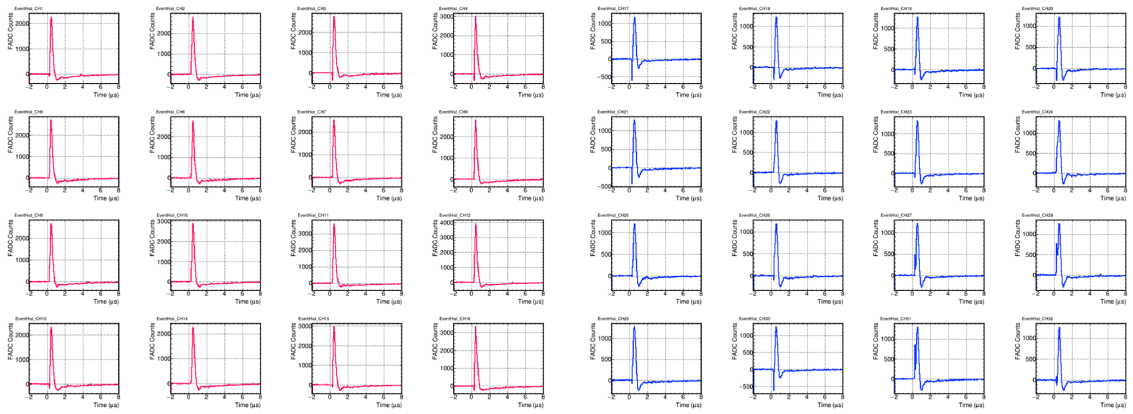

Fig. 5.10. Waveforms of laser data detected by TSV–MPPC arrays in the liquid argon environment. The red and blue waveforms were obtained at different pixel pitches of the MPPC (75U and 50U, respectively).

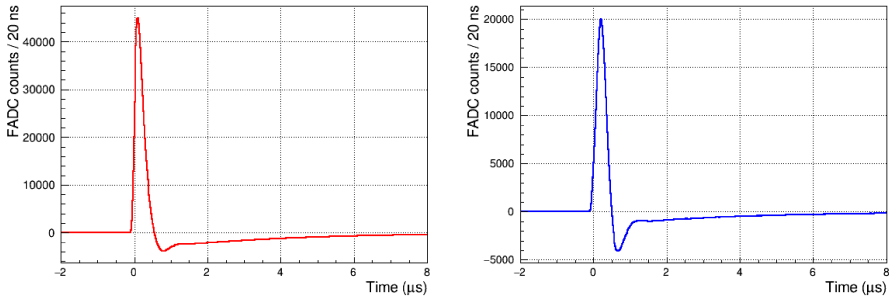

Fig. 5.11. Average waveforms of laser data detected by TSV–MPPC arrays (left: 75U, right: 50U).

fitting parameters include $Mean$, $Gain$, f_τ and c_τ, which are assumed to have equal values for the four distributions. Additionally, μ is scaled by attenuation rate of the optical filter ($\times 1, \times 2.5, \times 5, \times 8$). The parameter σ_{ped} is determined from laser-off data. The red line in Fig. 5.13 represents a typical fitting result for 75U channel.

To obtain the response function, the signal waveform is divided by the fitting results of μ and $Mean$ per channel. Subsequently, the waveforms from the 16 channels on either the 75U PCB or the 50U PCB are summed up, and the average is calculated over 1000 events. Figure. 5.14 displays the response functions for the 75U PCB in left panel and the 50U PCB in right panel. These response functions exhibit the same shape as the waveforms shown in Fig. 5.11.

5.3.4 Determination of light collection efficiency with TSV–MPPCs

The light collection efficiency is calculated from the full absorption peak of 59.5 keV gamma rays emitted by ^{241}Am. Figure 5.15 displays the summed waveforms and the integrated charge distributions for ^{241}Am data. The peaks in the integrated charge distributions around FADC counts of 6×10^4 (75U) and 2×10^4 (50U) correspond to the 59.5 keV γ-ray events. A factor 3 signal difference between 75U and 50U is attributed to variations in MPPC gain (approximately 2 times) and PDE (approximately 1.2 times).

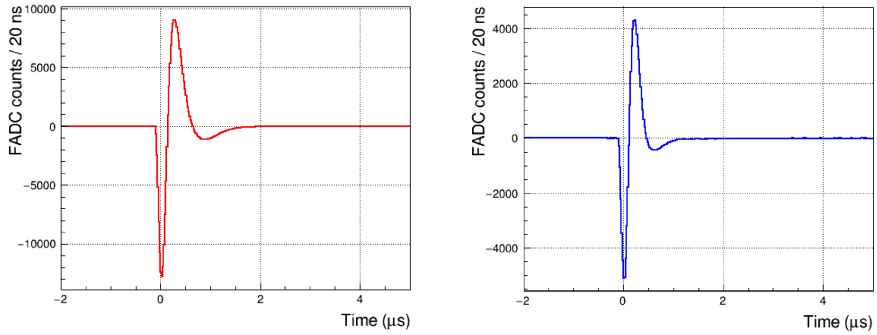

Fig. 5.12. Average Waveforms of electrical crosstalk to other readout PCB. left panel: from 75U MPPCs to 50U channels. right panel: from 50U MPPCs to 75U channels.

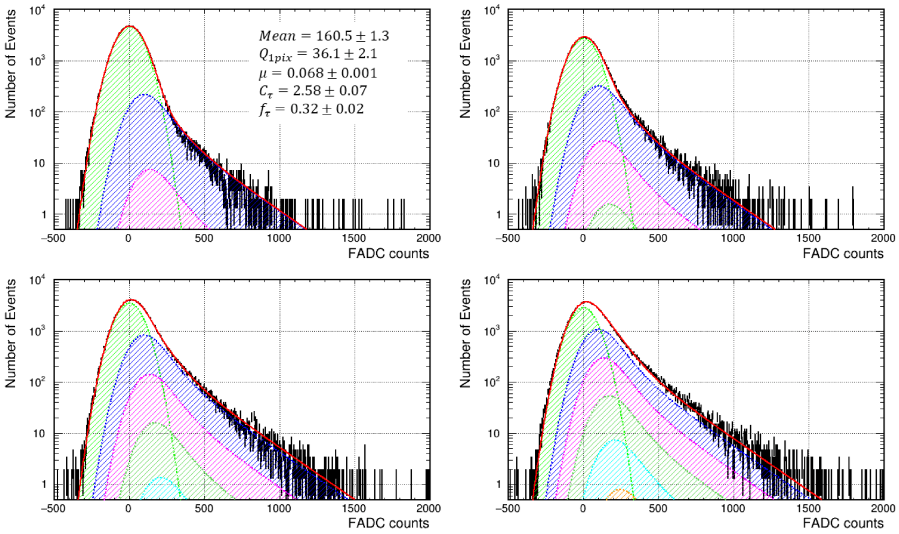

Fig. 5.13. Charge distribution of reduced laser data and fitting result.

Additionally, 75U exhibits higher optical crosstalk and after-pulse probability compared to 50U.

As described above, we should consider the undershoot and electrically crosstalk effect, to explain the signal waveform and estimate light collection efficiency obtained by the ^{241}Am γ-ray. The 16-channel sums of the waveforms, divided by fitting result of $Mean$ in section 5.3.3 for the 75U PCB (F_{75U}) and the 50U PCB (F_{50U}) per channel, are modeled by the numerical convolution of the liquid argon scintillation time distribution and the detector response function:

$$F_{75U}(t) = C_{75U} \times \sum_{t_i=0}^{8\ \mu s} [L_{Ar}(t-t_i) \times T_{75U}(t_i)], \tag{5.15}$$

$$F_{50U}(t) = C_{50U} \times \sum_{t_i=0}^{8\ \mu s} [L_{Ar}(t-t_i) \times T_{50U}(t_i)]. \tag{5.16}$$

$T_{75U}(t_i)$ and $T_{50U}(t_i)$ are the response functions (histograms with a bin width of 20 ns) acquired by the

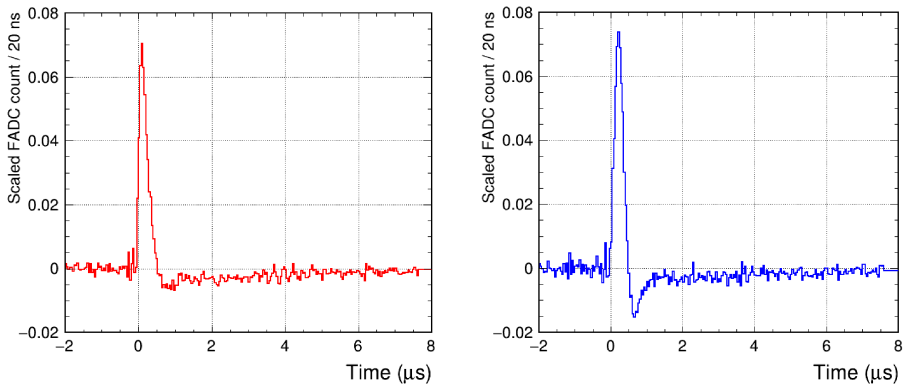

Fig. 5.14. Response function relative to one photon of reduced laser data detected by TSV–MPPC arrays (left: 75U, right: 50U).

laser calibration shown in Fig. 5.14, C_{75U} and C_{50U} are the scale factors indicating the number of photons of the ^{241}Am data, and L_{Ar} is the liquid argon scintillation time distribution:

$$L_{Ar}(t;\tau_f,\tau_s,f_s) = \frac{1-f_s}{\tau_f}\times e^{-t/\tau_f} + \frac{f_s}{\tau_s}\times e^{-t/\tau_s}. \tag{5.17}$$

Here, τ_f = 7 ns and τ_s = 1.6 μs are the time constants for the singlet and triplet components, respectively, and f_s is the fraction of the triplet component. The waveforms for the 75U and 50U PCBs of the ^{241}Am data were simultaneously fitted to the model functions event by event to determine C_{75U}, C_{50U}, and f_s. Fig. 5.16 shows the waveforms of a typical event around the 59.5 keV γ-ray peak (black line, left: 75U, right: 50U) and the results of the fit (red line).

Fig. 5.17 shows the distribution of C_{75U} (red) C_{50U} (blue),and $C_{75U}+C_{50U}$ (black), corresponding to the number of detected photons, in left panel, as well as f_s in right panel. Additionally, the green line in the right panel depicts the distribution of Slow/Total at 59.5 keV obtained from the detector with PMTs (described in Chapter 4). Slow/Total is defined as follows:

$$Slow/Total = L_{slow}/L_{total}, \tag{5.18}$$

where L_{total} is the total integrated charge of the liquid argon signal over the range [−20 ns, +7 μs], and L_{slow} is the integrated charge after 120 ns. There was no observed improvement in the PSD power of the detector with TSV–MPPCs compared to PMTs due to large electrical crosstalk. However, f_s (0.702 ± 0.002) is consistent with the triplet component fraction of the liquid argon scintillation (approximately 0.7 [86]). The red line in the left panel of Fig. 5.17 shows fitting result with the Gaussian function. As a result, the mean value of the light collection efficiency is calculated as 1368.0/59.5 = 23.0 photon/keVee. Considering the large uncertainty of 20% of the template normalization described in section 5.3.2, we determine the light collection efficiency as 23.0 ± 4.6 photon/keVee. It is roughly consistent with the expected light collection efficiency of 41 photons/keV × (50 − 60%) = 20 − 25 p.e./keV.

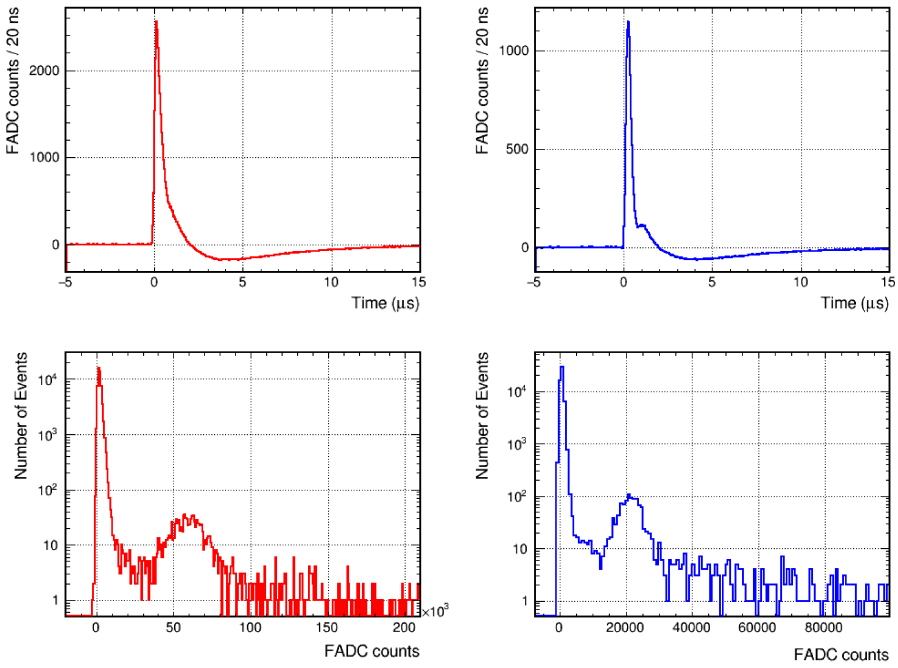

Fig. 5.15. Average waveforms around ^{241}Am γ-ray peak (top left: 75U, top right: 50U). Charge distribution of ^{241}Am (bottom left: 75U,bottom right: 50U).

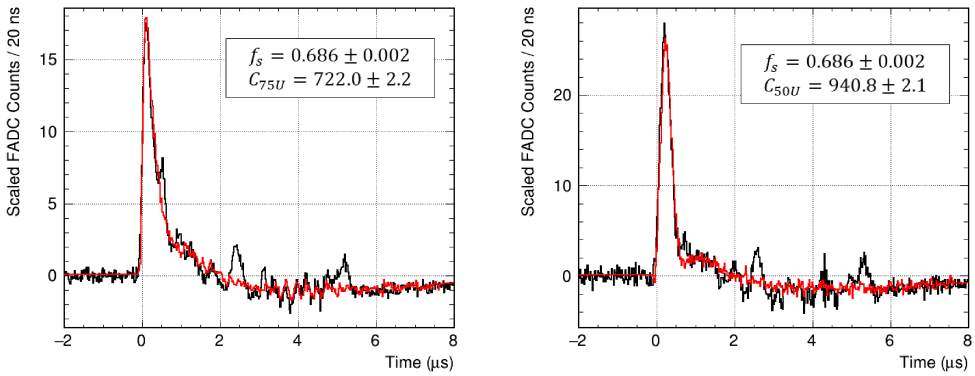

Fig. 5.16. (black line) Waveform of the event around the 59.5 keV γ-ray peak (left: 75U, right: 50U). (red line) Template fitting results.

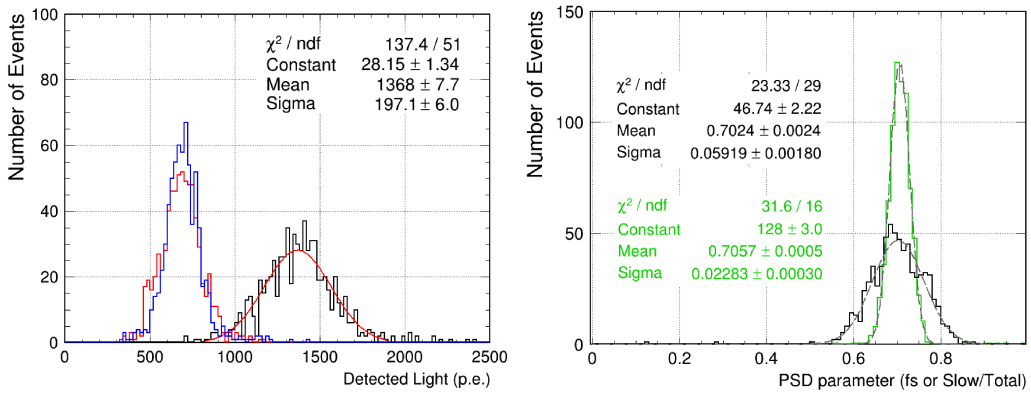

Fig. 5.17. (Left) Distribution of the number of detected photons. The red and blue histograms represent distributions obtained with TSV-MPPCs with 75U and 50U, respectively. The black histogram represents the distribution of the sum of 75U and 50U, along with its Gaussian fitting (red line). (Right) Distribution of the PSD parameters. The black histogram represents parameter f_s obtained with TSV–MPPCs, while the green histogram represents Slow/Total obtained with PMTs. The gray and green lines represent Gaussian fitting for f_s and Slow/Total, respectively.

CHAPTER 6

Measurement of gaseous argon electroluminescence in visible light region

Recent measurements have revealed the presence of visible light components in argon gas electroluminescence. This chapter presents an investigation of gaseous argon electroluminescence in the visible region ranging from 300 to 600 nm at room temperature and normal pressure, utilizing a gaseous TPC. The secondary emission light from the TPC luminescence region was dispersed using a spectrometer. The observed spectrum is interpreted using both the ordinary EL and the newly proposed mechanism of NBrS. Additionally, the impact of nitrogen impurities is discussed in this context.

6.1 Motivation

In a liquid argon double-phase TPC, the ionized electrons drifting upwards are extracted from the liquid to the gaseous phases under a high electric field (few kV/cm). Subsequently, these ionized electrons emit proportional electroluminescence (EL) through scattering on the gaseous argon atoms. Figure 6.1 presents a simplified diagram of the electroluminescence mechanism in gaseous argon, describing three emission processes for pure gaseous argon ordinary EL and nitrogen impurity luminescence, and NBrS as discussed in Section 2.4.1. Because visible light photons are easier to detect using photosensors than VUV photons, the use of visible light components in particle detectors has been actively discussed [87, 88], and a detailed understanding of the wavelength spectrum is crucial for such applications.

Figure 6.2 shows the results of theoretical calculations depicting the EL emission yields as a function of a reduced electric field (E/N) at room temperature (300 K) for both the ordinary EL model (top) [89] and the NBrS model (middle) [61]. Notably, while ordinary EL lights emit only above the 4-Td threshold, NBrS light exhibits emission both above and below this threshold. The bottom plot of Figure 6.2 displays the theoretical calculations for the wavelength spectra of NBrS light [61], presenting a continuous distribution from 200 to 1,000 nm, which is different from that of ordinary EL light.

It is known that more than 1 ppm of nitrogen impurity in liquid argon degrades the argon scintillation light. Thus, the nitrogen impurity level within the liquid phase is usually controlled below 1 ppm for liquid argon double-phase detectors. However, the nitrogen impurity in the gas phase can be higher due to the lower boiling point of nitrogen (77 K) compared to that of argon (87 K). Consequently, nitrogen impurities tend to accumulate in the gas phase over time. Therefore, the effect of nitrogen impurities should be carefully considered in order to understand the VL components.

In this study, detailed measurements of the wavelength spectrum of gaseous argon EL in the VL region

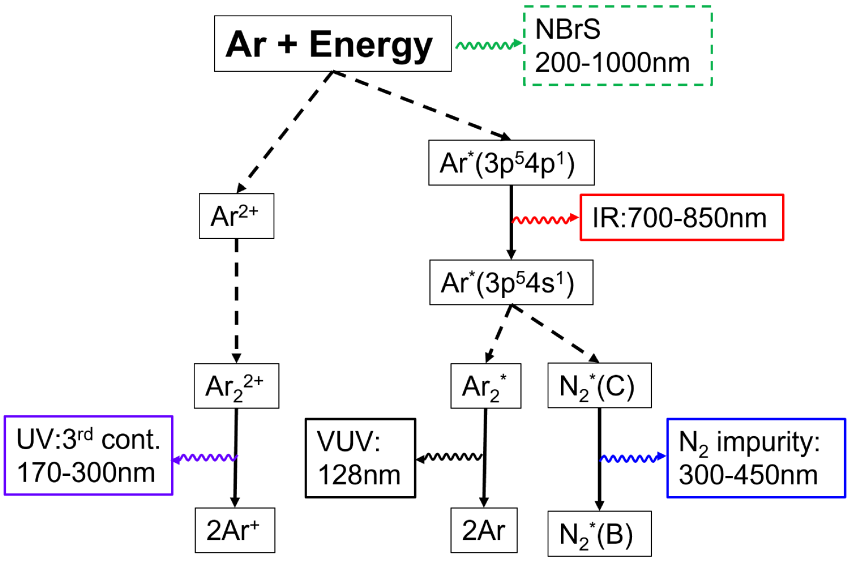

Fig. 6.1. Simplified diagram of the electroluminescence (EL) mechanism of the Ar-N mixture gas.

(300–600 nm) were performed under electric fields up to E/N = 10 Td at room temperature (300 K) and normal pressure (1 bar) utilizing a spectrometer. Then, the spectra derived from ordinary EL, NBrS and nitrogen impurity are interpreted. Note that these emission processes are characterized as functions of a reduced electric field E/N, which exhibits weak associations with temperature and pressure at constant E/N. Therefore, the results of the measurement at room temperature and normal pressure are applicable to the liquid argon temperature (87 K) for the same E/N. The parameter E/N is defined as the electric field per molecular density of the argon gas, and the molecular density is inversely proportional to the temperature. The relationship between E/N at temperatures T_1 and T_2 is expressed as $(E/N)T_1/(E/N)T_2 = T_2/T_1$ with the same electric field and pressure. Thus, 1 Td at 87 K is equivalent to 3.4 Td at 300 K under the same pressure and electric field conditions.

6.2 Experimental apparatus

Figure 6.3 illustrates a schematic of the experimental apparatus of a gaseous argon TPC featuring a fiducial volume with a length of 130 mm and diameter of 64 mm. The TPC was constructed utilizing polytetrafluoroethylene (PTFE) and copper field shaping rings. Pure argon luminescence was measured without the use of a wavelength shifter. The grid was positioned 10 mm away from the anode, after which the anode and cathode were used to generate luminescence and drift fields, respectively. The anode was transparent indium-tin-oxide (ITO)-coated quartz, exhibiting a transmittance of more than 95% for VL with wavelengths greater than 300 nm. An α-ray source (^{241}Am, 300 Bq) was situated inside the TPC to generate signals.

The TPC was placed within a vacuum vessel equipped with a quartz viewport. A spectrometer (Shimadzu Corporation SPG-120S) was positioned outside the vessel near the viewport, within 2 mm slits attached to both the inlet and outlet of the spectrometer. The distance between the anode and the outlet slit was

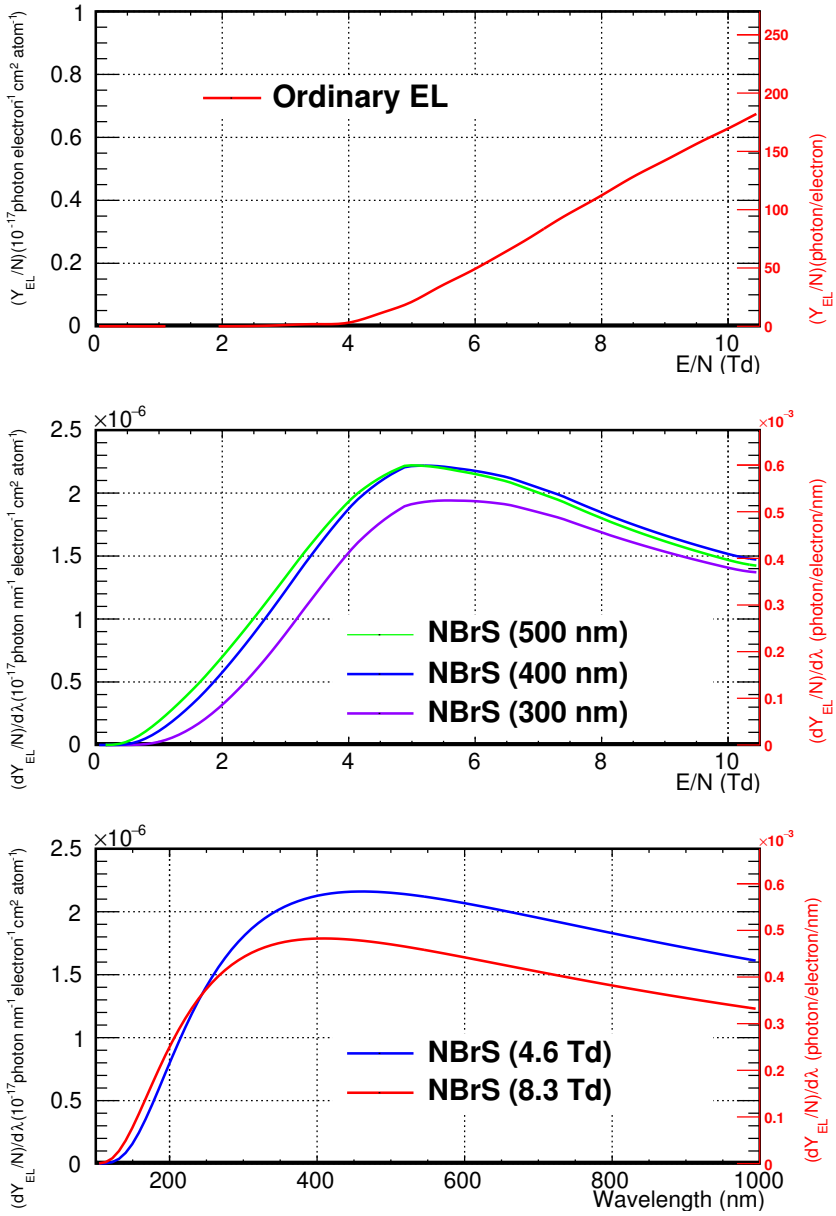

Fig. 6.2. Theoretical emission light yield as a function of reduced electric field E/N for the ordinary electroluminescence (EL) model (top) and the neutral bremsstrahlung (NBrS) model (middle). Emission light yield as a function of wavelength for the NBrS model (bottom). The axis labels on the right shown represented by red characters represent the light yield at room temperature (300 K), normal pressure (1 bar), and an electron drift distance of 1 cm.

approximately 250 mm. The responses of the spectrometer to monochromatic laser light with wavelengths of 450 nm (left) and 520 nm (right) are show in Figure 6.4. These responses were approximated by triangular functions $T(\lambda)$ centered around the peak wavelength λ_{peak}:

$$T(\lambda) = \begin{cases} A\left[1 - \frac{|\lambda - \lambda_{peak}|}{w}\right] & (|\lambda - \lambda_{peak}| < w) \\ 0 & (|\lambda - \lambda_{peak}| > w) \end{cases}, \tag{6.1}$$

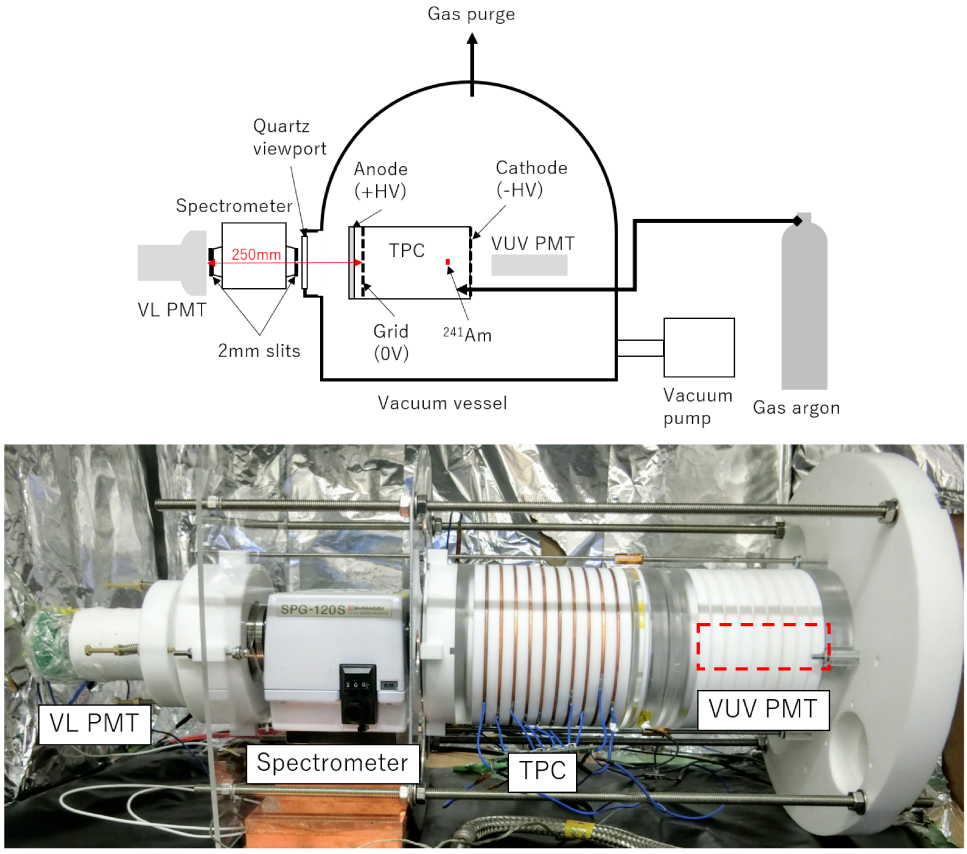

Fig. 6.3. Schematic of the experimental setup (top). Picture of the TPC, spectrometer, and VL and VUV PMT (bottom).

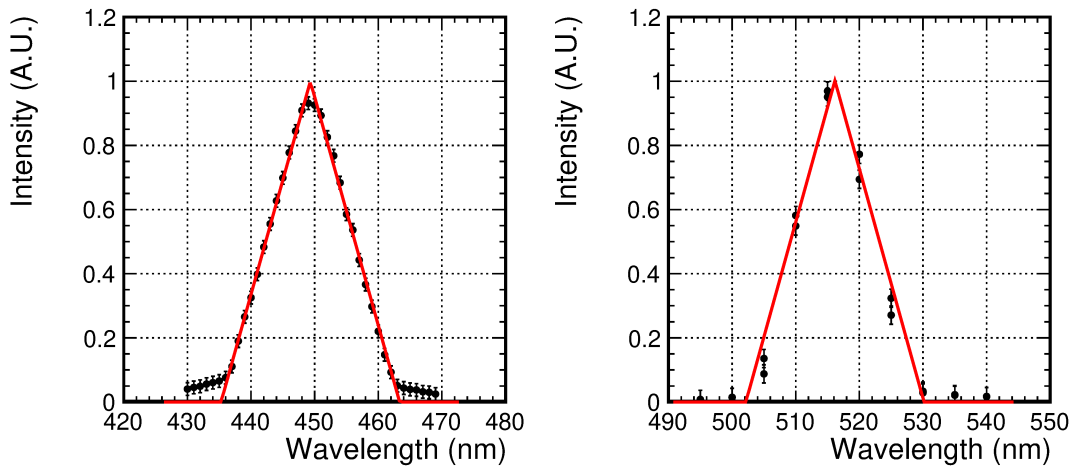

Fig. 6.4. Wavelength responses of the spectrometer for the 450 (left) and 520 nm lasers (right). Data are fitted to triangular functions (red lines).

where the width of the function is denoted as w = 14 nm, and the peak's height is represented by A = 1. A 5 nm shift in the responses was observed, arising from the combined performance of the spectrometer

and input laser. This shift introduced systematic uncertainties in the measurements.

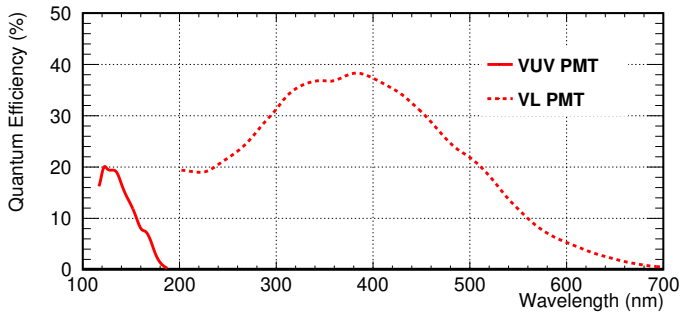

Fig. 6.5. Quantum efficiencies of the two PMTs (VUV PMT and VL PMT) used in this measurement as a function of the wavelength.

Two PMTs with distinct wavelength sensitivities were positioned near the spectrometer and cathode. The PMT located near the spectrometer (Hamamatsu-R11065, referred to as "VL PMT" in this study) with a quartz window exhibited sensitivity to both UV and VL. In contrast, the PMT situated near the cathode (Hamamatsu-R6835, referred to as "VUV PMT") with a MgF_2 window was exclusively sensitive to VUV (Fig. 6.5). A flash analog-to-digital converter (ADC; Struck Innovative Systeme SIS3316-250-14) with a sampling rate of 250 Ms/s and a resolution of 14 bits was utilized to read the PMT signals.

The vacuum vessel was evacuated to 10^{-2} Pa using a molecular turbo pump for at least one day preceding each measurement. Following this, the detector was filled with gaseous argon at room temperature and normal pressure. Throughout the experiment, a constant gas flow rate of 10 L/min was maintained to prevent impurities from outgassing. Three gas mixtures of argon and nitrogen (G1, N10, and N100) were employed in this measurement to assess the impact of nitrogen impurities. The specifications of these gases are detailed in Table 6.1.

Table 6.1. Specification of Ar gases used in the measurements.

Gas type	N_2 composition	Other impurities
G1	< 0.3 ppm	< 0.1 ppm
N10	10±1 ppm	< 0.1 ppm
N100	100±10 ppm	< 0.1 ppm

This study utilized three distinct datasets:

- Data for wavelength spectrum
  High-purity G1 gas was employed to obtain these data. The spectrometer wavelength was systematically scanned from 240 to 660 nm with a 20 nm pitch at two luminescence fields of 4.6 and 8.3 Td. The selection of these E/N values were selected to match the measurements and theoretical calculations presented in Ref.[61].

- Data for electric field dependence
  High-purity G1 gas was used for acquiring these data. The luminescence field was scanned from 1 to 8 Td with 1-Td pitch at wavelengths of 300, 400, and 500 nm. Additional data for the 300 nm wavelength were obtained at 10 Td.

- Data for nitrogen effect
  N10 and N100 gases were utilized to obtain these data. The spectrometer wavelength was systematically scanned from 240 to 660 nm with a 20-nm pitch at a luminescence field of 8.3 Td. For the N100 gas, the spectrometer wavelength was scanned from 300 to 450 nm with a 2.5-nm pitch. Six additional wavelength datasets (316, 337, 358, 381, 406, and 434 nm) corresponding to the resonant wavelength of nitrogen emission were obtained for the G1 and N10 gases [59].

Note that 1 Td of the reduced electric field within the luminescence region (under conditions of room temperature, normal pressure, and a 1 cm luminescence region) corresponds to 245 V/cm.

6.3 Results

The interaction between the α-ray and gaseous argon atoms generated the primary scintillation light (S1) and ionized electrons. The typical flight length of the α-ray was 3 cm. Subsequently, the ionized electrons drifted towards the grid under a constant drift field of 100 V/cm (0.4 Td). In the 1 cm gap between the grid and the anode, these electrons emitted secondary electroluminescence lights (S2) under a luminescence field ranging from 1 to 10 Td.

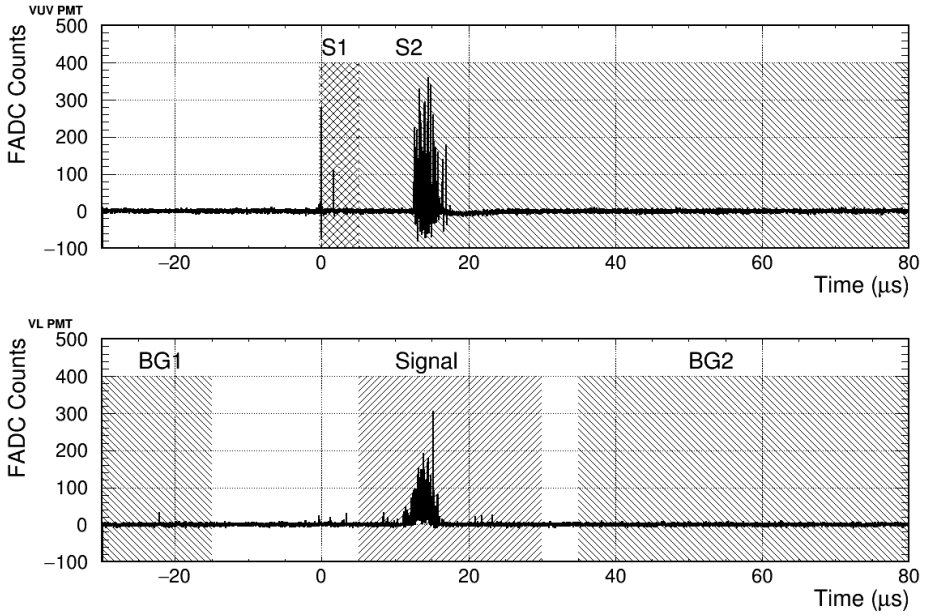

Fig. 6.6. Typical waveform distributions of the VUV PMT (top) and VL PMT (bottom) for the setup without a spectrometer.

The typical waveform distributions recorded by the Flash ADC are depicted in Fig. 6.6. The top and bottom plots represent the signals from VUV PMT and VL PMT, respectively. These distributions were acquired without the use of a spectrometer. The actual light yield of the VL PMT with a spectrometer was less than one photoelectron. The sharp peak in the VUV PMT at t = 0 corresponds to the S1 signal, while the broader peak around t = 15 µs corresponds to the S2 signal.

Table 6.2. Definition of light yield variables.

Name	PMT	Interval of integration
S1	VUV PMT	[−0.4 µs, 5 µs]
S2	VUV PMT	[5 µs, 80 µs]
Signal	VL PMT	[5 µs, 30 µs]
BG1	VL PMT	[−30 µs, −15 µs]
BG2	VL PMT	[35 µs, 80 µs]

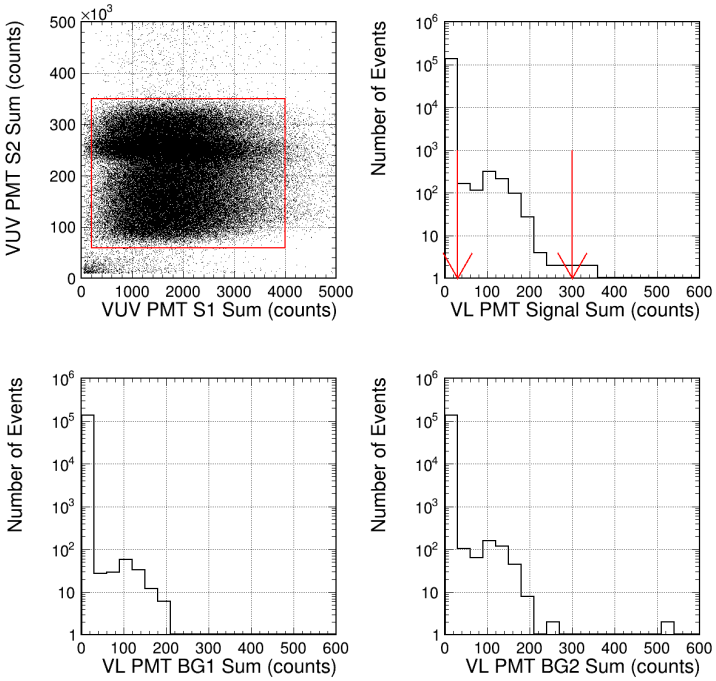

Fig. 6.7. Integrated light yield distributions of the VUV PMT waveform in the S1 and S2 regions (top-left). Data for the plot are obtained at a spectrometer wavelength of 400 nm and a luminescence field of 8.3 Td using the G1 gas. Events in the red box are selected for the wavelength spectrum calculation. The integrated light yield distribution of the VL PMT waveform is in the Signal (top right), BG1 (bottom left), and BG2 (bottom right) regions.

Five light yields (S1, S2, Signal, BG1, and BG2) were computed by integrating the waveform distributions of the VUV and VL PMT, as presented in Table 6.2. The integration intervals are highlighted by the hatched regions in Fig. 6.6. Events were selected based on S1 and S2 in the red box in the top-left

plot of Fig. 6.7. The data for this plot were acquired at a spectrometer wavelength of 400 nm and a luminescence field of 8.3 Td using G1 gas, resulting in the selection of 137,684 events (denoted as N_0). The distributions of Signal, BG1, and BG2 for the selected events are shown in the top-right, bottom-left, and bottom-right plots of Fig. 6.7, respectively. As mentioned earlier, most of the time, no photons were observed, and the peaks around 100 counts corresponded to single PE events. The VL PMT was operated with gain for single PE events of approximately 130 counts, and the PMT exhibited a clear separation between the noise level and the single PE events [90]. The single PE events were selected based on the light yields within the range of 30–300 counts, resulting in N_{Signal} = 943, N_{BG1} = 166, and N_{BG2}=502 for Signal, BG1, and BG2, respectively. The signal region contained background events primarily due to the accidental coincidence of the PMT dark counts. Background contamination was estimated using BG1 and BG2 normalized to the window width: $N_{Background}$ = (25 µs/60 µs) × (N_{BG1} + N_{BG2}) = 278. The number of events after background subtraction was $N_{Signal} - N_{Background}$ = 665. Assuming that the light yield followed a Poisson distribution, the light yield in the unit of PEs equaled the fraction of events in the single PE peak: $(N_{Signal} - N_{Background})/N_0$ = 0.00483.

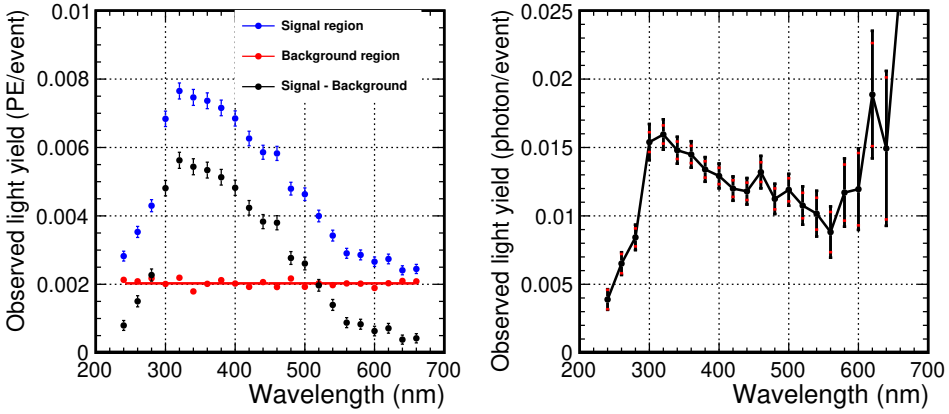

Fig. 6.8. Wavelength spectra for G1 gas at a luminescence field of 8.3 Td. Left: Observed light yields in the unit of photoelectrons as a function of the wavelength in the Signal region (blue points), BG1 + BG2 region (red points), and background-subtracted signal (black points). Right: Wavelength spectrum after correcting for PMT quantum efficiency.

By repeating the same analysis steps for various configurations (spectrometer wavelength, luminescence field, and gas type), the desired spectrum was obtained. The left plot in Fig. 6.8 shows the resulting wavelength spectra utilizing G1 gas at a luminescence field of 8.3 Td. The blue, red, and black points denote the light yields in the signal, background, and signal–background region, respectively. Since the light yield in the background region remained consistently constant, the average value (red line) was employed for subtraction. Finally, the wavelength spectrum (right plot in Fig. 6.8) was acquired after correcting for the VL PMT quantum efficiency as shown in Fig. 6.5). Two sources of systematic uncertainties were taken into account for the observed light yield.

- PMT quantum efficiency.

As discussed in the previous section, the wavelength of light, subsequent to its passage through the spectrometer, followed the distribution described by Eq. 6.1. In addition, a systematic wavelength shift of ±5 nm was observed for the spectrometer. Therefore, the determination of the wavelength for computing the quantum efficiency of the VL PMT becomes uncertain. The difference in quantum efficiency, corresponding to a wavelength change of ±7 nm, was assigned as the systematic uncertainty of the observed light yield.

- Reproducibility of measurement
  The stability of measurement throughout the data-acquisition period was assessed by repeating the measurement. A relative uncertainty of 5% was allocated to the observed light yield.

The red inner error bars in the right plot of Fig 6.8 depict the statistical uncertainty, while the outer error bars with black color represent the total uncertainty ($\sqrt{\text{statistical}^2 + \text{systematic}^2}$).

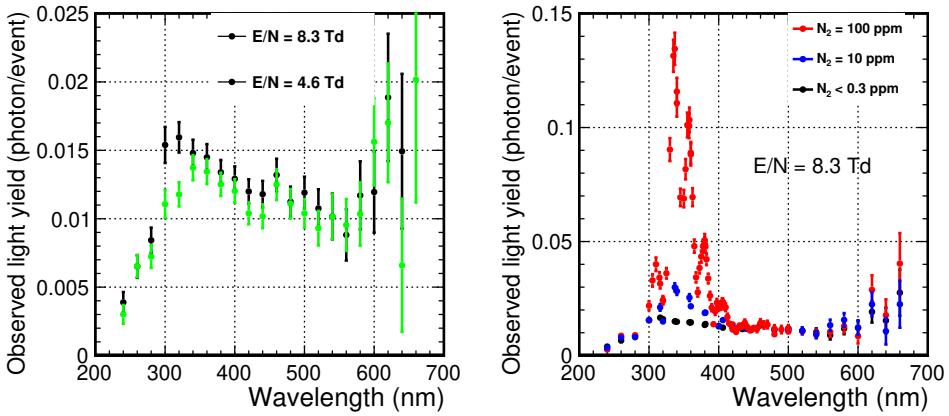

Fig. 6.9. Wavelength spectra after correcting the PMT quantum efficiency. Left: Spectra for high-purity GAr with electric fields of 4.6 Td (green points) and 8.3 Td (black points). Right: Spectra for GAr with N concentrations of less than 0.3 ppm (black points), 10 ppm (blue points), and 100 ppm (red points).

The obtained wavelength spectra are displayed in Fig. 6.9. The left plot shows the spectra for the G1 gas with electric fields of 4.6 Td (green points) and 8.3 Td (black points). The right plot displays the spectra for the G1 gas (black points), N10 gas (blue points), and N100 gas (red points) at E/N = 8.3 Td. The transmittance of the ITO-quartz degraded for the wavelength below 300 nm, and background contributions from the secondary light of the spectrometer were observed for the wavelength above 600 nm (300 nm×2). Therefore, a wavelength range of 300–600 nm was utilized for the subsequent analysis.

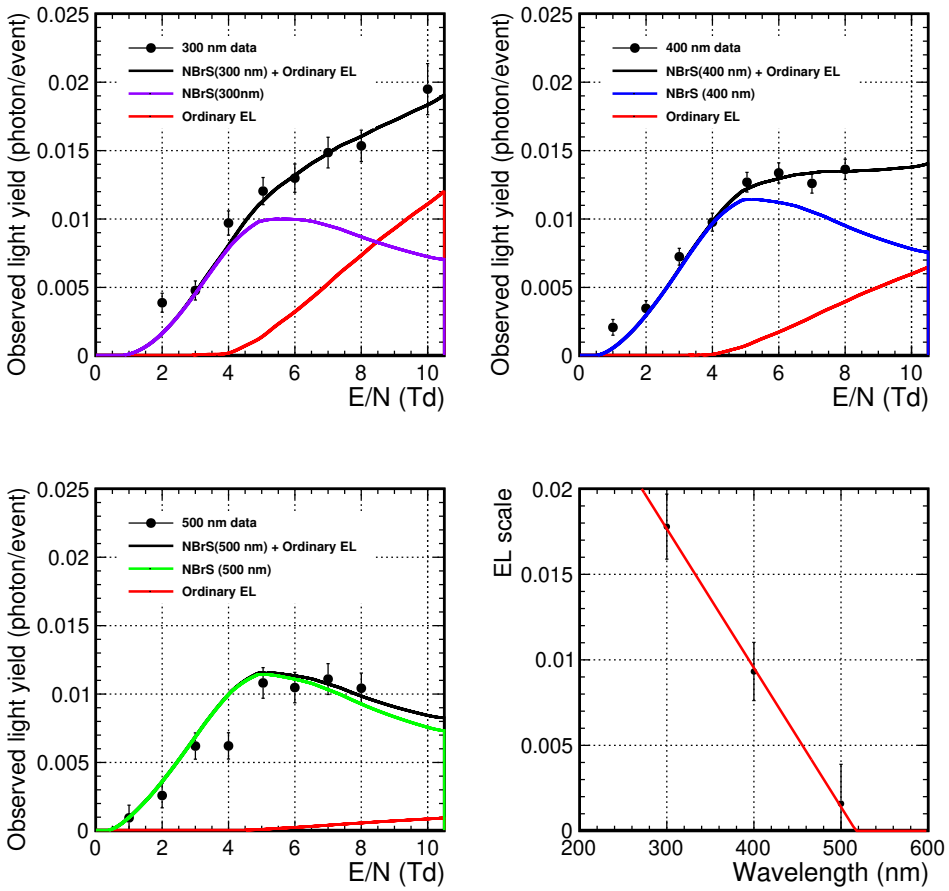

Fig. 6.10. Observed light yield as a function of E/N at wavelengths of 300 (top left), 400 (top right), and 500 nm (bottom left). The three distributions are simultaneously fitted to the sum of the model functions (black) of NBrS (purple, blue, and green) and ordinary EL (red). The bottom-right plot shows the scale factors for the ordinary EL as a function of wavelength.

6.4 Discussion

6.4.1 Electric field dependence

Figure 6.10 shows the results of the electric field dependence data at three wavelengths, with each nominal wavelength exhibiting an interval of approximately 14 nm (width w of the spectrometer in Eq (6.1)). Light emissions were observed at low electric fields below 4 Td. The light yields appeared saturated at higher electric fields. Therefore, the ordinary EL model is not enough to explain these distributions. To quantitatively assess the contribution of the NBrS model, the data points were simultaneously fitted to the following function:

$$F_{\mathrm{Ar}}(\lambda, E/N) = S_{\mathrm{EL}}(\lambda) F_{\mathrm{EL}}(E/N) + S_{\mathrm{NBrS}} F_{\mathrm{NBrS}}(\lambda, E/N), \tag{6.2}$$

where, $F_{\mathrm{EL}}(E/N)$ and $F_{\mathrm{NBrS}}(\lambda, E/N)$ represent the light yield functions for the ordinary EL and NBrS models as shown in Fig. 6.2, respectively. The scale factors, $S_{\mathrm{EL}}(\lambda)$ and S_{NBrS}, were determined by the fit.

Table 6.3. Scale factors obtained by fitting the data points to the electric field dependence of the observed light yield distribution.

Fit parameter	Value
χ^2/ndf	41.9/25
S_{NBrS}	$(5.1 \pm 0.2) \times 10^3$
S_{EL}(300 nm)	$(1.81 \pm 0.22) \times 10^{-2}$
S_{EL}(400 nm)	$(0.97 \pm 0.22) \times 10^{-2}$
S_{EL}(500 nm)	$(0.19 \pm 0.25) \times 10^{-2}$
S_0	$-(8.1 \pm 1.5) \times 10^{-5}$
λ_0	(521 ± 31)

The results of the fit are summarized in Table 6.3, and the fitted functions are presentd in Figure 6.10. The χ^2/ndf of the fit was 41.9/25, which is marginally worse because two data points (300 nm with 2 Td and 500 nm with 4 Td) were significantly different from those of the fitted function. Note that the result did not change significantly, even after excluding these two points from the fit. The bottom-right plot in Figure 6.10 depicts S_{EL} as a function of wavelength. The scale factor at 300 nm was the largest because of the significant UV contribution from the third continuum emission in Eq. (2.28). However, the scale factor at 500 nm was consistent with zero within its uncertainty. While the spectrum of the ordinary EL emission is not entirely understood, the wavelength dependence of the scale factors approximately follows a straight line,

$$S_{EL}(\lambda) = \begin{cases} S_0(\lambda - \lambda_0) & (\lambda < \lambda_0) \\ 0 & (\lambda > \lambda_0) \end{cases} . \tag{6.3}$$

The parameters S_0 and λ_0 were determined by fitting the data, as presented in Table 6.3.

6.4.2 Emission light yield of the NBrS model

In Figure 6.2, the theoretical prediction for the emission light yield of NBrS, denoted as F_{NBrS}, is 2.2×10^{-6} (10^{-17}photon/electron/cm^2/atom) for an E/N of 4.6 Td and a wavelength of 500 nm. The expected number of photons emitted by the NBrS mechanism (N_γ^{emit}) for this experimental setup, involving ^{241}Am α-ray and a spectrometer, was computed using F_{NBrS} as follows:

$$N_\gamma^{emit} = N_e \times \rho \times d \times w \times F_{\mathrm{NBrS}} = 1.7 \times 10^3, \tag{6.4}$$

where $N_e = E_\alpha/W_i$ = 5.49 MeV/26.4 eV = 2.1×10^5 [91] represents the number of drift electrons, $\rho = 2.7 \times 10^{19}$ atom/cm^3 is the number density of the argon atom, d = 1 cm is the distance of the luminescence field, and w =14 nm denotes the width of the spectrometer response in Eq. (6.1). In contrast, in Figure 6.9, the observed number of photons $N_\gamma^{obs} = 1.1 \times 10^{-2}$ for E/N = 4.6 Td and

wavelength = 500 nm. Therefore, the overall photon detection efficiency was calculated as follows:

$$\epsilon = N_{\gamma}^{obs}/N_{\gamma}^{emit} = 1.1 \times 10^{-2}/1.6 \times 10^{3} = 6.5 \times 10^{-6}. \tag{6.5}$$

The efficiency was predominantly attributed to the geometrical acceptance (A_{geo}), calculated using the distance from the luminescence region to the outlet slit (25 cm), and the size of the slit (2 mm×5 mm).

$$A_{\mathrm{geo}} = \frac{2\ \mathrm{mm} \times 5\ \mathrm{mm}}{4\pi \times (25\ \mathrm{cm})^2} = 1.3 \times 10^{-5}. \tag{6.6}$$

A_{geo} is two times larger than ϵ, which can be approximately explained by the transmittance of the quartz viewport and the ITO quartz (approximately 95% each), and the efficiency of the spectrometer (>50% [92]). Thus, the absolute value of the observed light yield in this measurement was roughly consistent with the prediction of the NBrS model.

6.4.3 Wavelength spectrum

Because the scale factors for the ordinary EL model (S_{EL}) and the NBrS model (S_{NBrS}) help predict all wavelengths mentioned in the previous section, the model function of Eq. (6.2) explains the wavelength spectrum. Figure 6.11 depicts an overlay of the model functions to the wavelength spectrum data at the reduced electric fields of 8.3 Td (top) and 4.6 Td (bottom). The χ^2/ndf values between the data points and the model functions were 16.4/16 and 32.0/16 for the 8.3 and 4.6 Td data, respectively. The spectrum data and model functions were in good agreement, except for two data points (340 and 360 nm with 4.6 Td). In this analysis, the spectrum for ordinary EL emission was modeled using a straight line (Eq. (6.3)). However, the spectrum of G1 gas with 8.3 Td (Fig. 6.9) showed a significant discontinuity below 300 nm, which points to the existence of a resonant-type structure for the ordinary EL emission. A finer-wavelength scan with more statistics will be required for a detailed explanation of ordinary EL emission. The spectrum at 4.6 Td was explained by the nearly pure NBrS emission, and the contribution of the EL emission was less than 10%.

6.4.4 Nitrogen effect

As mentioned above, an alternative explanation for the VL component of the EL emission other than the NBrS model is the nitrogen excimer emission. To investigate this effect, an Ar–N gas mixture was employed. The right plot in Figure 6.9 displays a significant excess between 300 and 400 nm in the N100 data attributed to nitrogen. However, the wavelength spectra of N100, N10, and G1 remain consistent above a wavelength of 450 nm. Consequently, we assumed that there were no substantial nitrogen contributions above 450 nm. Figure 6.12 depicts the wavelength spectra from 300 to 450 nm at an electric field of 8.3 Td employed G1 gas (black points), N10 gas (blue points), and N100 gas (red points), respectively. The model curves of NBrS (dotted black line) and NBrS + ordinary EL (solid black line) are overlaid (the same curves as in Fig. 6.11). The N100 gas data exhibited six resonant structures consistent with the measurements reported by Takahashi et al. [59]. The peak wavelengths ($\lambda_{peak,i}$) and

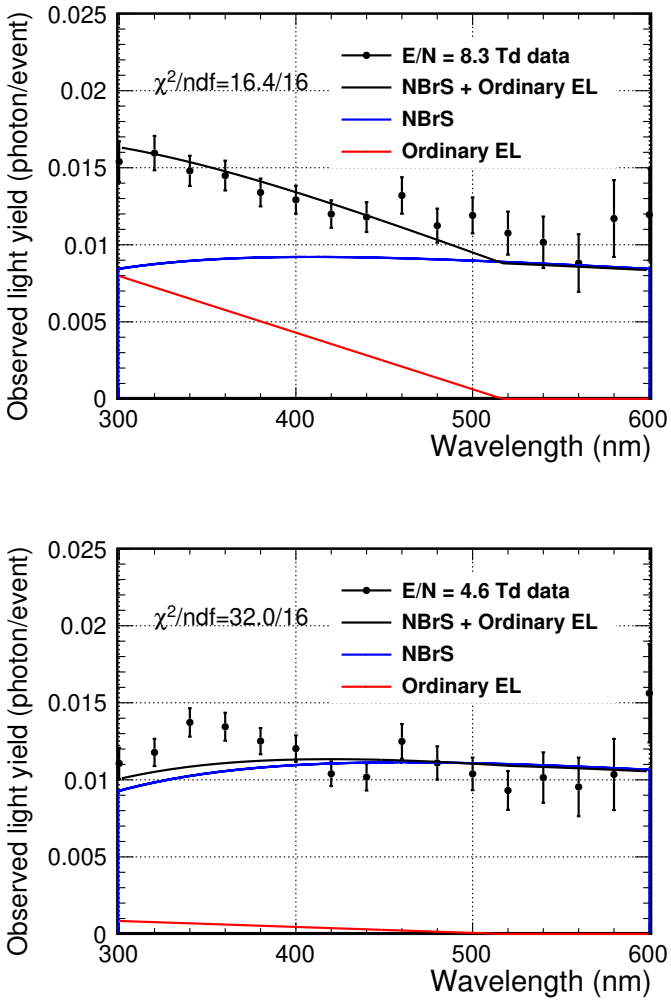

Fig. 6.11. Measured wavelength spectrum for E/N = 8.3 (top) and 4.6 Td (bottom). The spectra for NBrS and ordinary EL are overlaid.

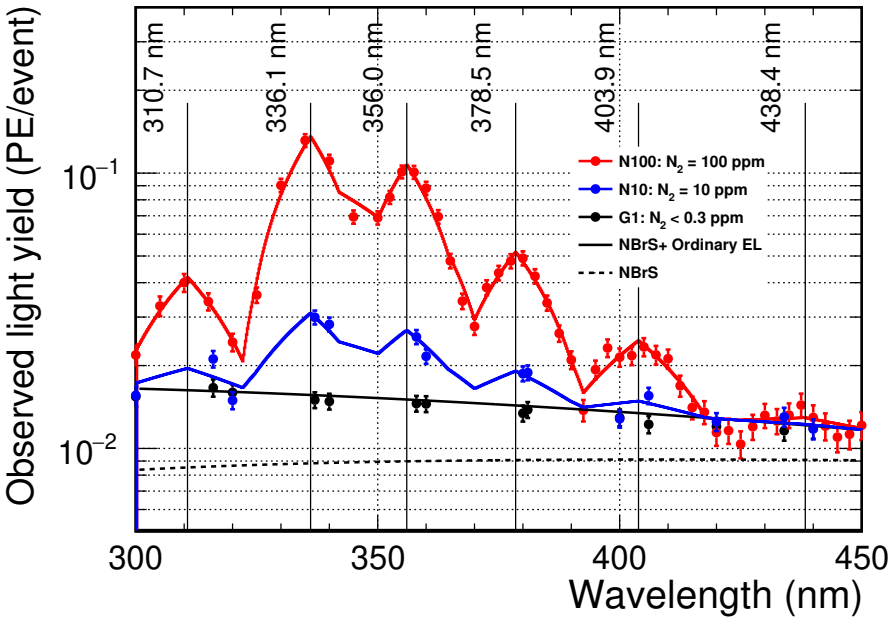

Fig. 6.12. Wavelength spectra for N_2 concentrations of <0.3 ppm (black points), and 10 ppm (blue points), and 100 ppm (red points).

heights (A_i) of the these resonances were determined by fitting the N100 spectra to a model function:

$$F_{\mathrm{N100}}(\lambda) = F_{\mathrm{Ar}}(\lambda) + \sum_{i=1}^{6} T_i(\lambda), \tag{6.7}$$

where F_{Ar} is the model function of Eq. (6.2) (solid black line in Fig 6.12), and the triangular function T_i is

$$T_i(\lambda) = \begin{cases} A_i \left[1 - \frac{|\lambda - \lambda_{peak,i}|}{w}\right] & (|\lambda - \lambda_{peak,i}| < w) \\ 0 & (|\lambda - \lambda_{peak,i}| > w) \end{cases}, \tag{6.8}$$

where the width of the function w is fixed at 14 nm. The fit results are summarized in Table 6.4. As mentioned earlier, a systematic uncertainty of 5 nm was considered for the wavelength, accounting for the shift observed in Fig. 6.4.

The wavelength spectrum obtained with N10 gas was modeled using the following expression:

$$F_{\mathrm{N10}}(\lambda) = F_{\mathrm{Ar}}(\lambda) + \alpha \sum_{i=1}^{6} T_i(\lambda), \tag{6.9}$$

where F_{Ar} and $T_i(\lambda)$ follow the same functions as those in Eqs. (6.7). The scale factor, α, was determined by fitting the data points to the wavelength spectrum. As a result, $\alpha = 0.12 \pm 0.01$ was obtained, which is consistent with the ratio of the nitrogen concentration of N10 (10 ± 1 ppm) to N100 (100 ± 10 ppm),

Table 6.4. Summary of the fit results of six observed emission peaks in the N100 data. The predicted wavelengths for the $N_2^*(C^3\Pi_g) \rightarrow N_2^*(B^3\Pi_g) + h\nu$ transition [59].

	This work		Predicted [59]	
i	$\lambda_{peak,i} \pm_{fit} \pm_{sys}$ (nm)	$A_i \pm_{fit}$ 10^{-2}(A.U.)	V'=0 (nm)	V'=1 (nm)
1	$310.7 \pm 0.6 \pm 5.0$	(2.6 ± 0.2)	N/A	315.9
2	$336.1 \pm 0.2 \pm 5.0$	(12.0 ± 0.4)	337.1	333.9
3	$356.0 \pm 0.1 \pm 5.0$	(9.3 ± 0.2)	357.7	353.7
4	$378.5 \pm 0.1 \pm 5.0$	(3.7 ± 0.4)	380.5	375.5
5	$403.9 \pm 0.5 \pm 5.0$	(1.1 ± 0.2)	405.9	399.8
6	$438.4 \pm 7.1 \pm 5.0$	(0.08 ± 0.07)	434.4	427.0

i.e., 0.1. Additionally, the G1 dataset were fitted to the model function:

$$F_{\mathrm{G1}}(\lambda) = \beta F_{\mathrm{Ar}}(\lambda) + \alpha \sum_{i=1}^{6} T_i(\lambda), \tag{6.10}$$

and the fit result showed that $\alpha = 0.001 \pm 0.007$ and $\beta = 0.96 \pm 0.03$. Thus, the residual nitrogen impurity in the G1 data was 0.1 ± 0.7 ppm, consistent with the uncertainty of 0 ppm. In summary, even small amount of nitrogen impurities (>10 ppm) can lead to VL emission within 300 to 450 nm range. However, the G1 data from this measurement contained nitrogen impurities of less than 1 ppm, along with negligible nitrogen emissions. As shown in Fig. 6.1, the nitrogen emission arises from the transition of Ar^*, necessitating at least 4 Td of the reduced electric field. Hence, nitrogen emissions cannot account for the VL emission below 4 Td. Even if small packets of VL emissions were produced from unknown impurities inside the argon gas, it is highly unlikely that the emissions occurred below 4 Td. Therefore, NBrS emissions stand as the most reasonable model to explain the observed VL emission. Furthermore, it is possible to utilize nitrogen emissions in the gas phase for the double-phase detector if the amount of nitrogen impurities in the liquid phase can be maintained below 1 ppm.

6.5 Summary

The argon EL in the VL region (300 to 600 nm) was investigated utilizing the gaseous argon TPC, with ^{241}Am α-rays as the signal source under room temperature and normal pressure. The secondary emission light from the TPC luminescence region was dispersed using a spectrometer. The wavelength spectrum and luminescence-field dependence of the light yield were compared with those predicted by the ordinary EL and NBrS models. The effect of nitrogen impurities on the light yield was assessed using the argon-nitrogen mixture gas. We conclude that the ordinary EL model and nitrogen emission alone cannot fully explain the wavelength spectrum and electric field dependence of the observed light in the VL region. The inclusion of the NBrS model can enable a comprehensive explanation of the phenomena.

CHAPTER 7

First operation of liquid argon detector at the stratosphere

Scientific balloons are utilized across various fields as airborne platforms with the capability of sustained levitation in the stratosphere for extended periods, often spanning several months. Scientific balloons have been successfully employed in numerous cosmic ray observations. In Japan, JAXA centrally oversees the research, development, and operation of scientific balloons, conducting test flights for cosmic ray observation experiments like GAPS [93] and SMILE [94]. Beyond Japan, for instance, NASA manages long-duration flights at Antarctica such as BESS-Polar [95]. In addition, a balloon experiment with a liquid xenon detector, LXeGRIT, was conducted [96]. The attractiveness of balloon experiments stems from their ability to be conducted at a lower cost and with a shorter preparation time than satellite missions. On the other hands, balloon-borne experiments pose unique challenges such as the need for resistance to vibration and shock.

Despite the numerous advantageous features of liquid argon detectors in cosmic ray observations, as planned by GRAMS [30], they have never been operated on flying objects. We launched a compact and simple liquid argon detector on a balloon as an initial engineering flight for airborne operation. The objective of this engineering flight is to establish the technical procedures for operating the balloon-borne liquid argon detector at high altitudes. This chapter provides detailed information about this ballooning flight.

7.1 Challenges for operation of liquid argon detector at stratosphere

Balloon experiments present unique challenges, including vibration, weight limitations, and dependence on weather conditions. This section lists some of the challenges that are particularly important to consider in the operation of liquid argon detectors.

- **The necessity for resistance to vibration and shock:** Unlike ground-based operations, a detector suspended by a balloon experiences pendulum motion, rotation, and vibrations. In the case of a liquid argon detector, maintaining the liquid surface is challenging, making two-phase detectors impractical. Even with a single-phase detector, a sufficient amount of liquid argon is required to prevent the detector casing from being exposed to the gaseous phase. The entire payload, not just the liquid argon detector, must be able to withstand the significant loads applied during balloon launching and parachuting.

- **Adherence to weight limitation:** The weight that can be levitated contingent on both the size of the balloon and the amount of helium. Generally, lighter payloads facilitate easier launch, enabling smaller balloons to reach higher altitudes.
- **Adherence to electric power limitation:** The availability of electrical power is constrained when operating on a balloon, especially considering the high power consumption of the refrigerator used for cooling argon.
- **Adaptation to atmospheric pressure and temperature changes associated with changes in altitude:** Figure 7.1 illustrates the temperature and pressure of the U.S. Standard Atmosphere as a function of altitude [97]. The entire payload must function effectively regardless of changes from the ground to the upper atmosphere. Additionally, since the atmospheric pressure is below the triple point of argon (0.068 MPa), there is a possibility of argon solidification.
- **The ability for remote operation of the detector:** Control of voltages for PMTs and drift electric fields, as well as adjustments to DAQ settings, are performed remotely via wireless communication from the ground. Measurements such as temperature and pressure are also monitored remotely.
- **The safe recovery of the payload:** After observation, the payload is detached from the balloon and descends softly with a parachute for either a land or water landing. It is essential to minimize damage due to landing and reduce risks when humans approach during recovery. Since transmitting all data to the ground is impractical, the recovery of the data storage media becomes a necessity.

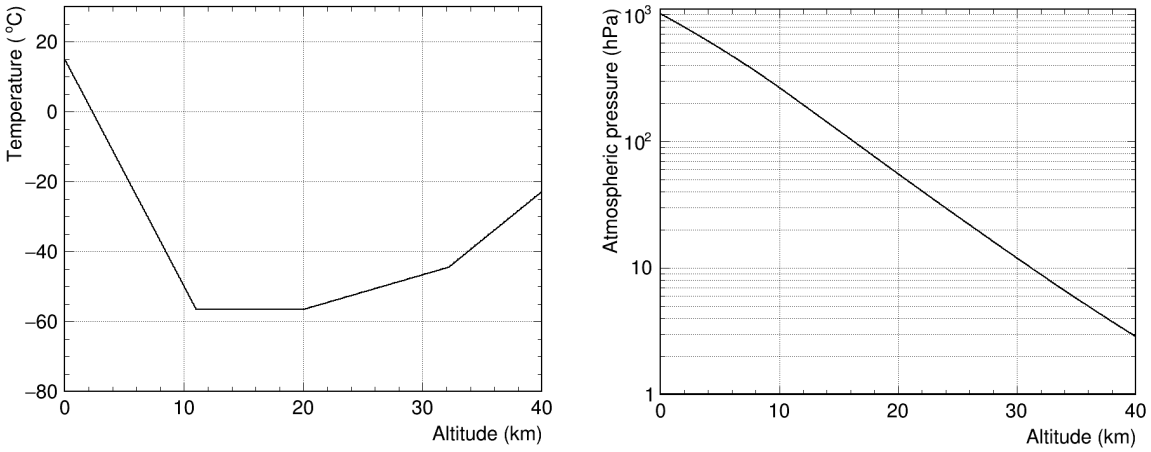

Fig. 7.1. Atmospheric temperature (right figure) and pressure (left figure) in U.S. Standard Atmosphere as a function of altitude. These figures are illustrated based on information from Ref.[97].

7.2 Payload

The payload comprises a stainless steel vacuum-insulated vessel for the liquid argon, a stainless steel pressurized vessel for the CPU and batteries, and a gondola to carry them. The total weight of the payload is 269.5 kg without liquid argon. The gondola was designed to withstand 2G in horizontal (2 axes) and vertical directions for the impact during release and 5G in the vertical direction for the impact during parachuting. Gondola frame consist of L-shaped steel (A6065-t5, $500 \times 500 \times$ t5 mm) and H-shaped steel (A6065-t5, $500 \times 500 \times$ t4 $\times$ t3 mm). The overall size is a cube of $1.2 \times 1.2 \times 1.2$ m. The frames are fastened to each other with stainless screws. Stainless steel eye nuts were used at the suspension points, and extra-strong duralumin (A7075), which is stronger than the frame material, was installed at the eye nut fixing points. The entire gondola is covered with 25 mm or 75 mm heat insulation material (Styrofoam B2) because the outside air temperature drops to at least -70 ^{o}C in the upper air. The gondolas were also colored with orange and white ink to improve visibility. Styrofoam is also laminated inside the gondola as a floating device after landing on the water.

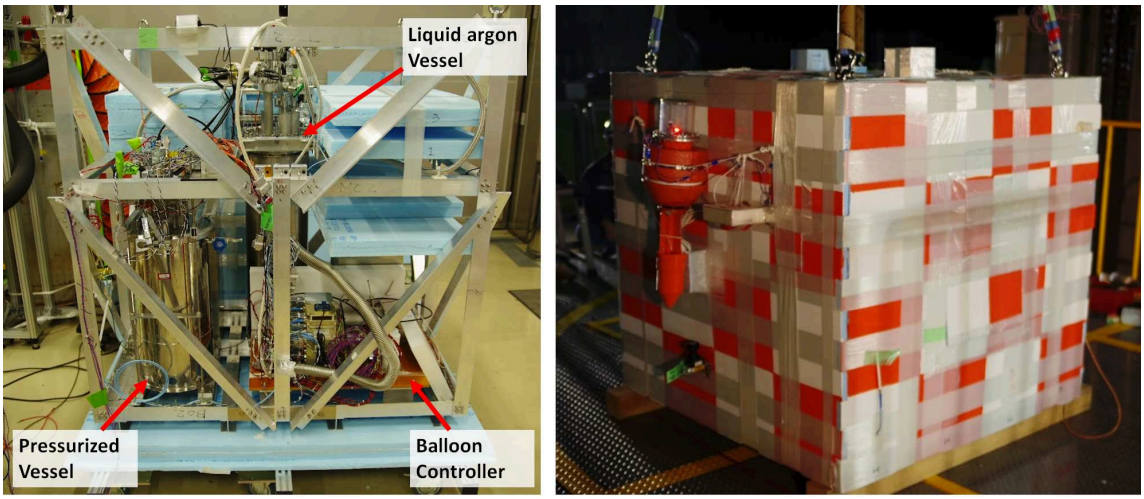

Fig. 7.2. Images of payload.

Figure 7.3 shows a schematic diagram of the liquid argon handling system and a picture of the simple/compact TPC. Liquid argon is held in a stainless steel vacuum-insulated vessel, 80 cm high and 25 cm in diameter. This vessel has a heat inflow rate of less than 10 W at room temperature and can hold enough liquid argon to operate the detector for more than 24 hours. To prevent vessel breakage due to a rise in vessel pressure or coagulation of argon due to a drop in pressure, the vessel pressure is maintained by an absolute pressure valve (VF1) with an operating pressure of 1.1 (in valve-outlet pressure of 1 atm) to 1.2 (in valve-outlet pressure of 0 atm) atm. In the event of a sudden pressure increase, such as when the vessel is overturned, the vessel is evacuated through a differential pressure safety valve (VF3) and a rupture disk (RD) with an operating differential pressure of 2.5 atm and 3.0 atm, respectively. Liquid argon is filled through a handmade filter, which consists of molecular sieve and reduced copper, to remove impurities such as water and oxygen. A sufficient amount of argon is filled the day before launch to allow

for standby time. Liquid argon is drained from the vessel using the differential pressure between the inner pressure of the vessel and the outside atmosphere while in the upper air to avoid the risk of liquid argon boiling during water landing and recovery. Since the piping for liquid drainage extends to the bottom of the vessel, when liquid argon drainage is complete, the inside of the vessel is connected to the atmosphere, and the pressure inside the vessel become equal to the atmospheric pressure. However, above an altitude of 3 km, atmospheric pressure falls below the liquid argon triple point pressure, and argon coagulation is expected at the outlet of the drain piping. Liquid drainage is controlled by a solenoid valve (VF5) at the end of the piping.

Liquid argon TPC consists of three types of PCBs (cathode, side plate, and anode) and gate-grid, and its sensitive area is $10 \times 10 \times 10$ cm. From the bottom to the top, the cathode is positioned at Z=0 cm, the grid at Z=10 cm, the anode at Z=10.5 cm, and the side plate is located on the side of the sensitive area. The electric field is formed in the vertical direction by dividing the cathode, side plate, grid and GND with resistance. During operation, a voltage of 2.5 kV was applied to the cathode, resulting in a drift electric field of 200 V/cm and an induction field of 1 kV/cm. The anode is divided into three segments, as depicted in Fig. 7.8, and the ionized electron signal is amplified and read out by a charge-integrating amplifier for each of the segmented electrodes. The gain and time constant of the charge-integrating amplifier are 2 V/pC and 500 µs, respectively. Liquid argon scintillation is detected by a PMT installed in the lower part of the TPC after wavelength shifting to visible light. PMT and three charge amplifiers signals are digitized using two USB oscilloscopes (Digilent, Analog Discovery 2). Data acquisition is triggered by the PMT signal and stored as waveform data in the onboard flight computer within the pressurized vessel. The trigger rate is limited to approximately 60 Hz due to CPU performance constraints.

Sensors such as thermometers, pressure gauges, and voltmeters were used to monitor the condition of the detectors. These environmental data are transmitted to the ground every few seconds, allowing the detector status to be constantly monitored on the ground. An on-board computer controlled the detector operations such as voltage adjustment and DAQ setting changes, as well as communications to ground. The primary lithium batteries served as the power source, with their power distributed to each component through DC-DC converters.

7.3 Engineering flight campaign

This engineering flight was approved in April 2023 as part of JAXA's 2023 balloon program, labeled B23-06. The preparations for the flight were carried out in three phases. The development of each component, such as the gondola, liquid argon detector, DAQ, software, and others, conducted at each institutes, respectively. Following the successful integration test of all elements at Waseda University, the payload was transported to JAXA Sagamihara Campus in May 2023. At Sagamihara, the payload underwent testing for vacuum and low-temperature tolerance, as well as assembly and compatibility testing with the communication system prepared by the JAXA Balloon Group. In June 2023, the payload was transported to the Taiki Aerospace Research Field (TARF) in Hokkaido, Japan, which served as the balloon launch site [98]. The payload preparation was completed, and it was finally integrated with the TARF communication equipment. By early July, all preparations were finished, and the payload was

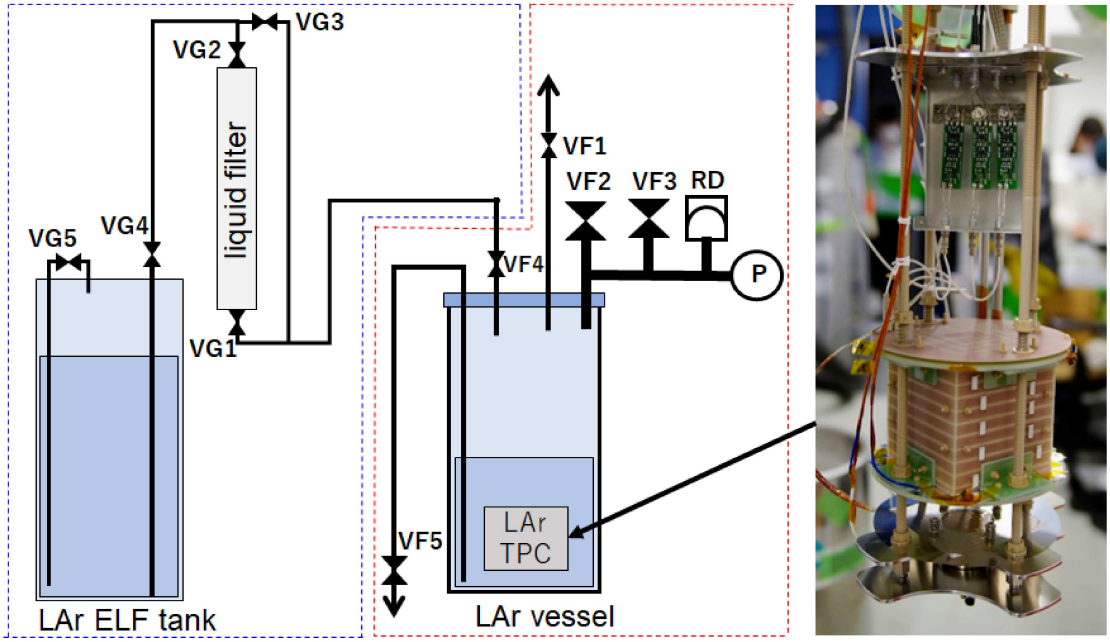

Fig. 7.3. Schematic diagram of liquid argon operation system and an image of liquid argon TPC.

placed on standby to await favorable weather conditions for launch. The weather conditions were favorable for flight on July 27, 2023, and the balloon were released early in the morning. After approximately 3 hours of flight, the payload landed in the Pacific Ocean, roughly 40 km from TARF, and was subsequently recovered by a fishing boat. Figure 7.4 shows the payload set on the balloon launcher and a helium-filled balloon (left), a scene of the balloon launch (center), a payload floating over the Pacific Ocean (upper right), and a scene of recovery by a fishing boat (lower right), respectively.

Fig. 7.4. Photos during engineering flight.

7.4 Operation procedure

The liquid argon detector was operated in this flight, following the procedure outlined in Figure7.5. Initially, on the morning before the release, the liquid argon vessel was filled with sufficient argon to immerse the detector for the entire observation period in the building where the detector was assembled. Subsequently, the payload was positioned on the launcher, and it was monitored online until the release time. The team then took a break and waited until midnight on that day. A few hours before the launch, the team reconvened to make final preparations. Just before the launch, voltage was applied to the PMT, and data acquisition of pressure, temperature, and the detector was initiated. However, no voltage was applied to the TPC electric field, resulting in no visible charge signal. This precaution was taken to prevent discharge during balloon launch. After releasing the balloon, stability of the attitude was confirmed using the acceleration sensor. Subsequently, the TPC voltage was then activated, initiating observation.

The TPC voltage is turned off, and the liquid argon is drained before detaching the balloon. The detector is exposed to the gas phase due to liquid drainage, posing a risk of discharge; hence, the cathode voltage is lowered. Balloon detachment from the payload occurs without waiting for complete liquid argon drainage due to the necessity of controlling the landing point. Once drainage completion is confirmed through the inner pressure of the liquid argon vessel, data acquisition is immediately terminated, and all liquid argon detector operation systems are shut down. The payload, decelerated by a parachute, lands in the sea, and retrieval is carried out by a fishing boat. Liquid argon handling is managed by our group, while balloon operations, including launch, altitude control, and detachment, are overseen by the JAXA Balloon Group.

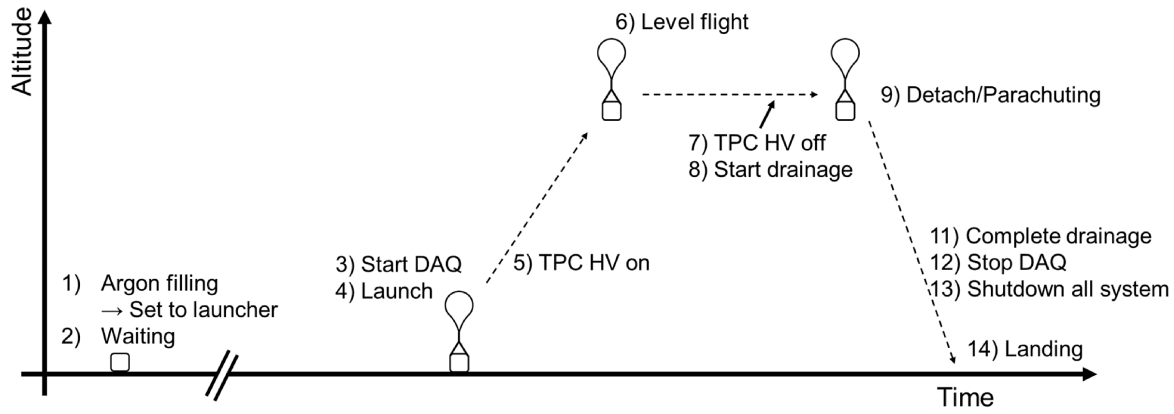

Fig. 7.5. Schematic diagram of liquid argon operation in engineering flight.

7.5 Flight result

7.5.1 Flight overview

Figure7.6 shows flight trajectory in left panel and the flight altitude in right panel for this mission. The GPS data was provided by JAXA/ISAS Balloon Group. The balloon was released at 03:55 AM on July 27th, 2023, and achieved level flight at 05:59 AM, reaching a maximum altitude of approximately 28.9 km. At 6:33 AM, before gondola detachment, VF5 was opened to initiate the release of liquid argon, and the balloon and payload were subsequently detached at 06:43 AM. The completion of the liquid argon release was confirmed at 07:00 AM during a soft descent facilitated by parachute. All power, including the CPU, was immediately turned off. The payload safely landed on the sea at 07:07 AM and was recovered within a few minutes. Following recovery, no damage was observed to the gondola, liquid argon container, TPC, or the pressurized container and its contents.

Environmental data, including pressure and temperature, along with PMT waveforms, were continuously recorded from the pre-launch phase until all power supplies were shut down. In contrast, cathode voltage application was delayed by 5 minutes after launch to mitigate the risk of discharge due to the shock of release. Furthermore, the cathode voltage was turned off before liquid argon exit to prevent discharge caused by exposure to the gas phase. Consequently, the ionizing electron signals were acquired from 5 minutes after launch (at an altitude of about 2 km) up to the moment just before the initiation of liquid argon drainage.

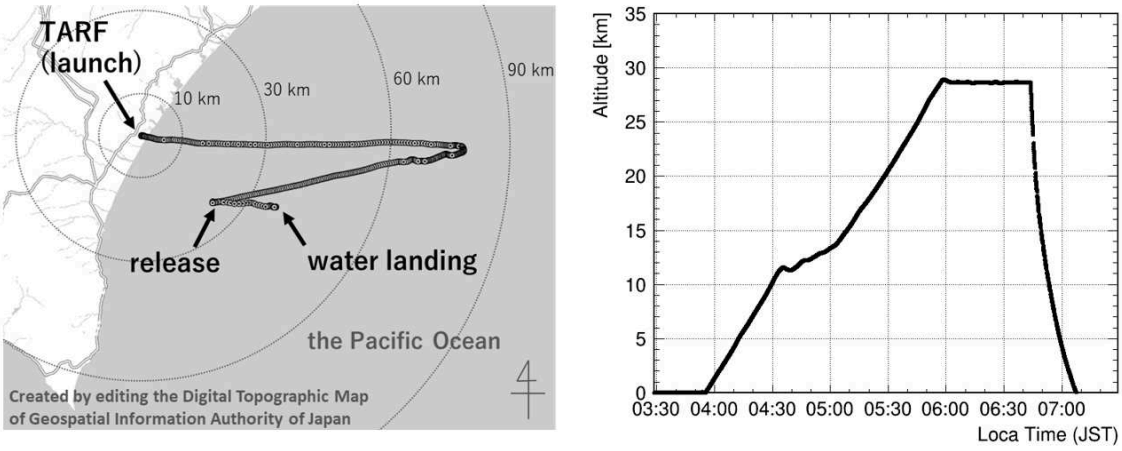

Fig. 7.6. Flight pass (left) and altitude (right) for this mission.

7.5.2 Maintaining and drainage of liquid argon

Figure 7.7 displays the time variation of the pressure inside the liquid argon vessel (red line) and the temperature of vessel bottom (blue line) alongside the atmospheric pressure (black line). Note that atmospheric pressure is represented as a value converted from altitude using the U.S. Standard

Atmospheric Model. Throughout the flight, the pressure within the liquid argon vessel is consistently maintained within the expected range of 1.1–1.2 atm. The thermometer, positioned below the liquid surface, monitors the liquid argon temperature, confirming that the argon remained in the liquid phase from the time of launch to the initiation of liquid drainage. Internal pressure remained below the operating pressure of the differential pressure safety valve and rupture disk throughout the entire period from filling to recovery.

Next, our focus shifts to the liquid argon drainage process: immediately after opening VF5, the vessel's pressure decreases, confirming the initiation of drainage. However, within a few seconds, the liquid outlet closes, causing a subsequent pressure increase. As anticipated, the sudden decrease in atmospheric pressure below the triple point leads to the rapid solidification of liquid argon near the drainage tube outlet. Additionally, the liquid argon within the drainage tube vaporizes, contributing to an elevated pressure inside the container compared to the pre-draining state. Given that VF5 was opened and closed intermittently until the completion of liquid drainage, the internal pressure experienced corresponding fluctuations. Following the separation of the payload from the balloon, the altitude decreased, resulting in an increase in atmospheric pressure to approximately the triple point. This change facilitated the smooth progression of the drainage process. In this specific flight, liquid drainage occurred after the altitude was reduced. In future flight, we will explore enhancing the drainage method, such as by considering the installation of a heater in the drainage line.

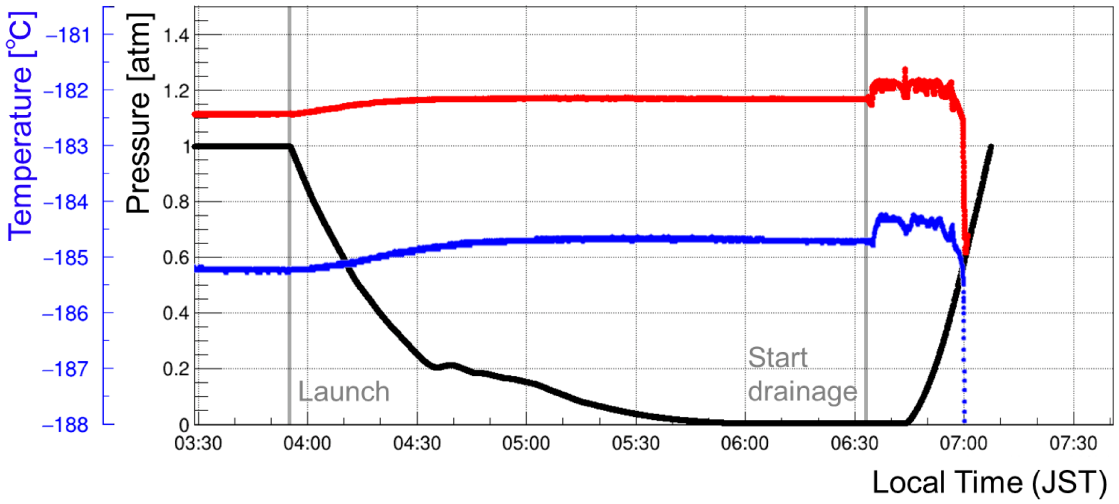

Fig. 7.7. Changes in liquid argon vessel pressure (black) and atmospheric pressure (black), and temperature (blue) during flight.

7.5.3 Liquid argon signal obtained during flight

Fig. 7.8, from left to right, shows the PMT waveform, ionized electron signal waveform, anode electrode shape and corresponding channel number. In this detector, the ionized electron signal is directly obtained from the output of the charge-integrating amplifier, so the change in voltage, i.e. the amount of increase,

corresponds to the amount of electron signal. Also, t=0 µs corresponds to Z=10 cm and t=120 µs corresponds to Z=0 cm. The PMT waveform shows two time constant components of liquid argon scintillation (τ = 6 ns, 1.5 mus). These signals were recorded from immediately after the release of the balloon to just before the drainage.

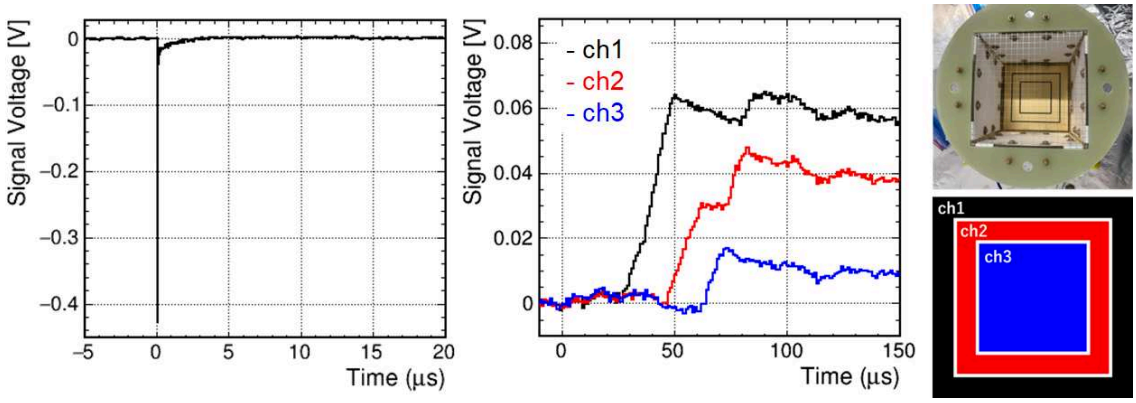

Fig. 7.8. Waveforms of liquid argon TPC signal (left: PMT, center: charge amplifier) and anode electrode shape (right).

The trigger rate was constrained by CPU performance, saturating at around 60 Hz. Therefore, the event rate was determined by fitting the distribution of the time difference between each event to an exponential function:

$$f(t) = A \times exp(-R \times t), \tag{7.1}$$

where A is a scale factor and R is the event rate. The left plot of Fig. 7.9 shows the distribution of the time difference at an altitude of 5 km (black plots) and fitting result (red line). the right plot of Figure 7.9 represents the rates calculated by exponential fitting, providing the true event rates unrestricted by 60 Hz limit. This fitting process was performed separately for each altitude. The event rate increases with the ascent of the balloon up to about 20 km and decreases with further altitude, exhibiting a shower maximum.

7.6 Summary and future prospect

A balloon engineering flight was conducted as the first test of liquid argon TPC onboard a flying object, and the balloon was released in the early morning of July 27th,2023, and flight data including 44 minutes of level flight was obtained. The following challenges were addressed in this balloon flight: (1) shock and vibration, (2) weight limitations, (3) power limitations, (4) atmospheric pressure and temperature changes with altitude, (5) remote operation of the detector, and (6) safe recovery of the detector. To minimize the impact of shock and vibration, a liquid single-phase detector was employed. Due to power and weight constraints, a refrigerator was not used. Instead, the liquid argon vessel was filled with enough liquid argon to immerse the detector for the entire flight duration, and liquid argon was evaporated naturally. In addition, the liquid argon vessel was designed to have a heat inflow of 10 W or less to limit the amount

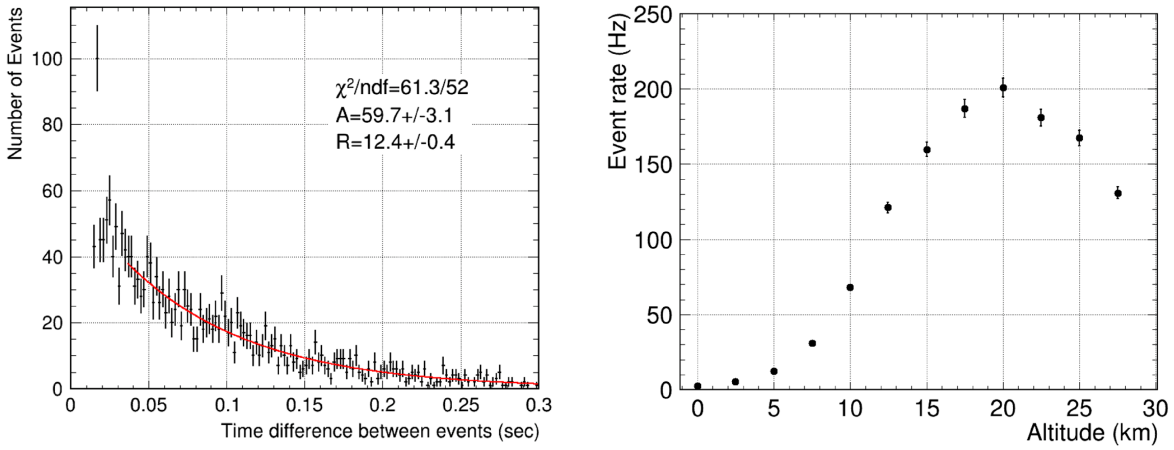

Fig. 7.9. (Left) Distribution of time differences at an altitude of 5 km (black plots) and the fitting result (red line). (Right) Event rates calculated by exponential fitting as a function of altitude.

of evaporation. The absolute pressure valve was used to maintain the internal pressure of the vessel at a constant value even if the atmospheric pressure changed in accordance with changes in altitude. In addition, the entire gondola was covered with insulation to minimize the effects of changes in outside temperature. Voltage and DAQ settings were changed wirelessly during the flight, and environmental data such as temperature and pressure could be constantly monitored on the ground. For safe recovery, the liquid argon was drained in the sky to avoid hazards, such as the explosive boiling of liquid argon. As a result, argon was kept in the liquid phase in the stratosphere, and data from the liquid argon detector was successfully acquired.

The GRAMS experiment [30] is planned to use the liquid argon detector to simultaneously observe cosmic ray antiparticles and cosmic ray gamma rays. The balloon engineering tests conducted in this study represents the first steps in demonstrating the feasibility of operating a liquid argon detector on a balloon, providing valuable insights for future experiments like GRAMS. While the natural evaporation method proved effective for the relatively short flight duration of a few hours in this experiment, alternative liquid argon maintenance mechanisms need consideration for longer flights lasting a month or more. Options include cooling with a refrigerator or liquid nitrogen, or preparing a larger liquid argon tank for storage.

Chapter 8

Conclusion

Although the existence of dark matter has been strongly suggested by numerous cosmological observations, its nature remains entirely unknown. Many experimental groups are currently conducting experiments in an effort to elucidate this mysterious substance. Liquid argon detectors, in particular, exhibit outstanding performance in the dark matter search. Due to its capabilities in energy/position reconstruction, robust particle identification, and scalability, liquid argon detectors currently lead in direct dark matter searches across a broad range of dark matter masses from 1 GeV to 1 TeV. Furthermore, there is an anticipation for its application in indirect dark matter search experiments, where detectors are mounted on scientific balloons and satellites. This marks a novel application for liquid argon detectors, where development is already underway.

To improve the performance of the liquid argon detector for dark matter search, we addressed three points: firstly, the enhancement of the light collection efficiency of vacuum ultraviolet light from scintillation (discussed in Chapters 4 and 5); secondly, the measurement of the spectrum in the visible region in the gas phase, which is still not fully understood (Chapter 6); thirdly, a balloon-borne engineering test of a liquid argon detector for its application in indirect search experiments (Chapter 7). This chapter provides a summary and discusses their application in dark matter search experiments.

8.1 Summary

The liquid argon detector detects S1 and/or S2 light signals, enabling energy reconstruction and particle identification. The primary component of this light signal is scintillation light emitted during de-excitation, which is a VUV light with a wavelength of 128 nm. In addition to VUV light, the S2 emission in the gaseous phase includes UV and IR light resulting from excitation-deexcitation processes, as well as visible light, which has been proposed as NBrS but remains not fully understood. A better understanding of the properties of these light signals and their efficient detection will contribute to enhanced detector performance, such as a lower energy threshold, higher energy resolution, and more robust particle identification. Therefore, our focus was on enhancing the light collection efficiency and precisely measuring the luminescence in the visible region in the gas phase.

The enhancement in light collection efficiency was realized through two approaches: optimization of wavelength shifting using TPB and implementation of TSV–MPPC. First, by establishing a highly reproducible vacuum evaporation system and adjusting the thickness of the TPB coating formed by it, a light collection efficiency of 12.8 ± 0.3 p.e./keVee was achieved. This corresponds to close to unity acceptance ($A_{vuv} \times \varepsilon_{WLS} \times A_{vis} = 1$) under the assumption of $QE_{PMT} = 30\%$. The PSD capability is also

improved compared to the detector with a light collection efficiency of 5.7 p.e./keVee. Subsequently, we confirmed that the operability of TSV–MPPC at liquid argon temperatures with a high detection efficiency (>50%). Additionally, the operability of the liquid argon detector with MPPCs was demonstrated using a TSV—MPPC arrays. Improvements in energy resolution and PSD capability could not be confirmed due to issues with the MPPC readout circuit PCB. However, we achieved a light collection efficiency of 23.0 ± 4.6 photons/keVee with TSV–MPPCs.

The argon EL in the visible light region, ranging from 300 to 600 nm, was investigated under room temperature and normal pressure. Gaseous TPC was employed for efficient measurements, providing a high turnover rate compared to a liquid argon TPC. The secondary emission light from the TPC luminescence region was dispersed utilizing a spectrometer. We acquired data on the wavelength spectrum, luminescence-field dependence, and the effect of nitrogen impurities on the light yield. Even in an environment where the nitrogen impurity emitting visible light is sufficiently small (0.1 ± 0.7 ppm, which is consistent with zero within uncertainties), we observed emission across a continuous spectrum from 300 nm to 600 nm. Additionally, visible light was observed at a lower electric field intensity than the threshold electric field intensity for ordinary EL of approximately 4Td. The observed wavelength and electric field dependencies could be explained by considering the NBrS model.

These photodetection techniques not only benefit detectors specialized in direct dark matter searches but also contribute to the development of detectors for indirect dark matter searches. In indirect dark matter searches using charged antiparticles as probes, the signal yield is significant, allowing for signal reconstruction with existing liquid single-phase TPCs, and thus, the detector performance requirements are not stringent. In contrast, when gamma rays are employed as probes, they possess low deposition energy (ranging from several tens to several hundreds of keV per reaction point) and necessitate spatial resolution to identify the arrival direction. Existing detectors lack sufficient energy resolution for such charge signals, indicating the need for further detector development. In addition, neutrons must be distinguished from gamma rays in liquid argon detectors, as both deposit their energy similarly. Unlike ground-based experiments, where neutron background can be reduced by installing shields, airborne experiments distinguish them analytically, employing methods such as PSD in liquid argon. Therefore, enhancing the light collection efficiency significantly contributes to indirect dark matter searches, especially in the context of gamma rays.

However, to apply these developments for indirect searches, such as those on scientific balloons, we need to address technical challenges specific to flying objects that are not present in ground-based experiments. A critical challenge in terms of liquid argon detector design involves dealing with shocks and shaking during flight. For instance, unlike a single-phase detector, a double-phase TPC is not suitable for operation on flying objects due to the need for precise control of the liquid level to within a few millimeters. In addition to this challenge, there are various other obstacles that must be addressed before considering the detector's performance, including changes in atmospheric pressure and temperature due to variations in altitude. Moreover, constraints on power consumption and payload weight further complicate the airborne operation of liquid argon.

The liquid argon detector has never been operated on a flying object before, and the environmental conditions it might face in the stratosphere are unknown. To explore the feasibility of operation in airborne

conditions, we conducted the balloon-borne flight of the liquid argon detector in the stratosphere. The liquid argon detector was compact ($10 \times 10 \times 10\ cm$) and was operated as single-phase TPC. The liquid argon evaporated spontaneously without the use of a refrigerator. The vessel pressure was maintained at a constant level using an absolute pressure valve. On July 7, 2023, the balloon was launched at the TARF owned by JAXA, reaching a maximum altitude of 28.9 km with a total flight time of 3 hours and 12 minutes. Environmental data measurements, including pressure and temperature, demonstrated that the argon remained safely in liquid phase during ascent and levitation. The liquid argon TPC has also been successful in obtaining both scintillation and ionized electron data, and in observing charged cosmic rays in the upper atmosphere. This balloon engineering test proved operational feasibility of the liquid argon detector in a balloon-borne environment.

8.2 Discussion for dark matter search with liquid argon detector

As outlined in Section 1.2, detectors utilized in direct dark matter search experiments require (1) a large target mass, (2) a low energy detection threshold, (3) minimal internal/external background, and (4) particle identification capability. In this section, we discuss how the results obtained in these studies, which focus on the enhancement of light collection efficiency and the detailed measurement of NBrS, influence these requirements.

PSD capability with the enhanced light collection efficiency

The liquid argon detector distinguishes between ER events and NR events through PSD. The deviation of the PSD distribution is primarily influenced by statistical fluctuations in the number of photons, and a higher light collection efficiency leads to a smaller deviation, indicating better PSD capability. Figure 8.1 displays the rejection power estimated by the MC simulation, established in Section 4.5.4, as a function of light collection efficiency. The rejection power of ER events is defined in Eq. 4.5 based on the PSD mean of NR, simplifying the discussion.

Initially, we compare the PSD capability of the newly constructed detector in this study, with a light collection efficiency of 12.8 p.e./keVee, to the previously constructed one with 5.7 p.e./keVee. For instance, at a recoil energy of 10 keVnr, R_{PSD}^{ER} improved by a factor of approximately 2 (from 5 to 10). Similarly, at 20 keVnr, R_{PSD}^{ER} improved by a factor of more than 10 (from 30 to 400). Additionally, despite experiencing no improvement in PSD capability due to readout PCB issues, a light collection efficiency of 23.0 p.e./keVee was observed in the liquid argon detector with TSV–MPPCs. Assuming that the same level of resolution as a PMT can be achieved in the future, the TSV–MPPC detector is expected to enhance R_{PSD}^{ER} by a factor of about 4 (from 5 to 20) at 10 keVnr and approximately 3000 (from 30 to 1×10^4) at 20 keVnr compared to detector with light collection efficiency of 5.7 p.e./keVee.

In direct dark matter search experiments with a liquid argon detector, ER backgrounds, including gamma rays from the detector components and ^{39}Ar-derived β^+ rays, are effectively distinguished from NR events such as dark matter-nuclear recoil by PSD. However, In the low recoil energy region, the PSD dispersion is large due to small light yield, making it difficult to separate ER from NR. Referring to the DarkSide-50

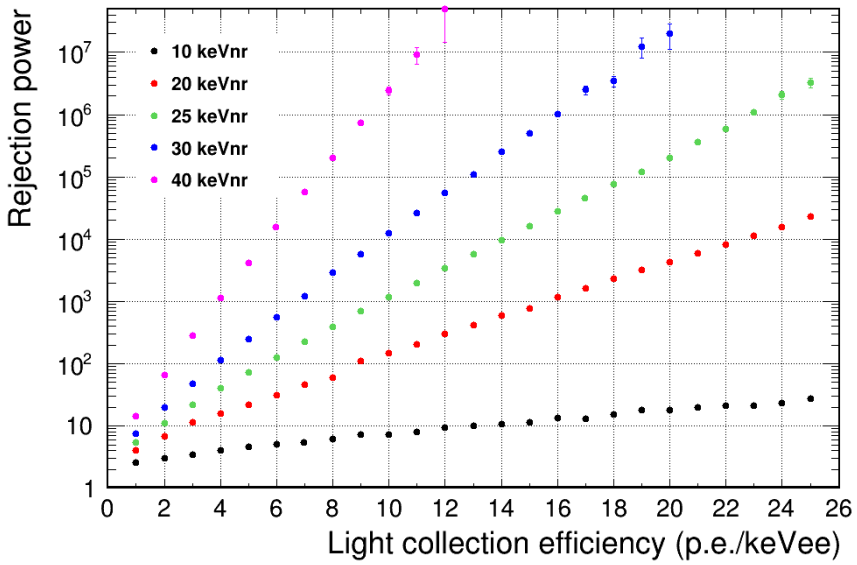

Fig. 8.1. Rejection power estimated by MC simulation as a function of the light collection efficiency, at a signal efficiency of 50%.

results reported in Ref.[99], the energy threshold of the region of interest is approximately 40 keVnr, constrained by the ER rejection capability through PSD. Let us consider the scenario where the current light collection efficiency of DarkSide-50, approximately 8 p.e./keVee, is enhanced to 23 p.e./keVee. Note, however, that PSD rejection power is assumed to improve according to Fig. 8.1. At light collection efficiency of 8 p.e./keVee, a rejection power of 2×10^5 can be achieved at a signal efficiency of 50% for recoil energy of 40 keVnr. On the other hand, at 23 p.e./keVee, a rejection power of 2×10^5 can be obtained even at a recoil energy of 25 keVnr. Naturally, a detailed discussion should take into account the spectrum of ER background events currently obtained by DarkSide-50, however, here we only discussed the PSD power.

As discussed above, the enhancement of light collection efficiency improves the PSD capability and lowers the energy threshold due to improved PSD capability. Thus, it is valid for requirements (2) and (4).

Application of NBrS as a new signal channel in liquid argon detector

We discuss the applicability of NBrS as a newly signal channel for liquid argon detectors, given its emission wavelength in the visible light range, which is easier to detect than VUV. The first crucial factor in considering the applicability of NBrS is its light yield. We adopt the bottom panel of Fig. 6.2 as the luminescence yield (F_{NBrS}) to calculate the total light yield, as the observations, such as the wavelength spectrum and electric field dependency, as well as the rough estimation of the detected number of photons, are consistent with that model. The total number of photons emitted from the NBrS mechanism, denoted

as N_γ^{tot}, is given by the following equation:

$$N_\gamma^{tot} = N_e \times \rho \times d \times \int_{\lambda_l}^{\lambda_h} F_{\mathrm{NBrS}}(\lambda)\, d\lambda, \tag{8.1}$$

where N_e is the number of drift electrons, ρ is the number density of the argon atoms, d is the distance of the luminescence field, and λ is the wavelength. Here, we assumed the luminescence field of 4.6 Td, $N_e = 1$ and the ideal gas at 1 atm argon, i.e. $\rho = 2.7 \times 10^{19}$ atom/cm^3. Integration is performed in the range of $\lambda_l = 200$ nm to $\lambda_h = 700$ nm, encompassing the sensitivity range of the R11065, resulting in N_γ^{tot} as follows:

$$\begin{aligned} N_\gamma^{tot} &= 1 \times (2.7 \times 10^{19}) \times 1 \times (9.7 \times 10^{-4}) \quad [1 \times 10^{-17}\ \text{photons/e}^-] \\ &= 0.26\ [\text{photons/e}^-]. \end{aligned} \tag{8.2}$$

Compared to ordinary EL, which typically results in the detection of several tens to hundreds of photo-electrons per drift electron, NBrS is expected to yield only about 1/100th of the photons, even if detected with collection efficiency of 100%. Therefore, NBrS does not have an immediate application to dark matter searches. However, luminescence in a low electric field could find application in detector operation in environments where a strong electric field cannot be formed or emission within liquid argon. It is also possible to increase the amount of luminescence by extending the luminescence field distance. The exploration of applications of NBrS with these characteristics is a subject for future work.

8.3 Future prospect

Several upcoming experiments employing liquid argon detectors are planned for direct dark matter searches, indirect dark matter searches, and neutrino experiments.

In direct dark matter searches, stringent requirements such as minimizing background events and increasing detector mass are imperative, especially for exploring lower cross-sections. The next-generation direct dark matter search experiment, DarkSide-20k [100], is designed to utilize 23 t UAr in its effective volume, thereby reducing the presence of ^{39}Ar in the beta source. Generating large quantities of UAr poses a significant technical challenge, and both generation and purification processes will be carried out at Urania and Aria facilities [101]. To enhance the detector performance, a semiconductor photodetector developed in collaboration with Fondazione Bruno Kessler will be employed. This photodetector exhibits higher PDE and lower radiation impurities compared to traditional PMTs. Addressing the need for a cathode electric field of -50 kV or higher, essential for larger detector sizes, the approach involves routing the feedthrough ground through to the liquid argon, ensuring that the high-voltage components remain shielded from gas argon exposure. The expected sensitivity of DarkSide-20k is projected to reach the cross section of O(10^{-48}) for dark matter with a mass of 1 TeV/c^2, with an exposure of 20 t×10 years. The optimization of TPB wavelength shifting conducted in this study is expected to have broad applicability, enhancing photon collection efficiency in upcoming experiments. Additionally, our findings indicate the utility of TSV-MPPCs, distinct from the semiconductor photodetectors intended for use in DarkSide-20k,

especially in low-temperature environments. Consideration of replacement with TSV-MPPCs featuring higher PDE could be effective. The optimization of TPB wavelength shifting conducted in this study is expected to have broad applicability, enhancing photon collection efficiency in upcoming experiments like DarkSide-20k. We have also shown that TSV-MPPCs, which are different from the semiconductor photodetectors planned for use in DarkSide-20k, are useful at low temperatures, and replacement with TSV-MPPCs with higher PDE may be effective.

On the other hands, in indirect dark matter searches, the first experiment using a liquid argon detector, GRAMS, is currently in the preparatory stages. Unlike experiments using conventional magnetic fields [25, 28], liquid argon detectors offer the unique advantage of detecting incident particles from all directions. In indirect search experiments targeting charged antiparticles, such as antideuterons as dark matter probes, it becomes crucial to elevate the detector above the stratosphere, minimizing the atmospheric effects. The GRAMS experiment aims to achieve this by deploying the detector on an Antarctic scientific balloon in the late 2020s. The ongoing development of the GRAMS experiment places a high priority on ensuring the stable operation of the liquid argon detector on the scientific balloon and validating the interaction between charged antiparticles and liquid argon. The results of the balloon engineering tests conducted in this study showcase the feasibility of operating the liquid argon detector in the stratospheric conditions of a scientific balloon. These findings provide valuable insights for future indirect search experiments, including the upcoming GRAMS mission. Conversely, given the extended duration of the actual observations spanning over a month, the methodology for maintaining high-purity liquid argon necessitates a reassessment. To prove operation of a prototype detector, GRAMS is planning test flight scheduled for 2025-2026. In addition to charged antiparticles, the GRAMS detector is designed to detect gamma rays in the MeV energy band, utilizing the liquid argon detector as a Compton camera. The challenge lies in the fact that a single Compton scattering results in a modest energy deposition of only a few tens to a few hundreds of keV. Achieving a position resolution at a few millimeter level and an energy resolution equivalent to a few hundred electrons, as well as reconstructing the sequence of Compton events [102], presents significant technical challenges. Notably, a liquid argon Compton camera has not been demonstrated in operation until now. While the detector's performance on the ground is currently sufficient for charged antiparticle observations, the detection of MeV gamma rays necessitates the development of a detector with improved energy and position resolution. This aspect is actively under study and development.

As described above, the development of liquid argon detectors for high sensitive dark matter search is active.

Bibliography

[1] F. Zwicky, Die Rotverschiebung von extragalaktischen Nebeln, Helv. Phys. Acta **6**, 110–127 (1933).

[2] K. G. Begeman *et al.*, Extended rotation curves of spiral galaxies: Dark haloes and modified dynamics, Mon. Not. Roy. Astron. Soc. **249**, 523 (1991).

[3] D. Clowe *et al.*, A direct empirical proof of the existence of dark matter, Astrophys. J. Lett. **648**, L109–L113 (2006).

[4] N. Aghanim *et al.* (Planck Collaboration), Planck 2018 results. I. Overview and the cosmological legacy of Planck, Astron. Astrophys. **641**, A1 (2020).

[5] LHC Machine, JINST **3**, S08001 (2008).

[6] F. Tanedo, Defense against the dark arts notes on dark matter and particle physics flip tanedo, (2015).

[7] R. H. Helm, Inelastic and elastic scattering of 187-mev electrons from selected even-even nuclei, Phys. Rev. **104**, 1466–1475 (1956).

[8] B. Suerfu, M. Wada, W. Peloso, M. Souza, F. Calaprice, J. Tower, and G. Ciampi, Growth of ultra-high purity nai(tl) crystals for dark matter searches, Phys. Rev. Res. **2**, 013223 (2020).

[9] Tarec Saab *et al.*, Dark matter limit plotter v5.13, .

[10] F. Ruppin *et al.*, Complementarity of dark matter detectors in light of the neutrino background, Phys. Rev. D **90**, 083510 (2014).

[11] P. Agnes *et al.* (DarkSide-50 Collaboration), Search for low-mass dark matter WIMPs with 12 ton-day exposure of DarkSide-50, Phys. Rev. D **107**, 063001 (2023).

[12] R. Ajaj *et al.* (DEAP Collaboration), Search for dark matter with a 231-day exposure of liquid argon using DEAP-3600 at SNOLAB, Phys. Rev. D **100**, 022004 (2019).

[13] E. Aprile *et al.* (XENON Collaboration), Search for Coherent Elastic Scattering of Solar ^{8}B Neutrinos in the XENON1T Dark Matter Experiment, Phys. Rev. Lett. **126**, 091301 (2021).

[14] E. Aprile *et al.* (XENON Collaboration), First Dark Matter Search with Nuclear Recoils from the XENONnT Experiment, Phys. Rev. Lett. **131**, 041003 (2023).

[15] J. Aalbers *et al.* (LZ Collaboration), First Dark Matter Search Results from the LUX-ZEPLIN (LZ) Experiment, Phys. Rev. Lett. **131**, 041002 (2023).

[16] A. H. Abdelhameed *et al.* (CRESST Collaboration), First results from the CRESST-III low-mass dark matter program, Phys. Rev. D **100**, 102002 (2019).

[17] R. Agnese *et al.* (SuperCDMS Collaboration), Search for Low-Mass Dark Matter with CDMSlite Using a Profile Likelihood Fit, Phys. Rev. D **99**, 062001 (2019).

[18] Q. Arnaud *et al.* (NEWS-G Collaboration), First results from the NEWS-G direct dark matter search experiment at the LSM, Astropart. Phys. **97**, 54–62 (2018).

[19] G. Adhikari *et al.* (COSINE-100 Collaboration), Strong constraints from COSINE-100 on the DAMA dark matter results using the same sodium iodide target, Sci. Adv. **7**, abk2699 (2021).

[20] C. Amole *et al.* (PICO Collaboration), Dark Matter Search Results from the Complete Exposure of the PICO-60 C_3F_8 Bubble Chamber, Phys. Rev. D **100**, 022001 (2019).

[21] A. Aguilar-Arevalo *et al.* (DAMIC Collaboration), Results on low-mass weakly interacting massive particles from a 11 kg-day target exposure of DAMIC at SNOLAB, Phys. Rev. Lett. **125**, 241803 (2020).

[22] R. Agnese *et al.* (SuperCDMS Collaboration), Projected Sensitivity of the SuperCDMS SNOLAB experiment, Phys. Rev. D **95**, 082002 (2017).

[23] M. Cadeddu, Darkside-20k sensitivity, directional dark matter detection and the role of coherent elastic neutrino-nucleus scattering background, Ph.D. thesis, University of Cagliari (2018).

[24] M. Schumann *et al.*, Dark matter sensitivity of multi-ton liquid xenon detectors, JCAP **10**, 016 (2015).

[25] M. Aguilar *et al.* (AMS Collaboration), First Result from the Alpha Magnetic Spectrometer on the International Space Station: Precision Measurement of the Positron Fraction in Primary Cosmic Rays of 0.5–350 GeV, Phys. Rev. Lett. **110**, 141102 (2013).

[26] M.-Y. Cui *et al.*, Possible dark matter annihilation signal in the AMS-02 antiproton data, Phys. Rev. Lett. **118**, 191101 (2017).

[27] Z. Weng (AMS Collaboration), Towards Understanding the Origin of Cosmic-Ray Positrons, PoS **ICRC2019**, 091 (2020).

[28] H. Fuke *et al.*, Search for cosmic-ray antideuterons, Phys. Rev. Lett. **95**, 081101 (2005).

[29] T. Aramaki *et al.* (GAPS Collaboration), Antideuteron Sensitivity for the GAPS Experiment, Astropart. Phys. **74**, 6–13 (2016).

[30] T. Aramaki *et al.*, Dual MeV Gamma-Ray and Dark Matter Observatory - GRAMS Project, Astropart. Phys. **114**, 107–114 (2020).

[31] S. Hoof *et al.*, A Global Analysis of Dark Matter Signals from 27 Dwarf Spheroidal Galaxies using 11 Years of Fermi-LAT Observations, JCAP **02**, 012 (2020).

[32] J. M. Carmona *et al.*, Neutron background at the Canfranc Underground Laboratory and its contribution to the IGEX-DM dark matter experiment, Astropart. Phys. **21**, 523–533 (2004).

[33] F. Tortorici *et al.* (ICARUS Collaboration), The ICARUS Experiment, Nucl. Part. Phys. Proc. **306-308**, 154–162 (2019).

[34] B. Abi *et al.* (DUNE Collaboration), Long-baseline neutrino oscillation physics potential of the DUNE experiment, Eur. Phys. J. C **80**, 978 (2020).

[35] G. Aad *et al.* (ATLAS Collaboration), The ATLAS Experiment at the CERN Large Hadron Collider, JINST **3**, S08003 (2008).

[36] M. Agostini *et al.* (GERDA, (GERDA Collaboration)* Collaboration), Final Results of GERDA on the Two-Neutrino Double-β Decay Half-Life of Ge76, Phys. Rev. Lett. **131**, 142501 (2023).

[37] E.Aprile, Noble gas detector, (2006).

[38] P. Benetti *et al.* (WARP Collaboration), Measurement of the specific activity of ar-39 in natural argon, Nucl. Instrum. Meth. A **574**, 83–88 (2007).

[39] J. Xu *et al.*, A study of the trace 39ar content in argon from deep underground sources, Astroparticle Physics **66**, 53–60 (2015).

[40] C. Regenfus *et al.*, Study of nuclear recoils in liquid argon with monoenergetic neutrons, J. Phys. Conf. Ser. **375**, 012019 (2012).

[41] M. Miyajima *et al.*, Average energy expended per ion pair in liquid argon, Phys. Rev. A **9**, 1438–1443 (1974).

[42] J. Lindhard *et al.*, Integral equations governing radiation effects, Mat. Fys. Medd. Dan. Vid. Selsk **33**, 1–42 (1963).

[43] J. Lewin and P. Smith, Review of mathematics, numerical factors, and corrections for dark matter experiments based on elastic nuclear recoil, Astropart. Phys. **6**, 87–112 (1996).

[44] H. Cao *et al.* (SCENE Collaboration), Measurement of Scintillation and Ionization Yield and Scintillation Pulse Shape from Nuclear Recoils in Liquid Argon, Phys. Rev. D **91**, 092007 (2015).

[45] T. Joshi *et al.*, First measurement of the ionization yield of nuclear recoils in liquid argon, Phys. Rev. Lett. **112**, 171303 (2014).

[46] P. Agnes *et al.*, Measurement of the liquid argon energy response to nuclear and electronic recoils, Phys. Rev. D **97**, 112005 (2018).

[47] T. Washimi, Study of Electron Recoil Background Rejection in Double Phase Argon Detector for the WIMP Dark Matter Search, Ph.D. thesis, Waseda U. (2018), *in Japanese*.

[48] M. Kimura *et al.*, Measurement of the scintillation efficiency for nuclear recoils in liquid argon under electric fields up to 3 kV/cm, Phys. Rev. D **100**, 032002 (2019).

[49] J. Thomas and D. A. Imel, Recombination of electron-ion pairs in liquid argon and liquid xenon, Phys. Rev. A **36**, 614–616 (1987).

[50] T. Doke *et al.*, Absolute Scintillation Yields in Liquid Argon and Xenon for Various Particles, Jap. J. Appl. Phys. **41**, 1538–1545 (2002).

[51] S. Amoruso *et al.*, Analysis of the liquid argon purity in the icarus t600 tpc, Nuclear Instruments and Methods in Physics Research Section A: Accelerators, Spectrometers, Detectors and Associated Equipment **516**, 68–79 (2004).

[52] M. Hofmann *et al.*, Ion-beam excitation of liquid argon, Eur. Phys. J. C **73**, 2618 (2013).

[53] A. Hitachi *et al.*, Effect of ionization density on the time dependence of luminescence from liquid argon and xenon, Phys. Rev. B **27**, 5279–5285 (1983).

[54] M. Kimura *et al.*, Liquid argon scintillation response to electronic recoils between 2.8–1275 kev in a high light yield single-phase detector, Phys. Rev. D **102**, 092008 (2020).

[55] R. Acciarri *et al.* (WArP Collaboration), Oxygen contamination in liquid Argon: Combined effects on ionization electron charge and scintillation light, JINST **5**, P05003 (2010).

[56] R. Acciarri *et al.* (WArP Collaboration), Effects of Nitrogen contamination in liquid Argon, JINST **5**, P06003 (2010).

[57] T. Doke, A. Hitachi, S. Kubota, A. Nakamoto, and T. Takahashi, Estimation of Fano factors in liquid argon, krypton, xenon and xenon-doped liquid argon, Nucl. Instrum. Meth. **134**, 353–357 (1976).

[58] G. Klein and M. J. Carvalho, Argon luminescence bands between 1600 and 2900 Å, Journal of Physics B: Atomic and Molecular Physics **14**, 1283 (1981).

[59] T. Takahashi *et al.*, Emission spectra from ar-xe, ar-kr, ar-n2, ar-ch4, ar-co2 and xe-n2 gas scintillation proportional counters, Nuclear Instruments and Methods in Physics Research **205**, 591–596 (1983).

[60] A. Korol and A. Solov ' yov, Polarization bremsstrahlung, Springer (2014), 10.1007/978-3-642-45224-6.

[61] A. Buzulutskov, E. Shemyakina, A. Bondar, A. Dolgov, E. Frolov, V. Nosov, V. Oleynikov, L. Shekhtman, and A. Sokolov, Revealing neutral bremsstrahlung in two-phase argon electroluminescence, Astroparticle Physics **103**, 29–40 (2018).

[62] B. Aimard *et al.*, A 4 tonne demonstrator for large-scale dual-phase liquid argon time projection chambers, JINST **13**, P11003 (2018).

[63] B. Abi *et al.*, First results on protodune-sp liquid argon time projection chamber performance from a beam test at the cern neutrino platform, Journal of Instrumentation **15**, P12004 (2020).

[64] T. Igarashi *et al.*, Performance of VUV-sensitive MPPC for Liquid Argon Scintillation Light, Nucl. Instrum. Meth. A **833**, 239–244 (2016).

[65] T. Pershing *et al.*, Performance of Hamamatsu VUV4 SiPMs for detecting liquid argon scintillation, JINST **17**, P04017 (2022).

[66] V. M. Gehman *et al.*, Fluorescence Efficiency and Visible Re-emission Spectrum of Tetraphenyl Butadiene Films at Extreme Ultraviolet Wavelengths, Nucl. Instrum. Meth. A **654**, 116–121 (2011).

[67] C. M. B. Monteiro *et al.*, Secondary scintillation yield in pure argon, Phys. Lett. B **668**, 167–170 (2008).

[68] T. Alexander *et al.* (DarkSide Collaboration), Light Yield in DarkSide-10: A Prototype Two-Phase Argon TPC for Dark Matter Searches, Astropart. Phys. **49**, 44–51 (2013).

[69] P. Agnes *et al.* (DarkSide Collaboration), First Results from the DarkSide-50 Dark Matter Experiment at Laboratori Nazionali del Gran Sasso, Phys. Lett. B **743**, 456–466 (2015).

[70] P. A. Amaudruz *et al.* (DEAP-3600 Collaboration), First results from the DEAP-3600 dark matter search with argon at SNOLAB, Phys. Rev. Lett. **121**, 071801 (2018).

[71] H. Cao *et al.* (SCENE Collaboration Collaboration), Measurement of scintillation and ionization yield and scintillation pulse shape from nuclear recoils in liquid argon, Phys. Rev. D **91**, 092007 (2015).

[72] B. Valeur and M. N. Berberan-Santos, in *Molecular Fluorescence* (John Wiley & Sons, Ltd., Noboken, NJ, USA, 2012) Chap. 3, pp. 53–74.

[73] M. Kuźniak and A. M. Szelc, Wavelength Shifters for Applications in Liquid Argon Detectors, Instruments **5**, 4 (2020).

[74] C. Benson *et al.*, Measurements of the intrinsic quantum efficiency and absorption length of tetraphenyl butadiene thin films in the vacuum ultraviolet regime, Eur. Phys. J. C **78**, 329 (2018).

[75] J. R. Graybill *et al.*, Extreme ultraviolet photon conversion efficiency of tetraphenyl butadiene, Appl. Opt. **59**, 1217–1224 (2020).

[76] V. Kumar and A. K. Datta, Vacuum ultraviolet scintillators: sodium salicylate and p-terphenyl, Appl. Opt. **18**, 1414–1417 (1979).

[77] V. M. Gehman, WLS R&D for the detection of noble gas scintillation at LBL: seeing the light from neutrinos, to dark matter, to double beta decay, JINST **8**, C09007 (2013).

[78] J. B. Birks *et al.*, 'Excimer' Fluorescence. IX. Lifetime Studies of Pyrene Crystals, Proceedings of the Royal Society of London Series A **291**, 556–569 (1966).

[79] M. Kuźniak *et al.*, Polyethylene naphthalate film as a wavelength shifter in liquid argon detectors, Eur. Phys. J. C **79**, 291 (2019).

[80] R. Jerry *et al.*, A study of the fluorescence response of tetraphenyl-butadiene, (2010), arXiv:1001.4214 [physics.ins-det] .

[81] R. Francini *et al.*, Tetraphenyl-butadiene films: VUV-Vis optical characterization from room to liquid argon temperature, JINST **8**, C09010 (2013).

[82] Murata Software Co. Ltd., Cae software femtet, `https://www.muratasoftware.com`.

[83] Hamamatsu Photonics K.K., S13361-6050 data sheets, (2023), accessed on 2023/CurrentDate.

[84] T. Doke and K. Masuda, Present status of liquid rare gas scintillation detectors and their new application to gamma-ray calorimeters, Nucl. Instrum. Meth. A **420**, 62–80 (1999).

[85] K. Ieki *et al.*, Large-Area MPPC with Enhanced VUV Sensitivity for Liquid Xenon Scintillation Detector, Nucl. Instrum. Meth. A **925**, 148–155 (2019).

[86] R. Acciarri *et al.*, Neutron to Gamma Pulse Shape Discrimination in Liquid Argon Detectors with High Quantum Effciency Photomultiplier Tubes, Phys. Procedia **37**, 1113–1121 (2012).

[87] A. Bondar, A. Buzulutskov, A. Dolgov, E. Frolov, V. Nosov, V. Oleynikov, E. Shemyakina, and A. Sokolov, Neutral bremsstrahlung in two-phase argon electroluminescence: further studies and possible applications, Nuclear Instruments and Methods in Physics Research Section A: Accelerators, Spectrometers, Detectors and Associated Equipment **958**, 162432 (2020), proceedings of the Vienna Conference on Instrumentation 2019.

[88] C. E. Aalseth *et al.* (DarkSide Collaboration), SiPM-matrix readout of two-phase argon detectors using electroluminescence in the visible and near infrared range, Eur. Phys. J. C **81**, 153 (2021).

[89] C. Oliveira *et al.*, A simulation toolkit for electroluminescence assessment in rare event experiments, Physics Letters B **703**, 217–222 (2011).

[90] M. Kimura *et al.*, Liquid argon scintillation response to electronic recoils between 2.8–1275 kev in a high light yield single-phase detector, Phys. Rev. D **102**, 092008 (2020).

[91] E. Aprile *et al.*, Noble gas detectors, (2006).

[92] https://www.shimadzu.co.jp/products/opt/products/mono01-12-02.html, .

[93] H. Fuke *et al.*, The pGAPS experiment: an engineering balloon flight of prototype GAPS, Adv. Space Res. **53**, 1432–1437 (2014).

[94] A. Takada *et al.*, Observation of Diffuse Cosmic and Atmospheric Gamma Rays at Balloon Altitudes with an Electron-tracking Compton Camera, Astrophys. J. **733**, 13 (2011).

[95] K. Abe *et al.*, Measurement of the cosmic-ray antiproton spectrum at solar minimum with a long-duration balloon flight over Antarctica, Phys. Rev. Lett. **108**, 051102 (2012).

[96] A. Curioni, Ph.d. dissertation thesis, Ph.D. thesis, Columbia University (2004).

[97] N. Aeronautics and S. A. (NASA), U.s. standard atmosphere, 1976, Tech. Rep. (1976) nASA-TM-X-74335.

[98] H. Fuke *et al.*, A new balloon base in japan, Advances in Space Research **45**, 490–497 (2010).

[99] P. Agnes *et al.* (DarkSide Collaboration Collaboration), Darkside-50 532-day dark matter search with low-radioactivity argon, Phys. Rev. D **98**, 102006 (2018).

[100] C. E. Aalseth *et al.* (DarkSide-20k Collaboration), DarkSide-20k: A 20 tonne two-phase LAr TPC for direct dark matter detection at LNGS, Eur. Phys. J. Plus **133**, 131 (2018).

[101] P. Agnes *et al.* (DarkSide-20k Collaboration), Separating ^{39}Ar from ^{40}Ar by cryogenic distillation with Aria for dark-matter searches, Eur. Phys. J. C **81**, 359 (2021).

[102] H. Yoneda *et al.*, Reconstruction of multiple compton scattering events in mev gamma-ray compton telescopes towards grams: The physics-based probabilistic model, Astroparticle Physics **144**, 102765 (2023).

List of publications

Publications

1. Kazutaka Aoyama, Masashi Tanaka, Masato Kimura, Kohei Yorita, Development of a liquid argon detector with high light collection efficiency using tetraphenyl butadiene and a silicon photomultiplier array, Progress of Theoretical and Experimental Physics, Volume 2022, Issue 4, 043H01
2. Kazutaka Aoyama, Masato Kimura, Hiroyuki Morohoshi, Tomomasa Takeda, Masashi Tanaka, Kohei Yorita, Measurement of emission spectrum for gaseous argon electroluminescence in visible light region from 300 to 600 nm, Nucl.Instrum.Meth.Phys.Res.A Volume 1025 (2022) 166107
3. M.Kimura, K.Aoyama, M.Tanaka, K.Yorita, Liquid argon scintillation response to electronic recoils between 2.8–1275 keV in a high light yield single-phase detector, Phys. Rev. D 102, 092008

Conference Proceedings

1. Kazutaka Aoyama, Increasing light collection efficiency of liquid argon detector for low mass WIMP search, 2020 Journal of Physics: Conference Series 1468, 16th International Conference on Topics in Astroparticle and Underground Physics (TAUP2019), 012034 (2020)

Talks at Conference

1. Kazutaka Aoyama, Status and prospect of the Gamma-Ray and Anti-Matter Survey (GRAMS), Kashiwa Dark Matter Symposium 2023, December 5-8 2023, Kashiwa, Japan
2. Kazutaka Aoyama, Increasing light collection efficiency of liquid argon detector for low mass WIMP search, 16th International Conference on Topics in Astroparticle and Underground Physics (TAUP 2019), September 9-13 2019, Toyama, Japan